Modelling and Simulation of Twin-Bed Pressure Swing Adsorption Plants for the Generation of High-Purity Nitrogen

Von der Fakultät für Ingenieurwissenschaften,
Abteilung Maschinenbau und Verfahrenstechnik der

Universität Duisburg-Essen

zur Erlangung des akademischen Grades

einer

Doktorin der Ingenieurwissenschaften

Dr.-Ing.

genehmigte Dissertation

von

Aleksandra Marcinek
aus
Racibórz

Gutachter:

Univ.-Prof. Dr.-Ing. Dieter Bathen

Univ.-Prof. Dr.-Ing. Tobias Fieback

Dr.-Ing. Joachim Guderian

Tag der mündlichen Prüfung: 27.10.2021

I Acknowledgments

The presented scientific research was attainable due to the cooperation of Münster University of Applied Sciences, University of Duisburg-Essen, and the company CarboTech AC GmbH, Essen. Therefore, I would like to express my gratitude to everyone from those institutions, who was involved in the preparation, organisation, and execution of the joint project.

Especially, I thank Prof. Dr.-Ing. Joachim Guderian from the Department of Chemical Engineering at Münster University of Applied Sciences for creating an opportunity for me to work on this exciting project, for his trust, regular expert advice, as well as encouragement to take up new professional challenges. Moreover, I thank Prof. Dr.-Ing. Dieter Bathen from the Department of Mechanical and Process Engineering at University of Duisburg-Essen for substantive supervision over the progress of my work and many productive discussions.

I would like to acknowledge the researchers, who contributed to the success of my work. I thank Dr. Andreas Möller from 3P Instruments, Leipzig, as well as Dr. Frieder Dreisbach and Dr. Thomas Paschke from TA Instruments, Bochum, for performing an experimental investigation of adsorption isotherms. I also wish to show my appreciation to all student-colleagues, who assisted me during the project.

Finally, I thank most of all my dear husband, El Mahdi Chaker, who I can always count on; for his incessant support, comprehension, and spiritual relief not only during the doctoral studies but also on an every-day basis.

Steinfurt, October 2021 Aleksandra Marcinek

II Table of Contents

III List of Figures

IV List of Tables

V List of Symbols and Abbreviations

A	sorption frequency factor [m^2/s]
a	specific area of adsorbent [m^2/kg]
a_p	specific particle surface area per unit volume of bed [m^2(pellet area)/m^3(bed)]
c_{ads}	molar concentration in adsorbed phase [$kmol/m^3$]
c_i	gas concentration in stream i [$kmol/m^3_n$]
c_k	molar concentration of component k [$kmol/m^3$]
C_{pak}	specific adsorbed phase heat capacity at constant pressure of component k [MJ/kmol/K]
C_{pg}	specific gas phase heat capacity at constant pressure [MJ/kmol/K]
C_{pR}	heat capacity of the product receiver shell [J/kg/K]
C_{ps}	specific solid phase heat capacity at constant pressure [MJ/kg/K]
Cv	valve flow coefficient [kmol/s/bar]
C_{vg}	specific gas phase heat capacity at constant volume [MJ/kmol/K]
d	pore diameter [nm]
D	Fickian diffusion coefficient [m^2/s]
D_0	corrected diffusivity, surface diffusion coefficient at zero loading [m^2/s]
D_B	packed-bed diameter [m]
D_e	effective diffusion coefficient [m^2/s]
D_{mk}	mean molecular diffusion coefficient of component k [m^2/s]
D_R	product receiver diameter [L]
D_s	surface diffusion coefficient [m^2/s]
E_a	sorption activation energy [kJ/kmol]
E_{zk}	axial dispersion coefficient of component k [m^2/s]
F	gas flow rate [kmol/s]
h	gas-solid heat transfer coefficient [$MW/m^2/K$]
H_B	packed-bed length [m]
h_R	gas-product receiver shell heat transfer coefficient [$MW/m^2/K$]
h_{Ra}	ambient-product receiver shell heat transfer coefficient [$MW/m^2/K$]
h_w	gas-wall heat transfer coefficient [$MW/m^2/K$]
k_{gz}	effective axial gas phase thermal conductivity [MW/m/K]
k_{sz}	effective axial solid phase thermal conductivity [MW/m/K]
M	molecular weight [kg/kmol]
m_R	mass of product receiver shell [kg]
P	pressure [bar abs]
p_k	partial pressure of component k [bar abs]
Q_i	gas flow rate in stream i [m^3_n /h]
R, R_g	molar gas constant [J/mol/K, kJ/ kmol/K]
r_0, r_p	adsorbent pellet radius [m]
T_0	reference temperature [K]
T_a	ambient temperature [K]
T_g	gas phase temperature [K]
T_s	solid phase temperature [K]

v_{ads}	adsorbate phase molar volume [m^3/mol]
V_B	bottom-void volume [cm^3]
V_{CMS}	total packed-bed density in PSA system [m^3]
v_g	gas phase superficial velocity [m/s]
v_{gas}	gas molar volume [m^3/mol]
V_R	product receiver volume [L]
V_T	top-void volume [cm^3]
w_k	loading of component k [kmol/kg]
w_k^*	equilibrium loading of component k [kmol/kg]
w_{s0k}, b_{0k}, n_{0k}, α_k, χ_k, Q_k	Sips isotherm parameters of component k
w_{sk}^*	saturation equilibrium loading of component k [kmol/kg]
w_{total}	total adsorbent loading [kmol/kg]
X	purge proportionality factor [-]
$\bar{X}$	mean value
x_i	gas mass fraction in stream i [kg/kg]
y_i	gas molar fraction in stream i [kmol/kmol]
y_k	mole fraction of component k in the gas phase [kmol/kmol]
z_k	mole fraction of component k in the adsorbed phase [kmol/kmol]

δ_{exp}	relative error between PIs determined experimentally [%]
δ_{sim}	relative error between PIs computed in Monte-Carlo method [%]
Δg	change in Gibbs free energy [J/mol]
Δh_{ads}, ΔH_k	heat of adsorption of component k [J/mol, kJ/mol]
Δh_v	heat of evaporation [J/mol]
Δp, ΔP	change in pressure, pressure difference [Pa, bar]
ΔT	change in temperature [K]
Δs	change in entropy [J/mol/K]
Δv	change in molar volume [m^3/mol]
ε_B	total bed voidage [m^3(void+pore)/m^3(bed)]
ε_i	interparticle voidage [m^3(void)/m^3(bed)]
ε_P	intraparticle voidage [m^3(pore)/m^3(pellet)]
$\theta = w_k^*/w_{sk}^*$	adsorbent surface coverage [-]
μ, μ_0	chemical potential, reference chemical potential [J/mol]
π	spreading pressure [N/m]
ρ_g	gas phase molar density [kmol/m^3]
ρ_i	gas density in stream i [kg/ m^3_n]
ρ_s	solid phase bulk density [kg/m^3]
σ	absolute uncertainty value
$\sigma_{\bar{X}}$	percentage uncertainty of the mean value
Φ	relative error between experimental and simulated PIs [%]
ψ	adsorbent pellet shape factor [-]
Ω	parameter dependent on half-cycle time [-]
$\partial w/\partial t$	mass transfer rate [kmol/kg/s]

ASU	air separation unit
CMS, MSC	carbon molecular sieve, molecular sieve carbon
CSS	cyclic-steady-state
CVD	chemical vapour deposition

EXP	experimental value
GMB	general mass balance
HTC	effective heat transfer coefficient
IAST	ideal adsorption solution theory
LDF	linear driving force
MTC	effective mass transfer coefficient
MTZ	mass transfer zone
OMB	oxygen mass balance
PFD	process flow diagram
PI	performance indicator (here: either productivity or air demand)
PSA	pressure swing adsorption
QDF	quadratic driving force
QDS	quadratic differencing scheme
SIM	simulated value
V	valve model
VPSA	vacuum pressure swing adsorption

VI Abstract

At present, nitrogen production from air by pressure swing adsorption (PSA) is simulated almost exclusively at low product purity levels (< 99 % N_2). However, with increasing global demand for highly purified gases provided by energy-efficient separation processes, the requirement for either extensive experimental research in the high-purity range or predictive computer simulations arises. Moreover, with increasing nitrogen purity, PSA plants require an over-proportional air demand with the consequence that high-purity PSA systems engender a distinct interest in energy-saving measures. This dissertation presents a mathematical model of a twin-bed PSA plant equipped with a carbon molecular sieve (Shirasagi MSC CT-350) adsorbent for the generation of high-purity nitrogen (99.9 – 99.999 % N_2). The corresponding model is implemented in the process simulator Aspen Adsorption™. The influence of operating conditions, cycle organisation, as well as plant design on the PSA process performance is validated. Specifically, effects of adsorption pressure, operating temperature, half-cycle time, purge stream flow rate, cutting time, flow resistances, and volume of N_2-receiver tank are studied. The precision of the performance prediction by numerical simulations is critically discussed. Based on the new insights, efficiency improvement strategies with a focus on reduced energy consumption are introduced and reviewed. Finally, a future outlook on the research is presented.

The content of this dissertation is partially published in the following articles:

- A. Marcinek, J. Guderian, D. Bathen, *Performance determination of high-purity N_2-PSA plants*, Adsorption 26 (2020) 1215-1226, DOI: 10.1007/s10450-020-00204-9 [1].
- A. Marcinek, J. Guderian, D. Bathen, *Process intensification of the high-purity nitrogen production in twin-bed Pressure Swing Adsorption plants*, Adsorption (2021), DOI: 10.1007/s10450-020-00291-8 [2].
- A. Marcinek, A. Möller, J. Guderian, D. Bathen, *Dynamic simulation of high-purity twin-bed N_2-PSA plants*, Adsorption (2021), DOI: 10.1007/s10450-021-00320-0 [3].

1 Introduction

Nitrogen gas is a colourless, odourless, inert, and non-flammable substance, which remains indispensable in many industrial businesses and covers vastly different application areas i.e. (1) iron and steel industry; (2) electronics industry; (3) pharmaceuticals industry; (4) agriculture industry; (5) metallurgical and chemical processes; (6) mining sector; (7) food packaging sector; (8) automotive sector; (9) fire prevention systems; or (10) refrigeration systems. Gaseous nitrogen is utilised mostly due to its inert properties – to provide modified atmospheres by replacing the ambient air where the presence of oxygen would involve fire, explosion, or unfavourable oxidation. Therefore, oxygen is considered as the primary pollutant of nitrogen. Depending on the specific application, the acceptable contamination threshold of oxygen varies significantly. For instance, the requirement of the nitrogen purity level for fire-prevention systems is about 13 vol.-% O_2 [4], for electronics assembly 0.1 vol.-% O_2 [5], and for stainless-steel manufacturing 10 ppm O_2 [6]. Thus, taking into consideration the requested gas purity with respect to the needed production rate, the most economical method of nitrogen generation is suggested.

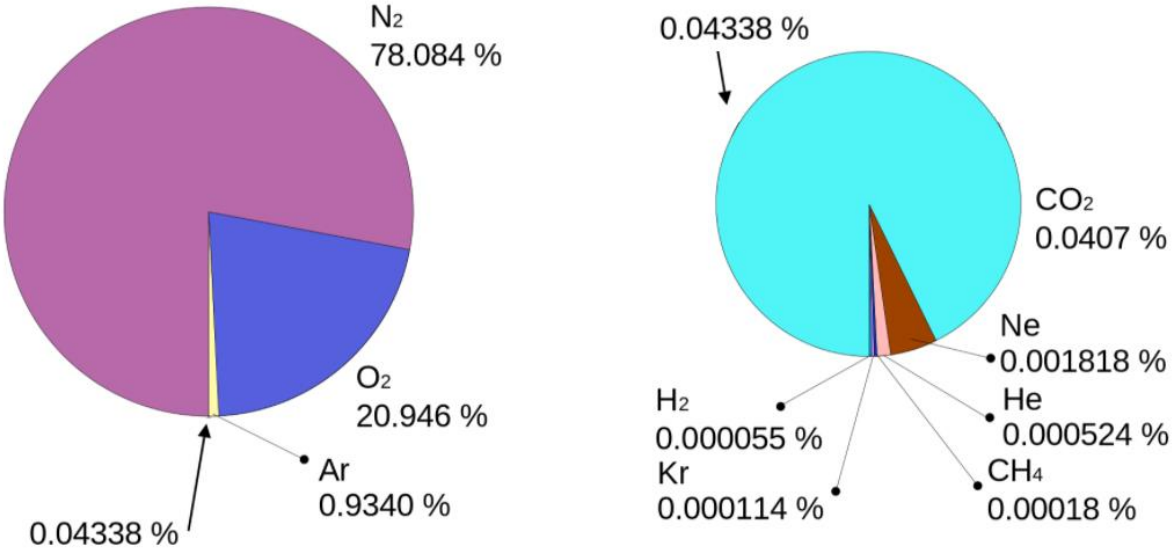

Fig. 1-1 Composition of air by vol.-%, excluding water vapour [7]

Air is the main source of nitrogen. Since the composition of air at low altitudes is remarkably constant, except for variation in local concentrations of water vapour and carbon dioxide, the air consists of 78.084 vol.-% of nitrogen. The complete composition of air is given in Fig. 1-1 [7]. As the mass of the earth's atmosphere is approximately 5 × 109 million tonnes, the supply is unlimited and the annual industrial production, though vast, is insignificant by comparison [8]. About two-thirds of the N_2 produced industrially is supplied as a gas, mainly in pipes, but also in cylinders under pressure; whereas the remaining one-third is supplied as a liquid – mostly as refrigerant [8].

As presented in Fig. 1-2, the size of the nitrogen market is constantly expanding, which directly indicates the increasing global demand. In addition to this, the cost of N_2 is particularly dependent on electricity costs, though plant maintenance and transport costs also obtrude [8]. For those reasons, nitrogen generation technologies have been persistently improved in terms of both capital and operating costs.

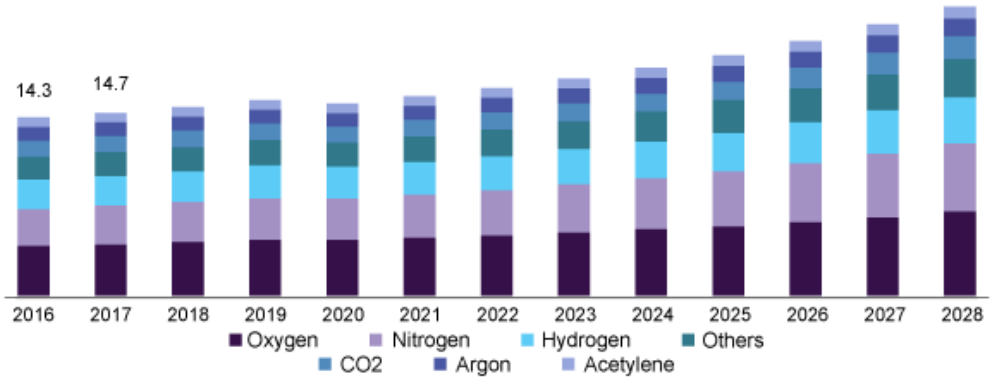

Fig. 1-2 Overview of U.S. industrial gases market size in million USD; detailed data unavailable [9]

At present, the production of nitrogen from the air is carried out mainly by three methods: cryogenic distillation, pressure swing adsorption (PSA), and membrane separation [10]. The selection of a suitable technique is primarily based on the required production rate, load profiles, utilisation (e.g. operating hours per week), and purity level of the product gas. As presented in Fig. 1-3, the operation of cryogenic air separation units (ASUs) is the most efficient method if large amounts of high-purity nitrogen are demanded; whereas the utilisation of membranes would be preferred when the requirement for either quantity and purity is lower. The PSA technology for nitrogen generation is commercially established in the intermediate area, for product flow rates up to several thousand m^3_n/h (at 0 °C, 1 bar abs) and product purity levels up to 10 ppm of the residual oxygen concentration. In order to provide an engineering tool for selecting the most economic technology of nitrogen production, a decision tree was proposed by Emrani et al. [11], which is shown in Fig. 1-4. Therefore, the most suitable technique can be selected based on heuristic rules along with literature data implemented within the selection diagram according to Fig. 1-3.

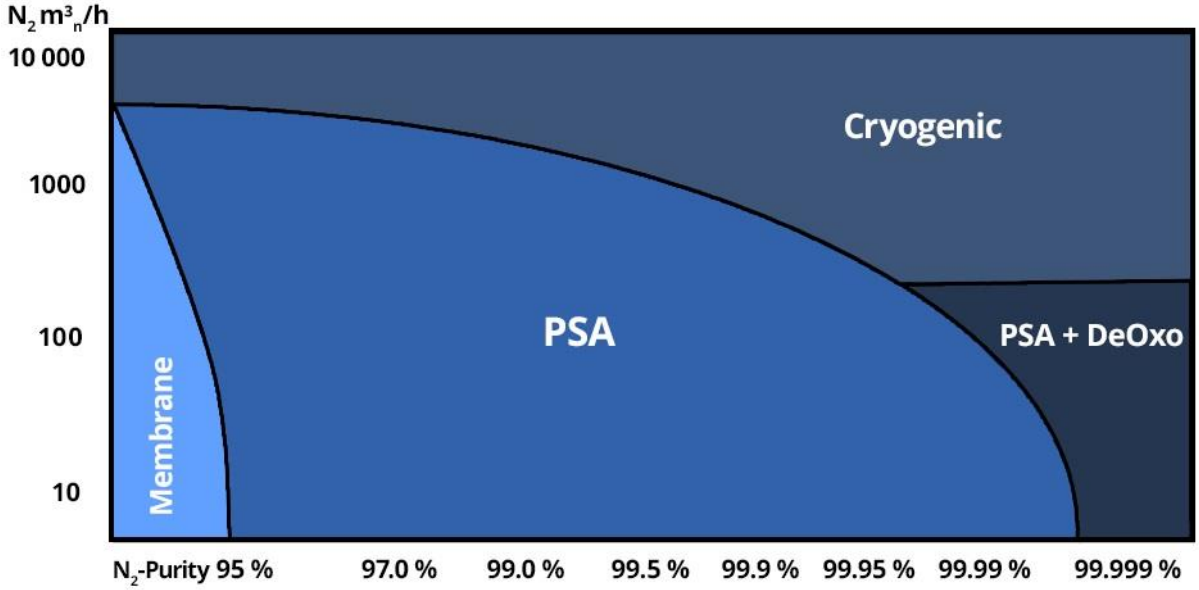

Fig. 1-3 Selection diagram for the N_2-production technique

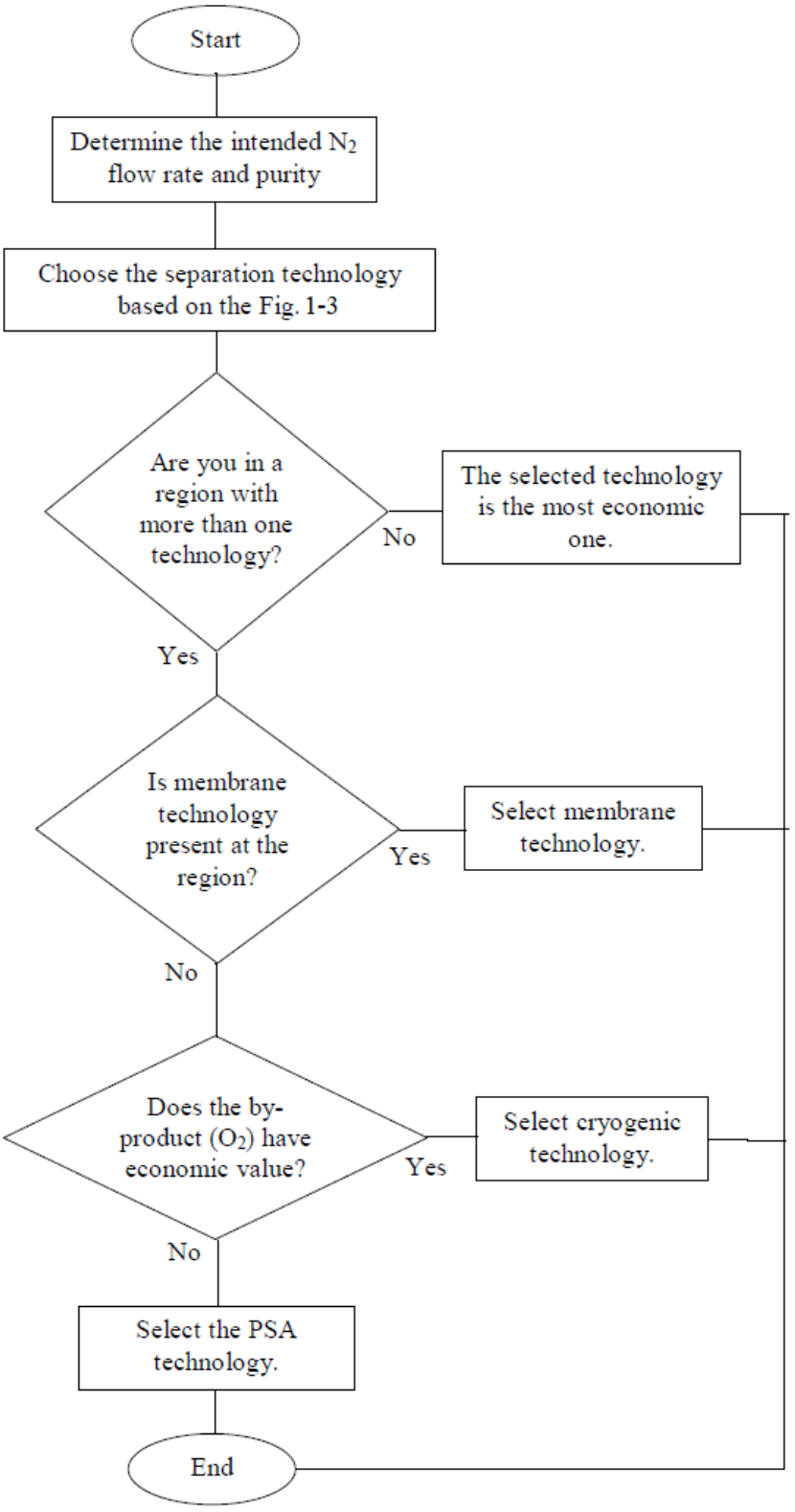

Fig. 1-4 Decision tree for the selection of N_2-production technique

However, diversified hybrid-systems for nitrogen generation, e.g. hollow-fiber membranes with porous catalytic layer [12]; membrane/PSA modules [13]; or PSA/de-oxo units involving a catalytic reaction with hydrogen [14] have also been developed.

1.1 Nitrogen production via PSA technology

The technology of pressure swing adsorption (PSA) for the production of gaseous nitrogen is based on physical adsorption; hence, the ability of carbon molecular sieves (CMS) adsorbents to capture oxygen molecules from a compressed air stream. The separation of oxygen from nitrogen is possible by the fact that the sorption rate of oxygen is remarkably faster than that of nitrogen. What is important is that the PSA technique enables nitrogen generation at ambient temperature, without involving any heat exchange units.

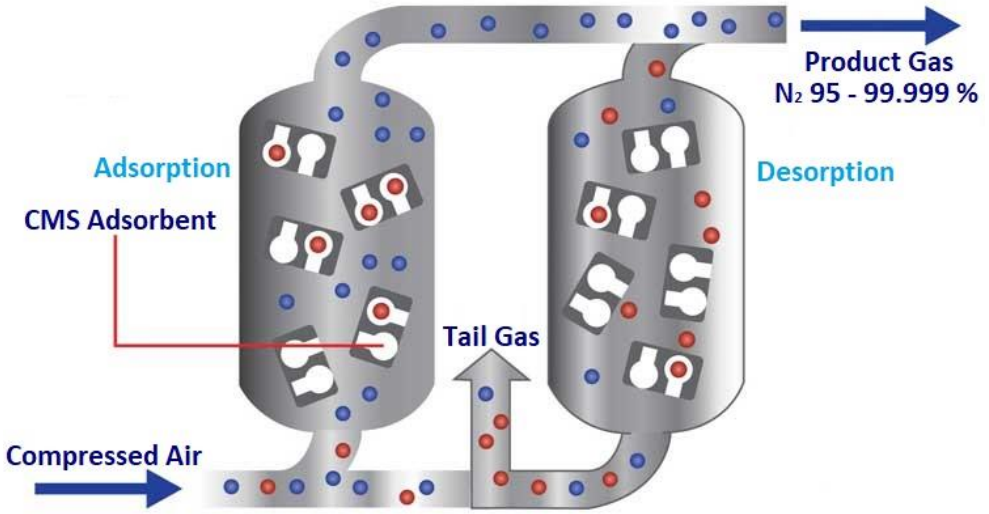

Fig. 1.1-1 Twin-bed PSA operation principle [15]

Whether considering twin-bed PSA, as presented in Fig. 1.1-1, one bed (here shown on the left) is pressurised by compressed air up to operating pressure level. Therefore, the adsorption of oxygen molecules (marked in red) occurs and purified nitrogen gas (marked in blue) is collected at the top of the adsorber as a product stream. At the same time, the other bed (here shown on the right) is depressurised to atmospheric pressure level. Thus, the desorption of previously captured oxygen molecules takes place, during which the adsorbent is regenerated. The process alternates between two columns what allows continuous nitrogen production.

As presented in Fig. 1.1-2, air separation with CMS does not occur by means of an equilibrium-based process, since there is no significant difference in oxygen and nitrogen adsorption isotherm courses; thus, no usable selectivity occurs. However, as shown in Fig. 1.1-3, oxygen is adsorbed much faster on CMS in comparison to nitrogen. For this reason, nitrogen production can be performed by a kinetic-based process. High selectivity is attainable as a result of the sieving effect in intentionally narrowed micropore mouths. Thereby, the common PSA cycle time is relatively short, e.g. a 120 s cycle includes 60 s for the production step (adsorption process) and 60 s for the regeneration step (desorption process).

In principle, two main unit operations are involved in order to execute the air separation by means of PSA technology: (1) air compression and purification; and (2) pressure swing adsorption. The associated process block diagram is presented in Fig. 1.1-4. The list of input and output streams is shown in Tab. 1.1-1. Fig. 1.1-5 shows a picture of typical twin-bed N_2-PSA skid.

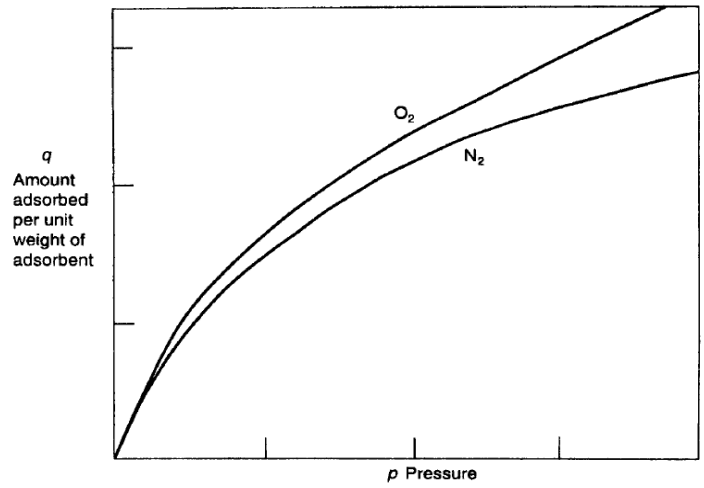

Fig. 1.1-2 Adsorption isotherms of oxygen and nitrogen on CMS adsorbent [16]

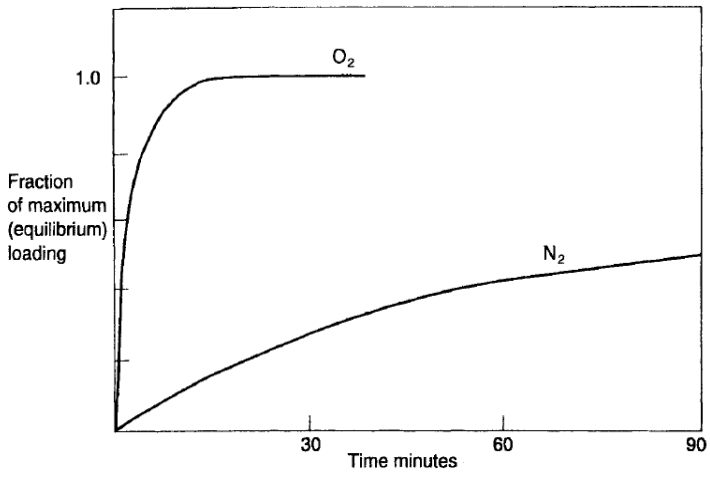

Fig. 1.1-3 Fractional uptake rates of oxygen and nitrogen on CMS adsorbent [16]

Regarding the N_2-PSA technology, it is commonly accepted that the product purity comprises the content of both nitrogen and argon, since many industrial applications do not require an additional separation of inert gas mixtures. Consequently, the determination of the product purity is accomplished by assuming a binary gas mixture, where the difference to the oxygen concentration simply results in the nitrogen purity.

Therefore, it is frequently assumed that the feed mixture consists of oxygen and nitrogen gases at approximate concentrations of 20.9 vol.-% O_2 and 79.1 vol.-% N_2. The introduced simplification originates in the irrelevance of other air components for studying the system due to their significantly lower concentrations in relation to oxygen and nitrogen. However, despite the presented assumption, it is important to declare that the product stream of N_2-PSA technology is predominantly a mixture of nitrogen and argon; and the tail-gas stream is predominantly a mixture of nitrogen, oxygen, argon, and carbon dioxide.

The air compression is the key aspect of operating costs, while the bed size is the dominating factor in capital costs [17]. Similar to membrane plants, N_2-PSA systems require an over-proportional air demand with increasing nitrogen purity. Hence, the operation of high-purity PSA plants motivates a particular interest in process optimisation with a focus on the reduction of air demand, without increasing the number or volume of adsorber columns.

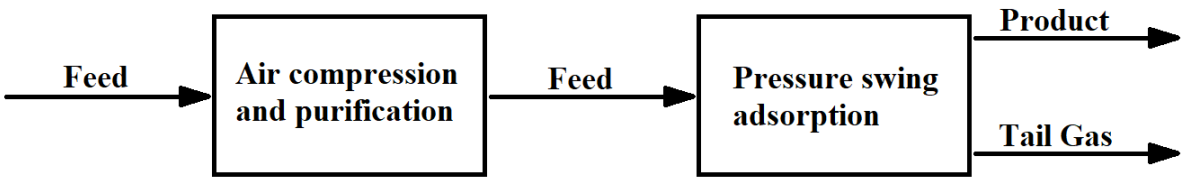

Fig. 1.1-4 Process block diagram of PSA technology

Moreover, multiple process variables and cycle organisation strategies give an opportunity for customising the system to specific requirements, which allow for the prospect of minimised operating costs. Thus, very different measures can be considered for intensifying PSA processes, including the application of improved separation materials as well as the configuration of the installation. Related thoughts are e.g. multi-bed PSA systems [18], trim feed concepts [19], dual-reflux concepts [20], hybrid systems [21], or opting for vacuum-PSA (VPSA) instead of PSA systems. Additionally, if the product gas is required on the low-pressure level, the recovery of pressure energy from the product stream by microturbines coupled with electric power generators is also a potential development. Furthermore, the particle diameter can play a significant role as a measure for intensifying processes – depending on the mass transfer controlling steps from bulk to particle internal adsorption sites for the considered adsorbent [22]. Unfortunately, many of the listed concepts are not feasible in high-purity N_2-PSA plants since the commercially established nitrogen productivity range of maximum a few thousand m^3_n/h makes those approaches unaffordable at present.

Fig. 1.1-5 Industrial-scale twin-bed N_2-PSA skid [23]

Thus, taking into consideration all the reasons presented here, the introduction of a mathematical model that quantitively predicts the performance of PSA-plants at different operating conditions would eliminate the necessity of performing extensive experimental research, and allow investigating new methods of process intensification with a particular focus on implementation of energy-saving strategies.

Tab. 1.1-1 Input and output streams associated with the process block diagram of N_2-PSA technology

Unit operation	**Input stream**	**Output stream**	
Air compression and purification	Air from ambient	Dry compressed air without solid particles and organic vapours	
Pressure swing adsorption	Dry compressed air without solid particles and organic vapours	Purified nitrogen at specific purity level	Oxygen-enriched tail gas

1.2 State of knowledge

Pressure swing adsorption is a well-established technique applied for the separation of multicomponent gas mixtures. Currently, this method is implemented in CO_2-capture technologies frequently [24–26], but also in traditional industrial processes, such as hydrogen purification, biogas upgrading, noble gas recovery, or, as considered here, air separation [27–29]. Hence, different process intensification methods dedicated to PSA techniques are developed within many application fields. However, in order to study the N_2-PSA system, it is essential that the literature review covers two general topics regarding (1) experimental and numerical investigation of PSA systems, and (2) thermodynamic equilibrium and diffusional mass transfer within microporous adsorbents. By means of this strategy only, it is possible to understand the process at both macroscopic and microscopic levels, which are ultimately interdependent.

The industrial implementation of PSA separation techniques began in the 1980s. The commonly-known patent assigned by Skarstrom in 1958, which introduces the moisture removal from atmospheric air by adsorption process [30], is frequently considered to be the original invention of PSA; however, earlier patents were issued already in the 1930s, e.g. by Finlayson and Sharp [31]. This extraordinarily long time between the invention of the technology and its commercialisation can be explained by the fact that the PSA process operates under transient conditions; unlike the conventional separation techniques, e.g. distillation, extraction, or absorption, which operate under steady-state conditions [32]. Since the transient processes are mathematically described by a set of partial differential equations, the relationship between plant performance and operational variables is less obvious when compared with traditional technologies, which are represented by a set of ordinary differential equations [32]. However, together with the benefit of computer science advancement, the understanding of PSA processes constantly improves; therefore, many publications are currently available.

Ruthven, Farooq, and Knaebel have provided a comprehensive summary of the underlying science and technology of pressure swing adsorption processes [32], presenting the fundamentals of mathematical modelling. Crittenden and Thomas have described in detail adsorber design procedures considering thermodynamic equilibrium relationships, kinetic relationships, heat effects, and flow dynamic constraints [16]. Furthermore, the principles of mass transfer associated with adsorption/desorption processes are given by Ruthven [33], Do [34], and Yang [35] which can be applied while studying PSA systems. More specifically, Kärger and Ruthven explain the diffusion phenomenon in microporous solids [36]. All publications mentioned here contain basic information corresponding to air separation processes.

The crucial aspect regarding modelling of kinetically-controlled air separation is the correct representation of the mass transfer kinetics in highly microporous CMS adsorbent. The commonly known linear driving force (LDF) model is frequently applied due to its simplicity and physical consistency [37]. Details of the LDF approach are presented in Chapter 2.2.1. Interestingly, the N_2-PSA process simulations involving LDF model present results almost exclusively at low product purity levels (< 99 vol.-% N_2) [38–43]. Shirley and Lemcoff were the sole authors of predicted and experimental data in the range of higher nitrogen purity (> 99.9 vol.-% N_2), describing the mass transfer kinetics through the Langmuir adsorption rate expression as an approximation of the slit-potential-rate model introduced by LaCava [44–46]. The model was deduced from knowledge of the structure of carbon molecular sieves and basic physical principles. Since the diffusing molecules experience a net repulsive interaction upon entering very narrow pores of molecular dimensions, they must pass an energy barrier to gain admittance to the adsorption volume. The difference of magnitude of these energy barriers for various adsorptives gives rise to different diffusion rates and therefore causes separation [47]. Thus, the adsorption process consists of two steps: (1) crossing the activation energy barrier at the entrance to the slit, and (2) adsorption on the cavity surface, which, according to the authors, is following the classical Langmuir adsorption rate [45]. Based on those considerations, the mass transfer rate is quantified as shown in Eq. 1.2-1.

$$\frac{\partial w_k(t)}{\partial t} = \frac{k_{slit} w_{sk}}{K_k\left(1-\theta_k\right)}\left[K_k c_k\left(1-\sum\theta_k\right)-\theta_k\right] \qquad \text{(Eq. 1.2-1)}$$

where: $w(t)$ is the adsorbed phase concentration, w_s is monolayer capacity, K is the Langmuir equilibrium constant, k_{slit} is the slit potential rate constant, c is gas phase concentration, and $\theta=w/w_s$ is the fractional surface coverage.

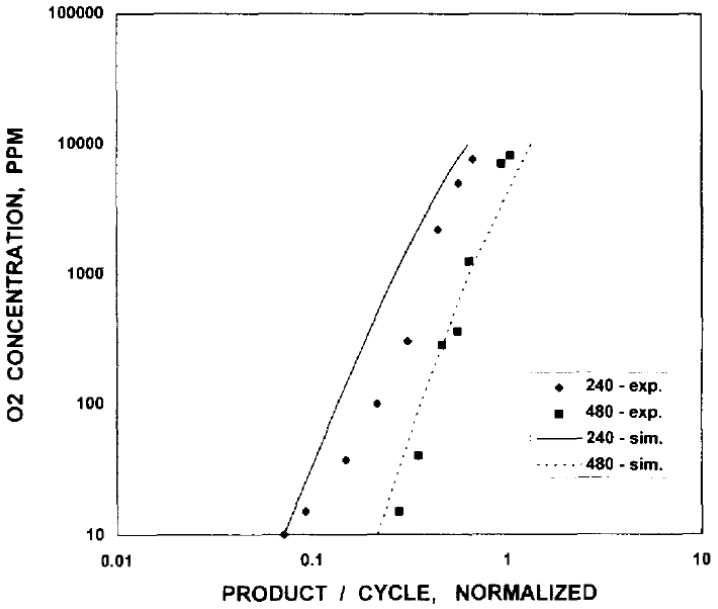

Fig. 1.2-1 Comparison between the predicted and experimental product rate for two cycle times [44]

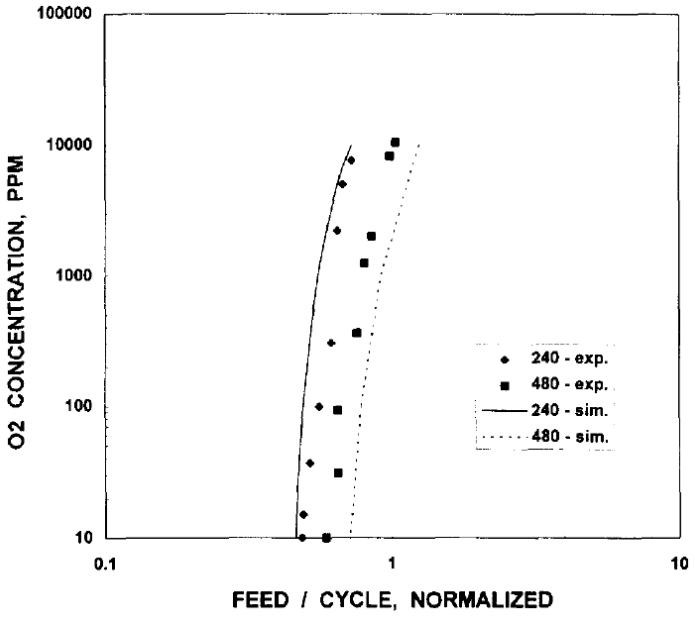

Fig. 1.2-2 Comparison between the predicted and experimental feed rate for two cycle times [44]

The authors investigated the influence of cycle time on the PSA process performance, which was confirmed by the model qualitatively; however, accuracy values were omitted. The comparison between predicted and experimental data is presented in Fig. 1.2.1–2. The applied model correctly predicts the product composition at very high (10 ppm O_2) and very low (1 vol.-% O_2) purity levels. In the intermediate range, the precision of prognostication significantly declines. For instance, it can be seen that at the experimental value of product purity equals about 300 ppm O_2, the mathematical model estimation equals about 2000 ppm O_2. Thus, the committed relative error of approximation equals about 85 %, which is not satisfying in industrial practice; especially in the case of operating a very basic PSA cycle.

Moreover, significant dissimilarities in the process dynamics were observed during generation of high-purity and low-purity nitrogen via PSA technique. Those findings suggest that either different mathematical models of mass transfer kinetics should be applied at specific product purity levels due to unique diffusion characteristics within microporous CMS; or, the universal mathematical model which properly predicts the PSA performance regardless of product purity level was not developed so far.

1.3 Motivation and purpose of scientific work

Despite many years of process employment (since the 1980s) along with experimental research and computer modelling, the N_2-PSA separation is still not fully comprehensible [35]. Various process intensification strategies were meanwhile developed and successfully implemented by engineers in commercial plants. However, both empirical data and process simulation results presenting those methods are still not acknowledged in literature. This provides the motivation to develop and to validate a new mathematical model of a twin-bed PSA for the production of high-purity nitrogen, covering multiple process conditions, operating strategies of technical relevance, and system design parameters. Therefore, both experimental and numerical data would bring significant benefits, such as improvement of engineering strategies, and progression of the scientific advancement.

However, any modifications of the PSA cycle organisation or slight alterations of process conditions influence the distribution of driving forces as a function of time within the production and regeneration steps. Those changes affect the local gas interstitial velocity, which again impacts, for instance, the local column pressure drop, the heat and mass transfer rate, and the axial dispersion of heat and mass [48,49]. Thus, the development of a predictive mathematical model becomes more challenging, especially in the case of kinetically-controlled nitrogen generation in the high-purity range.

In addition, a critical discussion of the simulation accuracy as well as the explicit experimental and simulation data with exact values of approximation errors are given in this work.

Finally, in light of the contemporary climate crisis, a particular focus on reduced energy consumption becomes a primary encouragement; since almost two-thirds of global electricity comes from the combustion of fossil fuels* [50], emitting large amounts of carbon dioxide to the atmosphere.

* applies to data from 2019

2 Theoretical background

Adsorption is the process of mass transfer from the fluid phase to the solid adsorbent, which is driven by the gradient of the chemical potential. The graphical representation of the system along with an indication of involved phases is presented in Fig. 2-1. Molecules being adsorbed lose their freedom of movement; therefore, the entropy and Gibbs free energy decrease in the system, which is consequently associated with a heat release. In accordance with Le Chatelier's principle, the adsorption process is intensified at low operating temperatures and high concentration or partial pressure of the adsorptive phase. In contrast, desorption is the reverse process to adsorption, during which the mass transfer occurs from the solid adsorbent to the bulk phase. It is an endothermic process, favoured at high operating temperatures and low adsorptive concentration.

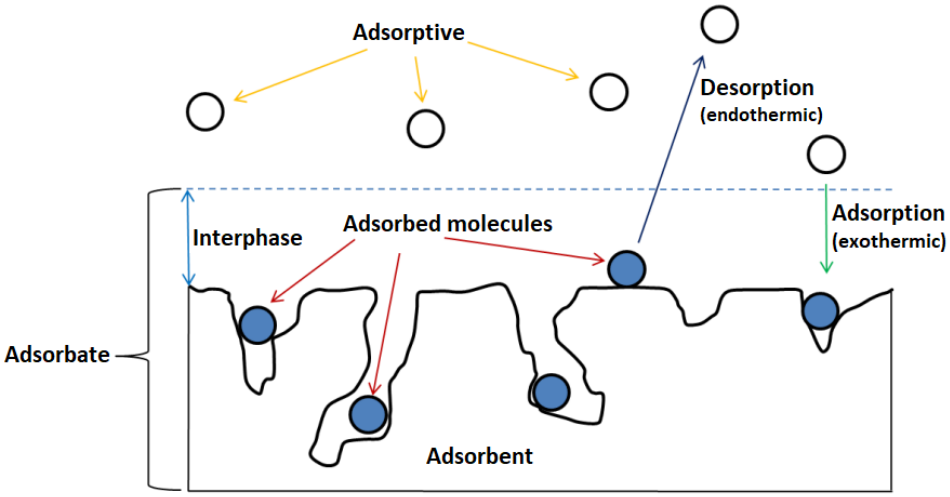

Fig. 2-1 Graphical representation of the system involving the adsorption/desorption process [51]

Depending on the nature of bonding forces between adsorbed molecules and active sites located on the surface of the adsorbent, the deposition of adsorptive occurs according to physisorption or chemisorption. Physisorption is associated with intermolecular forces (van der Waals forces) and does not involve a significant change in the electronic orbital patterns of the subjected molecules [52]. This process is reversible and its adsorption enthalpy is low (20-40 kJ/mol). Moreover, adsorbed molecules can form multilayers on the adsorbent surface. On the other hand, chemisorption is associated with valence forces of the same kind as those operating in the formation of chemical compounds [52]. It is an irreversible process of a high adsorption enthalpy (80-240 kJ/mol), during which a monolayer is formed on the adsorbent surface.

2.1 Adsorption equilibrium

Adsorption is induced by an imbalance imposed from the surroundings of the system [51]. Therefore, if the adsorbent is exposed to an adsorptive atmosphere, the system strives for thermodynamic equilibrium, which is energetically most favourable [53]. At the equilibrium state, the rate of adsorption and desorption is equal; namely, the net amount adsorbed does not change over time. However, once an imbalance is introduced to the system, the state variables adapt to achieve the energetic optimum yet again.

The adsorption equilibrium is commonly represented in the two-dimensional form, either (1) at constant temperature (adsorption isotherm), (2) at constant partial pressure (adsorption isobar), or (3) at constant amount adsorbed/adsorbent loading (adsorption isostere); as shown in Fig. 2.1-1. Considering the fundamental point of view on the adsorption phenomenon, it is feasible to derive models for a quantitative representation of thermodynamic equilibrium state. For instance, the classical Langmuir isotherm model results from the kinetic approach, and the Volmer model from the Gibbs thermodynamic equation [34]. In practice, however, models based on the fundamental theories do not always represent the data well, mostly due to inadequate assumptions. Therefore, empirical approaches are well-established in describing equilibrium data.

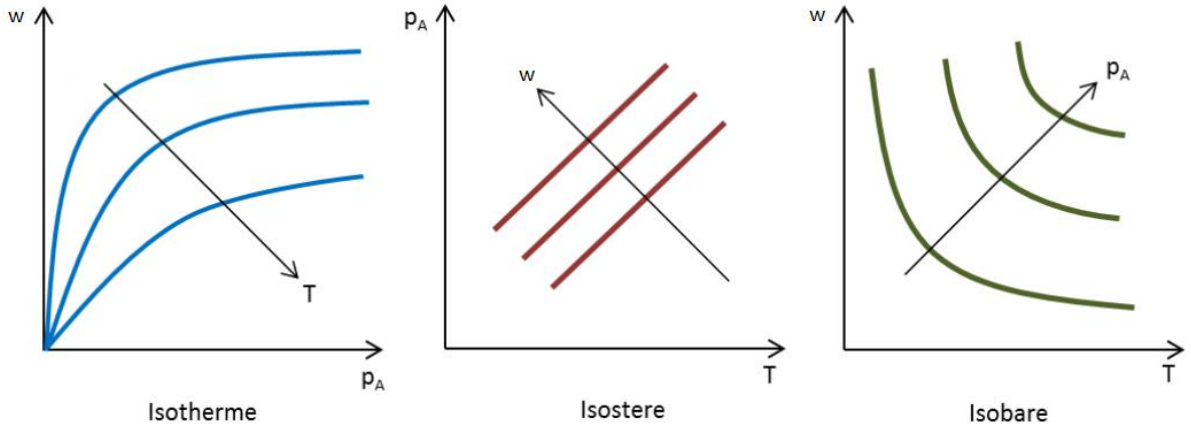

Fig. 2.1-1 Two-dimensional representation of adsorption equilibrium

In this work, the equation of Sips adsorption isotherm is applied to describe the behaviour of a single component at thermodynamic equilibrium, and the adsorption isostere is exploited to calculate the isosteric adsorption enthalpy. Moreover, the Ideal Adsorbed Solution Theory (IAST) was applied in order to evaluate the multi-component adsorption equilibria.

2.1.1 Sips isotherm

The Sips model for characterising the adsorption isotherm originates in the combination of Langmuir and Freundlich equations. It was introduced to describe adsorption of gases and vapors on heterogeneous surfaces below the capillary condensation region [34]; or in cases where Langmuir and Freundlich isotherms fail, e.g. the representation of water adsorption on zeolites which exhibits an S-shape isotherm [54], characterisation of adsorption in the liquid phase [55] including the pH-dependent adsorption [56], or biosorption of heavy metals ions [57]. The Sips single-component adsorption isotherm is calculated according to Eq. 2.1.1-1 [34].

$$w_k^* = w_{sk}^*(T)\frac{\left(b_k(T)\,p_k\right)^{1/n_k(T)}}{1+\left(b_k(T)\,p_k\right)^{1/n_k(T)}} \qquad \text{(Eq. 2.1.1-1)}$$

where: p_k is the partial pressure of component k, w_{sk}^* is the saturation equilibrium loading of component k, T is the temperature, b_k is the adsorption affinity of component k, and n_k is a dimensionless parameter that qualitatively characterises the heterogeneity of the adsorbate-adsorbent system. When n_k equals unity, the isotherm model reduces to the classical Langmuir

equation. However, the larger this parameter is, the higher the degree of system heterogeneity, as shown in Fig. 2.1.1-1.

The Sips equation circumvents the limitation of the rising adsorbate concentration associated with the Freundlich isotherm. At low adsorbate concentrations it reduces to the Freundlich isotherm; whereas at high concentrations it predicts a monolayer adsorption in a similar manner to the Langmuir isotherm. Namely, it predicts that the amount adsorbed reaches the saturation capacity, corresponding to complete coverage of all adsorption sites with adsorbate molecules. For this reason, the Sips isotherm should be used to describe only monolayer adsorption systems. However, as long as the equation is not used for equilibrium data extrapolation, it can be applied at higher pressures associated with multi-layer adsorption, but the parameter w_{sk}^* should not be considered as the ultimate saturation adsorption [58]. Moreover, since the Sips equation does not reduce to the linear isotherm at very low pressures, which is a constrain demanded by statistical thermodynamics, the application of the model in this range should be avoided.

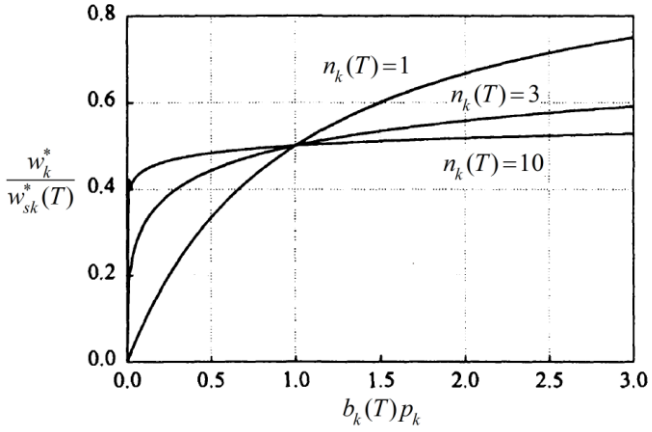

Fig. 2.1.1-1 Plots of the Sips equation as the function of $b_k(T)p_k$ [34]

2.1.2 Isostere method

The adsorption enthalpy is defined as the specific heat to be released/required when an adsorptive molecule binds/detaches to the solid surface of an adsorbent [59]. It remains a necessary parameter in the interpretation of adsorption and desorption processes, especially in the case of non-isothermal systems, since the temperature variation influences both adsorption equilibria and mass transfer kinetics. In gas-phase systems it can be determined experimentally via gas adsorption microcalorimetry technique [60]; or calculated straightforwardly based on analysis of adsorption isotherms via the so-called isostere method, which is simple and commonly practiced.

The isostere method originates in the following argumentation [51]. Since the adsorption isotherm identifies the thermodynamic equilibrium state between gas and solid phases, the Gibbs free energy equals zero at its every point, according to Eq. 2.1.2-1. Subsequently, the entropy term can be substituted by the quotient of adsorption enthalpy and temperature, as shown in Eq. 2.1.2-2. Therefore, by assuming that the volume of the adsorbate phase is negligible compared to the volume of the gas phase (Eq. 2.1.2-3) and substituting the volume of the gas phase according to the ideal gas law (Eq. 2.1.2-4), the adsorption enthalpy can be

determined directly from the slope of the straight line of an adsorption isostere, as presented in Eq. 2.1.2-5. The graphical illustration of the method is shown in Fig. 2.1.2-1.

$$d(\Delta g) = \Delta v \cdot \Delta p - \Delta s \cdot \Delta T = 0 \qquad \text{(Eq. 2.1.2-1)}$$

$$\frac{\Delta p}{\Delta T} = \frac{\Delta s}{\Delta v} = \frac{\Delta h_{ads}}{T \cdot \Delta v} \qquad \text{(Eq. 2.1.2-2)}$$

$$\Delta v = v_{gas} - v_{ads} \approx v_{gas} \qquad \text{(Eq. 2.1.2-3)}$$

$$v_{gas} = \frac{R \cdot T}{p} \qquad \text{(Eq. 2.1.2-4)}$$

$$\frac{dp}{p} = \frac{\Delta h_{ads} \cdot dT}{R \cdot T^2} \equiv \frac{d(\ln p)}{d(1/T)} = -\frac{\Delta h_{ads}}{R} \qquad \text{(Eq. 2.1.2-5)}$$

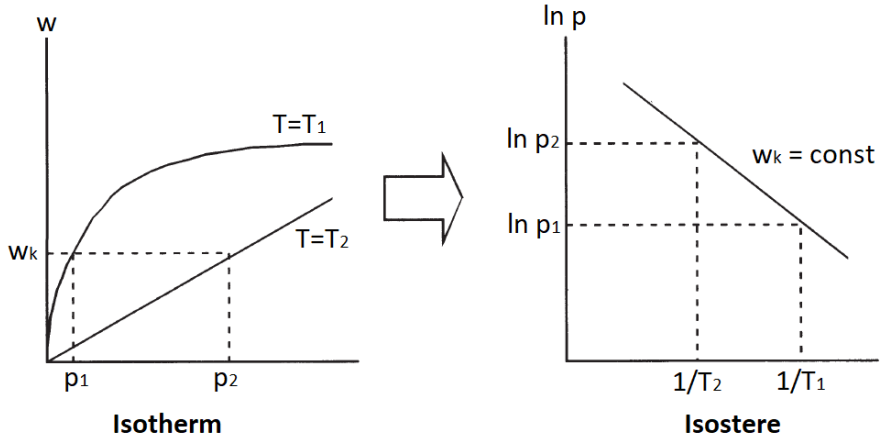

Fig. 2.1.2-1 Obtaining adsorption isostere from the adsorption isotherm [51]

The magnitude of adsorption enthalpy depends on the interactions between adsorbed molecules and active sites on the surface of the adsorbent. Therefore, due to the specific degree of system heterogeneity, the adsorption enthalpy decreases as the loading progresses. Moreover, above a certain number of multilayers created at the adsorbent surface, the adsorption turns into pure condensation, so that the amount of the adsorption enthalpy approaches the evaporation enthalpy [51]. The loading dependency of adsorption enthalpy in the gas phase is shown in Fig. 2.1.2-2.

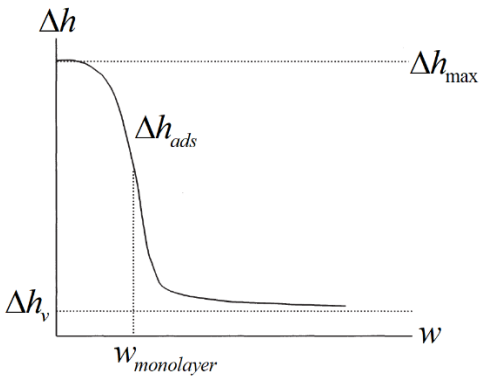

Fig. 2.1.2-2 Adsorption enthalpy as function of loading

2.1.3 Ideal Adsorbed Solution Theory

The information about the adsorption equilibrium of gas mixtures is of essential importance for the understanding and design of adsorption processes. Hence, the experimental determination of those data remains one of the most difficult empirical techniques in the adsorption field [61]. For this reason, different models have been proposed for predicting multicomponent adsorption data using only pure-component adsorption isotherms [62–64]; however, the IAST [65] is one of the most reliable and often-used. It originates in the thermodynamic approach, which is based on three fundamental assumptions: (1) adsorbate molecules in the mixture have equal access to the entire surface area of the adsorbent; (2) the adsorbent is homogeneous; and (3) the adsorbed phase is an ideal solution in which interactions between molecules are equivalent in strength and the spreading pressures of the components are equal at constant temperature [61]. Therefore, the IAST is an adsorption theory by analogy with Raoult's law for vapor-liquid equilibrium.

By means of this strategy, the presented system of equations can be established and treated numerically by applying iteration and integration techniques.

- The relation between spreading pressure π and adsorbent loading via Gibbs' isotherm [66], as shown in Eq. 2.1.3-1, where a is specific area of adsorbent and w_k^0/p_k^0 can be supplied by the adsorption isotherm equation. The spreading pressure is considered as the reduction of surface tension due to the spreading of the adsorbate over the adsorbent. Here, the superscript 0 indicates the pure component parameter.

$$\frac{\pi(p_k^0)\cdot a}{R_g\cdot T}=\int_0^{p_k^0}\frac{w_k^0}{p_k^0}dp_k^0 \qquad \text{(Eq. 2.1.3-1)}$$

- The equilibrium condition, as shown in Eq. 2.1.3-2, where N is number of components in the considered gas mixture.

$$\pi\equiv\pi_k=\pi_N \qquad \text{(Eq. 2.1.3-2)}$$

- The adsorption analog to Raoult's law, as shown in Eq. 2.1.3-3, where z is the mole fraction in the adsorbed phase.

$$P_k=y_kP=z_k\cdot p_k^0(\pi) \qquad \text{(Eq. 2.1.3-3)}$$

- The total adsorbent loading, as shown in Eq. 2.1.3-4.

$$\frac{1}{w_{total}}=\sum_k^N\frac{z_k}{w_k^0} \qquad \text{(Eq. 2.1.3-4)}$$

- The relation between adsorbate concentration and adsorbent loading, as shown in Eq. 2.1.3-5.

$$w_k=z_k\cdot w_{total} \qquad \text{(Eq. 2.1.3-5)}$$

- The conservation of mass in the adsorbate phase, as shown in Eq. 2.1.3-6.

$$\sum_k^N z_k=1 \qquad \text{(Eq. 2.1.3-6)}$$

The success of IAST calculation depends on the fitting quality of single-component adsorption isotherm data, especially in the low-pressure region. Inaccuracies at low loading data will lead to invalid determination of the spreading pressures [61]. It is accepted that IAST provides good predictions of multi-component adsorption equilibrium for gas mixtures that are close to ideal and whose components are adsorbed at similar levels. However, when one component is adsorbed stronger than another, the adsorbed phase deviates from an ideal mixture, and IAST can not accurately describe the mixture without corrections to the model [61].

2.2 Adsorption kinetics

The overall adsorption rate is limited by the ability of adsorbate molecules to diffuse into the interior of a highly porous solid. Therefore, the evaluation of the mass transfer rate highly depends on the adsorbent type. In principle, however, the mathematical representation of the adsorption kinetics can be performed in two different ways: (1) as a global mass transfer, or (2) as a combination of different diffusion mechanisms running in parallel and/or sequentially [51]. These approaches, presented in Fig. 2.2-1, are referred to as a homogeneous or heterogeneous model [67].

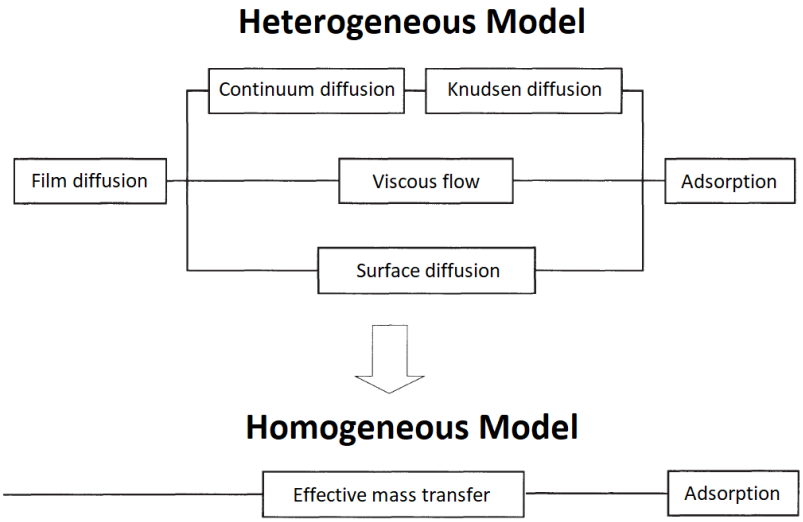

Fig. 2.2-1 Homogeneous and heterogeneous models of mass transfer kinetics

Application of a heterogeneous model requires not only detailed information about the adsorbent internal structure but also knowledge about underlying dominant mechanisms. In addition, one needs values of relevant diffusion coefficients, which determination is generally very complex and cost-intensive. Moreover, the solution of the heterogeneous model involves several sets of averaging of kinetic properties at the particle level to describe the local rates of adsorption. Those characteristics are often lost during the integration processes [37]. Besides, resolving the heterogeneous kinetic model is expected to engage more computation time and capacity in comparison to the simplified homogeneous model. On the other hand, homogeneous models are very frequently used for practical analysis of column dynamic data and for adsorptive process design because of their simplicity and analytical consistency. For those reasons, heterogeneous models are considered in cases where homogeneous models fail.

In this work, the homogeneous model of quadratic driving force (QDF) is applied to describe the adsorption kinetics. The selected model was derived from the simpler linear driving force

(LDF) equation. Therefore, both approaches are presented in order to illustrate the performed strategy. Moreover, the pressure dependence of mass transfer kinetics is considered through the implementation of the Darken correction due to utilisation of highly microporous CMS adsorbent in high-pressure PSA processes.

2.2.1 LDF model

The linear driving force model of adsorption kinetics was first introduced by Gluekauf for adsorption phenomena in chromatography [68]. It assumes that (1) the temperature and loading of the adsorbent are uniform and do not depend on the particle radius, and (2) the entire mass transport resistance is transferred to the boundary layer of the solid particle [37,51]. The graphical representation of concentration gradients within the adsorbent according to LDF model is presented in Fig. 2.2.1-1. Thus, the mass transfer rate of a single adsorbate k into a spherical adsorbent particle is quantified as shown in Eq. 2.2.1-1 [68]. The equation is applied when the diffusion process in the solid is the controlling stage, i.e. intra-particle mass transfer resistances dominate.

$$\frac{\partial w_k(t)}{\partial t} = MTC_{LDF}\left(w_k^*(t) - w_k(t)\right) = \frac{15D}{r_0^2}\left(w_k^*(t) - w_k(t)\right) \qquad \text{(Eq. 2.2.1-1)}$$

where: $w(t)$ is the average adsorbate concentration in the adsorbent particle at time t, and $w^*(t)$ is the adsorbate concentration in the adsorbent particle that would be in equilibrium with the instantaneous gas phase partial pressure of the adsorbate and the adsorbent temperature at time t. MTC_{LDF} is the effective mass transfer coefficient at adsorbate loading w and the adsorbent temperature, which can be estimated based on intra-particle diffusivity D and adsorbent particle radius r_0.

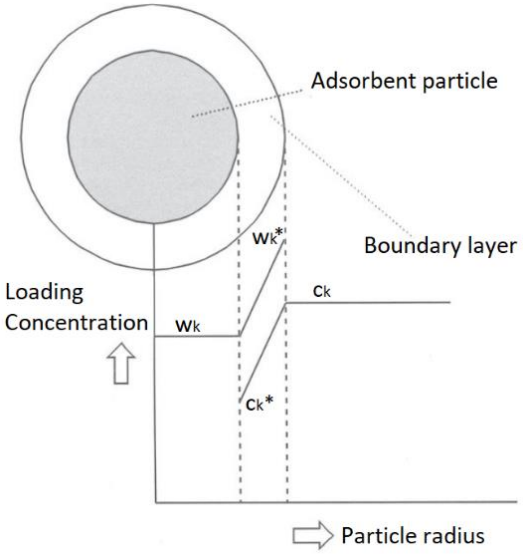

Fig. 2.2.1-1 Concentration gradients within the adsorbent particle according to LDF model [51]

Therefore, all mass transfer resistances occurring within the porous system of the adsorbent are lumped together and characterised by MTC_{LDF}. The equation was originally derived from a series expansion of the diffusion problem in a single particle subjected to a step change in external concentration, which is valid for long times of approximation, thereby for a long-term adsorption [69,70]. However, the equivalent equation can be derived considering that the

concentration profile resulting from the diffusion equation is parabolic and symmetric with respect to the particle center [69,71]. The finding suggests that the LDF model can be applied when a single diffusion resistance occurs within the adsorbent particle, or one mass transfer resistance significantly dominates. Therefore, when considering the dynamics of an adsorption column, the LDF model succeeds to describe adsorption processes characterised by a symmetrical breakthrough curve.

The model was developed for pure-component adsorption following linear or moderately curved isotherms, where conditions are maintained close to equilibrium [68]. It was shown that for a long column where constant pattern behaviour was established the LDF model was a good approximation for a system that could be described using the Langmuir isotherm [37].

Moreover, with regards to cyclic adsorption processes, when the external concentration changes fast in comparison to the diffusion time, the modification of the LDF equation was proposed, as stated in Eq. 2.2.1-2 [69,70].

$$\frac{\partial w_k(t)}{\partial t} = MTC_{LDF}\left(w_k^*(t) - w_k(t)\right) = \Omega\frac{D}{r_0^2}\left(w_k^*(t) - w_k(t)\right) \qquad \text{(Eq. 2.2.1-2)}$$

where: Ω is a function of the half-cycle time. The value of Ω increases rapidly for faster cycles.

2.2.2 QDF model

The quadratic driving force model of adsorption kinetics can be considered as the LDF approach modified by a concentration-dependent mass transfer coefficient [69,72]. According to QDF, the mass transfer rate of a single adsorbate k into adsorbent particle is estimated as shown in Eq. 2.2.2-1.

$$\frac{\partial w_k(t)}{\partial t} = MTC_{QDF}\left(\frac{w_k^*(t)^2 - w_k(t)^2}{2w_k(t)}\right) = MTC_{QDF}\frac{w_k^*(t) + w_k(t)}{2w_k(t)}\left(w_k^*(t) - w_k(t)\right) \qquad \text{(Eq. 2.2.2-1)}$$

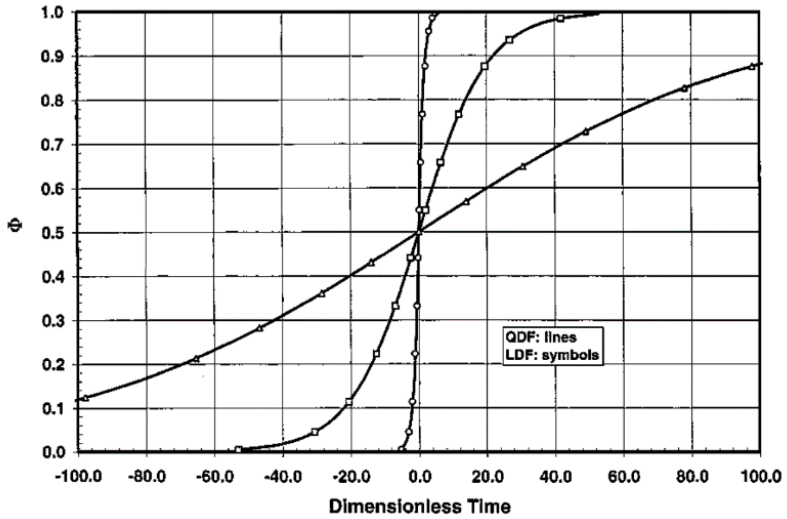

Fig. 2.2.2-1 Comparative column breakthrough curves by LDF and QDF models [37]; here Φ is gas concentration within the adsorber related to feed gas concentration

The main advantage of this model is that a better fit of the experimental breakthrough curves than LDF for low adsorptive and adsorbate concentrations in the system can be obtained [37,73] due to amplified influence of adsorbent loading. However, when considering the dynamics of an adsorption column, the breakthrough curves can be described almost quantitatively by either the LDF or the QDF models for local adsorption kinetics, as presented in Fig. 2.2.2-1 [37]. Therefore, the selection between those mass transfer models should be based on developed concentration gradients within the adsorber mass transfer zone.

2.2.3 Darken correction

The Darken correction of the intra-particle diffusivity shall be considered during characterisation of the mass transfer within highly microporous adsorbents. In the micropore (d < 2 nm), the diffusing molecules never escape from the force field of the pore wall; therefore, no bulk phase is recognised. In such circumstances, the strong concentration dependence of diffusivity occurs due to the effect of nonlinear adsorption equilibrium [32].

Since the driving force of mass transfer is always the gradient of chemical potential, the classic Fickian diffusion equation defining the surface diffusion flux can be modified, as presented in Eq. 2.2.3-1.

$$J = -D\frac{dc_{ads}}{dz} = -\frac{D_0}{R_g T}c_{ads}\frac{d\mu}{dz} \qquad \text{(Eq. 2.2.3-1)}$$

where: μ is the chemical potential, D is the diffusivity, and D_0 is the corrected diffusivity. Assuming the equilibrium state, the chemical potential corresponds to that in the ideal gas phase, following Eq. 2.2.3-2.

$$\mu = \mu_0 + RT\ln p \qquad \text{(Eq. 2.2.3-2)}$$

where: μ_0 is the reference chemical potential. By combining Eq. 2.2.3-1 and Eq. 2.2.3-2, the surface diffusion flux can be expressed as shown in Eq. 2.2.3-3, which is valid at constant temperature and pressure conditions.

$$J = -D\frac{dc_{ads}}{dz} = -D_0 c_{ads}\frac{d\ln p}{dz} \qquad \text{(Eq. 2.2.3-3)}$$

By means of this strategy, the micropore diffusivity is defined as shown in Eq. 2.2.3-4, which depends on the equilibrium isotherm between gas and solid phases. The Darken correction states that surface diffusivity D at any loading is equal to the value at zero loading D_0 multiplied by a thermodynamic correction factor $d\ln p/d\ln w$ [34]. Therefore, the application of Darken correction requires very accurate equilibrium data to evaluate secant and tangent of adsorption isotherm, as presented in Fig. 2.2.3-1.

$$D = D_0\frac{d\ln p}{d\ln c_{ads}} \sim D_0\frac{d\ln p}{d\ln w} = D_0\frac{w}{p}\frac{dp}{dw} \qquad \text{(Eq. 2.2.3-4)}$$

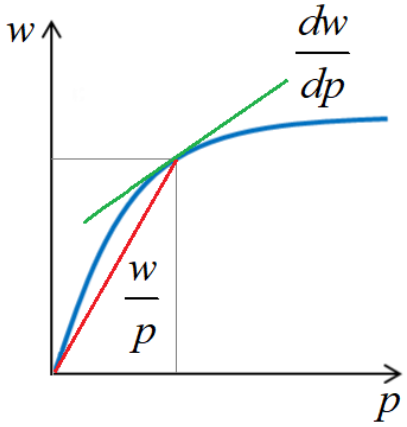

Fig. 2.2.3-1 Graphical representation of secant and tangent of the adsorption isotherm

In the limit of linear isotherm, the thermodynamic correction factor equals unity, so the micropore diffusivity becomes independent of concentration in the adsorbed phase [32].

Mass transfer in micropores is an activated process, which mainly obeys the mechanism of surface diffusion. Molecules situated at active sites along the adsorbent surface must attain enough energy to move from one active site to the next vacant active site [34]. Hence, the diffusion coefficients are strongly dependent on the binding energy of the respective adsorbent-adsorptive combination [51]. Consequently, the temperature dependence of corrected diffusivity D_0 is strong and generally follows the Arrhenius form, as presented in Eq. 2.2.3-5.

$$D_0 = A\exp\left(\frac{-E_a}{R_g T_s}\right) \qquad \text{(Eq. 2.2.3-5)}$$

3 PSA dynamic model

Pressure swing adsorption was studied mainly numerically in this work. For this reason, a mathematical model was developed enabling the simulation of the dynamic, highly interconnected steps of PSA in relevant technical configurations. By means of this strategy, new methods of process intensification can be evaluated in the future without performing extensive and time-consuming experimental research.

The dynamic simulation of nitrogen generation was performed using the process simulator Aspen Adsorption™. The implemented process flow diagram (PFD) represents a conventional twin-bed PSA set-up, as shown in Fig. 3-1. The system consists of the following elements:

(1) input stream (Feed) and output streams (Product and Tail Gas),
(2) adsorber columns (A1, A2),
(3) voids at the bottom of adsorbers (B_A1, B_A2),
(4) voids at the top of adsorbers (T_A1, T_A2),
(5) product receiver tank (R), and
(6) valves (V1 – V16).

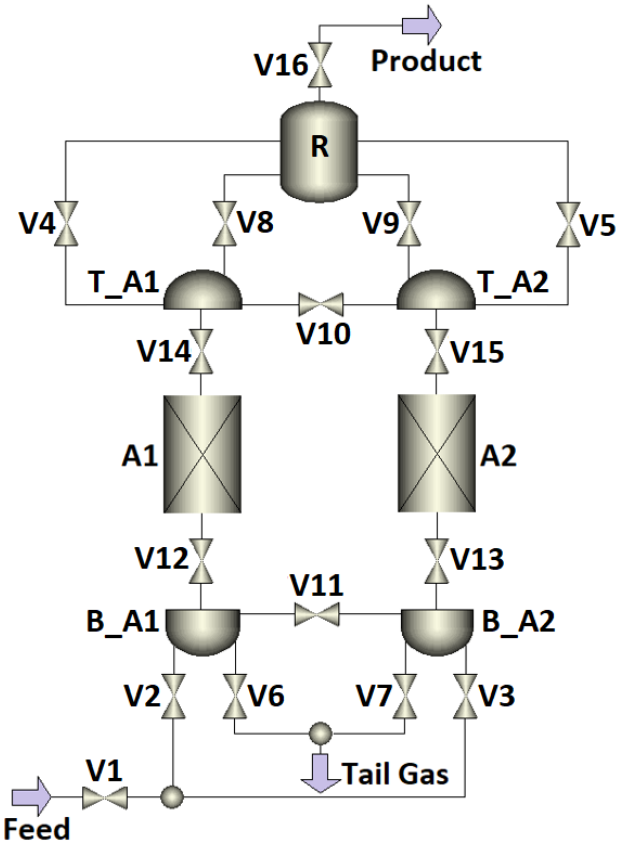

Fig. 3-1 PFD implemented in Aspen Adsorption™ process simulator

The mathematical model was developed based on the following premises:

(1) the direction of gas flow is reversible and determined by the pressure gradient,
(2) the feed gas is considered to be a two-component mixture of 20.9 vol.-% O_2 and 79.1 vol.-% N_2,
(3) the equation of state is expressed by the Peng-Robinson model,
(4) the flow pattern is described by the axially dispersed plug-flow model; the dispersion coefficient varies along the length of the adsorber,

(5) the pressure drop along the packed bed is approximated by the Ergun equation,
(6) mass, heat, and velocity gradients in the radial direction are neglected,
(7) the adsorption process is non-isothermal,
(8) the system is non-adiabatic; however, the conduction along the adsorber wall as well as heat accumulation in the wall are neglected,
(9) the porosity along the packed bed is considered constant and homogeneous,
(10) the single-component adsorption equilibrium is described by the temperature-dependent Sips isotherm,
(11) the multi-component adsorption equilibrium is estimated with the IAST approach, and
(12) mass transfer resistance at the CMS micropore-mouth dominates.

The quadratic differencing scheme (QDS) was used in order to solve the set of differential equations since it offers very accurate results with a minimal increase in simulation time for the same number of discretisation points. However, numerical results provided by the QDS oscillate under highly convective conditions. Therefore, the method is not fully suitable for the simulation of low-purity nitrogen production.

In this study, adsorbent packed beds (A1, A2) were discretised into 70 calculation nodes along their lengths.

3.1 Mass and energy balances

The overall and component mass balances applied to adsorbent beds (A1, A2) are presented in Eq. 3.1-1–3.1-2, respectively, which include terms of material accumulation in the gas phase, convection, axial dispersion, and rate of mass transfer to the solid phase.

$$\varepsilon_B \frac{\partial \rho_g}{\partial t} + \frac{\partial \left(v_g \rho_g \right)}{\partial z} + \rho_s \sum_k \frac{\partial w_k}{\partial t} = 0 \qquad \text{(Eq. 3.1-1)}$$

$$\varepsilon_B \frac{\partial c_k}{\partial t} + \frac{\partial \left(v_g c_k \right)}{\partial z} - \varepsilon_i E_{zk} \frac{\partial^2 c_k}{\partial z^2} + \rho_s \frac{\partial w_k}{\partial t} = 0 \qquad \text{(Eq. 3.1-2)}$$

The total bed voidage ε_B is calculated according to Eq. 3.1-3, which includes both interparticle and pore voids. The axial dispersion coefficient E_z is estimated according to Eq. 3.1-4, recognising the effects of molecular diffusion as well as of the gas turbulent mixing around the adsorbent pellets [67]. The model does not account for any gas channelling effect, either in the core of the packed bed or alongside the adsorber wall. The variation of molecular diffusion coefficient D_m with temperature and pressure is considered and calculated according to the Chapman-Enskog theory [74]. The method of D_m calculation is presented in Appendix 10.1.

$$\varepsilon_B = \varepsilon_i + \varepsilon_P \left(1 - \varepsilon_i \right) \qquad \text{(Eq. 3.1-3)}$$

$$E_{zk} = 0.73 D_{mk} + \frac{v_g r_p}{\varepsilon_i \left(1 + 9.49 \frac{\varepsilon_i D_{mk}}{2 v_g r_p} \right)} \qquad \text{(Eq. 3.1-4)}$$

The energy balances of gas and solid phases are presented in Eq. 3.1-5–3.1-6, respectively.

$$\varepsilon_B C_{vg}\rho_g \frac{\partial T_g}{\partial t} + C_{vg} v_g \rho_g \frac{\partial T_g}{\partial z} - \varepsilon_i k_{gz} \frac{\partial^2 T_g}{\partial z^2} + P\frac{\partial v_g}{\partial z} + ha_p\left(T_g - T_s\right) + \frac{4h_w}{D_B}\left(T_g - T_a\right) = 0 \quad \text{(Eq. 3.1-5)}$$

$$C_{ps}\rho_s \frac{\partial T_s}{\partial t} - k_{sz}\frac{\partial^2 T_s}{\partial z^2} + \rho_s \sum_k \left(C_{pak} w_k\right)\frac{\partial T_s}{\partial t} + \rho_s \sum_k \left(\Delta H_k \frac{\partial w_k}{\partial t}\right) - ha_p\left(T_g - T_s\right) = 0 \quad \text{(Eq. 3.1-6)}$$

Specifically, Eq. 3.1-5 includes terms of enthalpy accumulation in the gas phase, convection, axial thermal conduction, thermal effect of compression, and heat transfer between gas and solid phases. The variation of gas thermal conductivity k_{gz} with the temperature is considered and calculated by empirical equation [75] as presented in Appendix 10.2. The gas-solid heat transfer coefficient h is implemented as a function of Reynolds and Prandtl numbers, according to the method presented in Appendix 10.3. Furthermore, the heat exchange between gas in the column and the environment is included in the gas phase energy balance. The equation involves the gas-wall heat transfer coefficient (HTC) h_W which combines: (1) heat transfer resistances of the boundary layer between gas and wall on the inside of the column, (2) the material of the column wall, and (3) boundary layer between the outer column wall and the ambient. The specific particle surface a_p is calculated according to Eq. 3.1-7.

$$a_p = \frac{3\left(1-\varepsilon_i\right)}{r_p} \quad \text{(Eq. 3.1-7)}$$

Eq. 3.1-6 includes terms of enthalpy accumulation in the solid phase, axial thermal conduction, heat of adsorbed phase, thermal effect of the adsorption process, and heat transfer between gas and solid phases. The alteration of the adsorbed phase heat capacity C_{pak} with the temperature is considered and calculated by an empirical equation [75,76] as presented in Appendix 10.4.

Tab. 3.1-1 Parameters of the PSA dynamic model

Packed bed diameter	D_b [mm]	66
Average packed bed length	H_b [mm]	581
Average packing density	ρ_s [kg/m3]	711
Inter-particle voidage	ε_i [m^3 void/m^3 bed]	0.404
Intra-particle voidage	ε_p [m^3 void/m^3 pellet]	0.234
Total bed voidage	ε_B [m^3 (void+pore)/m^3 bed]	0.543
Average adsorbent particle radius	r_p [mm]	0.830
Specific particle surface	a_p [m^2 particle area/m^3 pellet]	2155
Adsorbent thermal conductivity	k_{sz} [W/m/K]	0.675
Adsorbent specific heat capacity	C_{ps} [J/kg/K]	880
HTC between gas and adsorber wall	h_w [W/m^2/K]	50
Product receiver volume	V_R [L]	12
Product receiver diameter	D_R [mm]	220
Mass of product receiver shell	m_R [kg]	4.8
Heat capacity of the product receiver shell	C_{pR} [J/kg/K]	500
HTC between gas and product receiver shell	h_R [W/m^2/K]	50
HTC between product receiver shell and ambient	h_{Ra} [W/m^2/K]	20
Bottom-void volume	V_B [cm^3]	18.5
Top-void volume	V_T [cm^3]	35

Mass and energy are accumulated within the product receiver tank (R) and adsorber voids (B_A1, B_A2, T_A1, T_A2). The ideal mixing of gas within each volume is assumed. In this

study, adsorber voids are considered to operate under adiabatic conditions since any energy transfer between columns and environment is included in the energy balance of adsorbers (A1, A2). Additionally, the valve model (V) does not account for any material holdup but relates the pressure drop to the gas flow rate through an orifice, which is discussed in more detail in Chapter 3.2. The temperature change of gas flowing across the valve model is estimated based on the Joule-Thomson effect.

The remaining parameters of PSA dynamic model are listed in Tab. 3.1-1.

3.2 Pressure drop

Generally, in any conventional PSA plant, three sources of pressure drop are recognised: (1) uncontrolled flow resistances in the piping system, e.g. pipes, bends, in-line filters, connectors, or adsorber column elements as perforated plates or sieves for the packed-bed support; (2) controlled flow resistances in the piping system, i.e. the control valves installed for a flow rate regulation of particular streams; and (3) the adsorbent fixed-bed. Therefore, the quantification of the pressure drop resulting from the aforementioned flow resistances is considered.

In order to signify particular flow resistances occurring in the piping system, both uncontrolled and controlled, the valve models V are implemented in the process simulator, as shown in Fig. 3.1. Depending on the function of objects assembled in the PSA plant, the Aspen Adsorption™ valve model V simulates the action of either a mass flow controller, a ball valve, or a control valve. When simulating the action of the mass flow controller, the gas flow rate downstream of the valve V is kept constant. In the case of simulating the action of the ball valve, the gas flow across the valve V is not associated with a pressure drop. Once the valve model V simulates the action of the control valve, the gas flow rate is expressed as a linear function of the pressure drop across the orifice, as shown in Eq. 3.2-1. Adjustment of the flow coefficient *Cv* allows the simulation of a specific pressure drop caused by the gas flowing through particular objects creating the flow resistance, which is considered either uncontrolled and controlled, e.g. pipe connectors, in-line filters, flow meters, manual needle valves, or adsorber column armature, such as perforated plates, sieves, etc.

$$F = Cv \cdot \Delta P \qquad \text{(Eq. 3.2-1)}$$

The experimental evaluation of pressure drop in the PSA piping system was performed in process conditions of 8 bar abs and 20 °C in order to find individual flow coefficients of implemented valve models V in the process simulator. Sensitivity studies have confirmed that the pressure build-up and fall-off during the PSA process are independent from the product flow rate in the investigated nitrogen purity range.

As a reference, the process with minimised controlled flow resistances in the PSA piping system was selected. In order to do so, control valves in all pipelines were fully opened. Accordingly, all valve models V in the process simulator representing controlled flow resistances were adjusted to simulate the action of the ball valve. By means of this strategy, the quantification of uncontrolled flow resistances was practicable. Individual flow coefficients *Cv* of particular valve models were found by fitting of simulated pressure curves to corresponding experimental pressure curves measured at the top of two adsorbers columns, as shown in Fig. 3.2-1. Moreover, the correctness of applied *Cv* values was confirmed by comparison of simulated and

experimental pressure drop across objects generating uncontrolled flow resistances in the PSA piping system, as shown in Fig. 3.2-2. The test method is described in detail in Appendix 10.5.

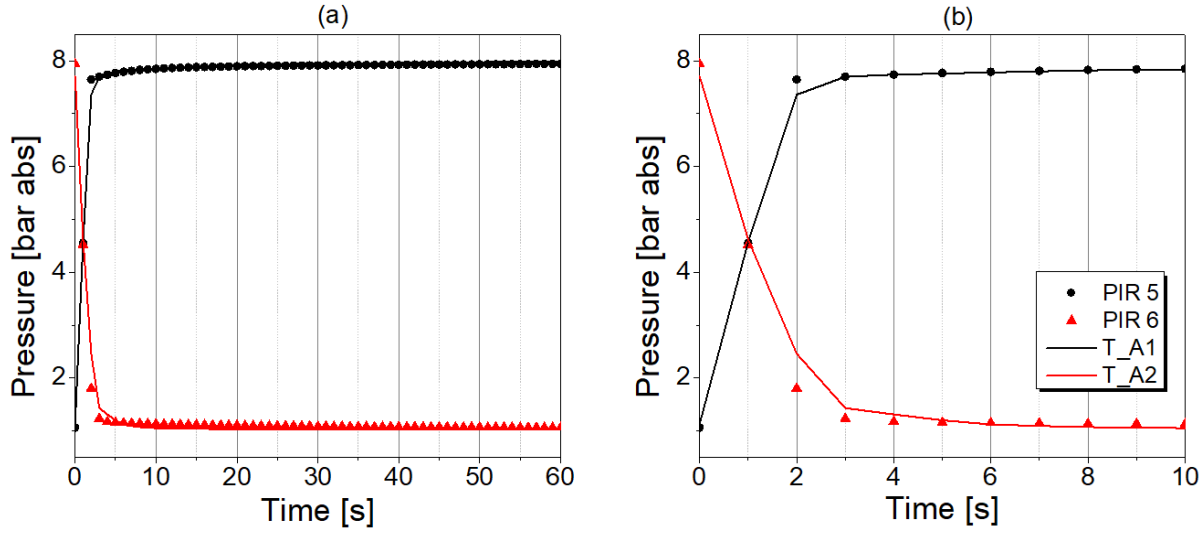

Fig. 3.2-1 Experimental and simulated pressure profiles at the top of adsorber columns with minimised controlled flow resistances in the PSA piping system: (a) during the entire PSA half-cycle, (b) during the initial phase of the PSA half-cycle

Subsequently, individual flow coefficients *Cv* of particular valve models representing controlled flow resistances in the PSA piping system were found analogously, by fitting of simulated pressure curves to corresponding experimental pressure curves measured at the top of two adsorbers columns, as presented in Fig. 3.2-3.

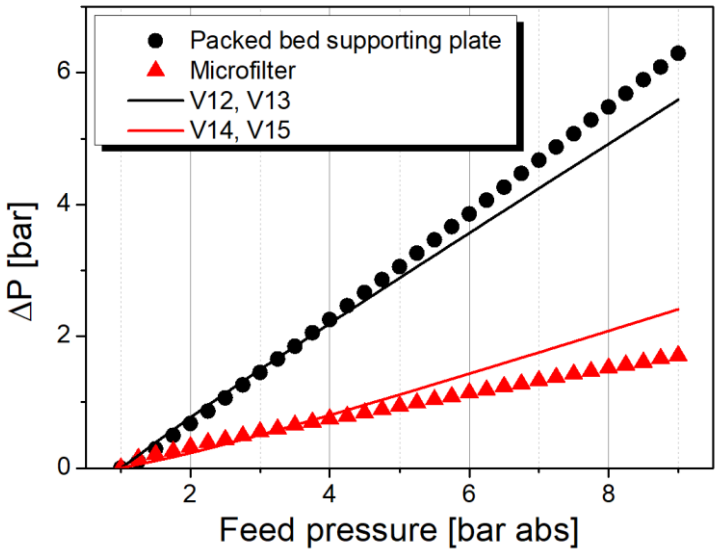

Fig. 3.2-2 Experimental and simulated pressure drop resulting from uncontrolled flow resistances in the PSA piping system at different feed stream pressure

Details of flow coefficients adjustment are presented in Appendix 10.6. Individual functions of applied valve models V, together with fitted *Cv* values representing the flow resistances in the piping system of considered PSA set-up, are listed in Tab. 3.2-1.

$$-\frac{\partial P}{\partial z}=\frac{1.75\times10^{-5}M\rho_g\left(1-\varepsilon_i\right)}{2r_p\psi\varepsilon_i^3}v_g^2+\frac{1.50\times10^{-3}\left(1-\varepsilon_i\right)^2\mu}{\left(2r_p\psi\right)^2\varepsilon_i^3}v_g \qquad \text{(Eq. 3.2-2)}$$

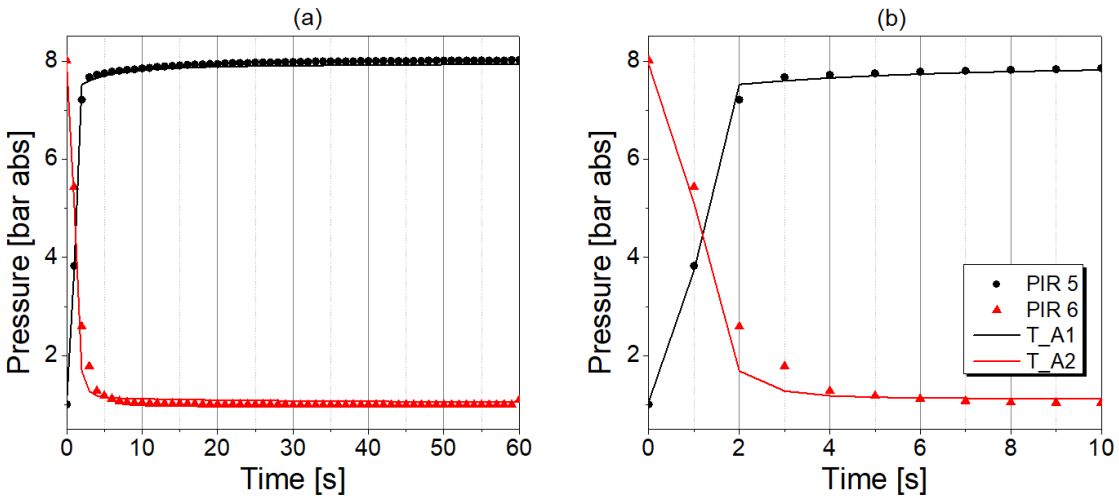

Fig. 3.2-3 Experimental and simulated pressure profiles at the top of adsorber columns with adjusted controlled flow resistances in the PSA piping system: (a) during the entire PSA half-cycle, (b) during the initial phase of the PSA half-cycle

Contemporaneously, the pressure drop caused by gas flow across the adsorbent fixed-bed is evaluated. In this study, the gas' superficial velocity in the adsorbent fixed-bed is related to local pressure gradients along the adsorber length which are estimated according to the momentum balance expressed by the Ergun model as shown in Eq. 3.2-2.

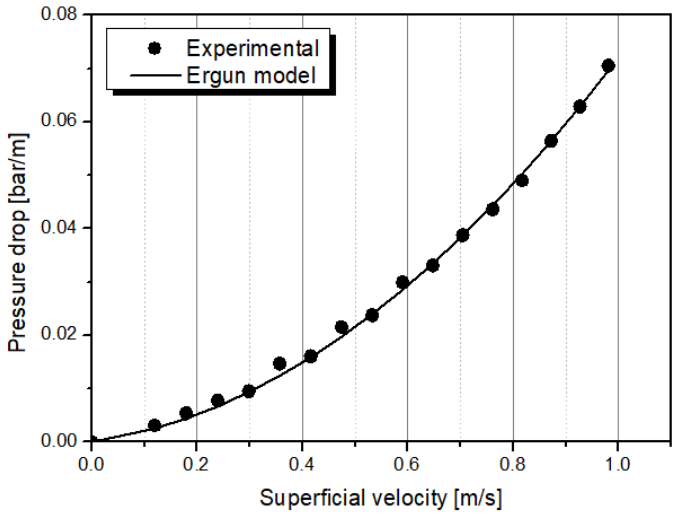

Fig. 3.2-4 Experimental pressure drop along the CMS packed bed represented by the Ergun model

Tab. 3.2-1 Functions of linear valve models V applied in the process simulator

Valve model	Function / Actual flow resistance	Action	Cv [kmol/s/bar]
V1 *	Feed stream flow meter	Control valve	9.0×10^{-4}
V2, V3	Feed pipeline	Control valve	5.0×10^{-1}
V4, V5	Product pipeline	Ball valve	-
V6, V7	Tail-gas pipeline	Ball valve	-
V8, V9	Purge stream flow controller	Flow controller	-
V10, V11	Equalisation pipelines	Control valve	2.5×10^{-5}
V12, V13 *	Packed bed supporting plate	Control valve	1.1×10^{-4}
V14, V15 *	Microfilter	Control valve	9.5×10^{-4}
V16	Product stream flow controller	Flow controller	-

* Represents an uncontrolled flow resistance in the piping system

The pressure drop along the packed bed was studied empirically and parameters of the Ergun equation were adjusted. The test method is described in detail in Appendix 10.7, with the results shown in Fig. 3.2-4. Since the interparticle voidage ε_i and the adsorbent particle radius r_p were determined experimentally by statistical analysis with 100 adsorbent pellets, the adsorbent shape factor ψ was considered here as the sole fitting parameter, which equals 1.959 [-]. The analysis of pellets geometry is reported in Appendix 10.8.

3.3 Adsorption equilibrium

Knowledge of adsorption equilibria is of essential importance in order to understand an adsorption process, since it characterises the amount adsorbed on the solid surface of a particular adsorbent at thermodynamic equilibrium. Moreover, the data of pure components adsorption equilibrium allow further evaluation of multicomponent adsorption equilibrium as well as estimation of mass transfer kinetics in the considered system, which is especially relevant for the mixture separation studies [34].

In this work, the thermodynamic equilibrium was measured gravimetrically on an IsoSORP magnetic suspension balance from Rubotherm. At first, a sample of the CMS adsorbent was pretreated, i.e. subjected to vacuum and heating in order to remove preadsorbed gases and moisture. Ahead of the measurement of the isotherm, the exact sample volume was determined by a buoyancy analysis in helium at the respective temperature. The equilibrium data were collected in the pressure range of 0 – 20 bar abs at temperature levels of 20, 40, and 60 °C. The adsorption of pure oxygen and pure nitrogen on the CMS adsorbent was tested. The experimental results were fitted to the temperature-dependent Sips isotherm model [34] presented in Eq. 3.3-1–3.3-4, since it provides a superior data description with respect to other common isotherm models in the studied pressure range. Even though the empirical Sips model is not thermodynamically consistent given that it does not exhibit a linear form at very low partial pressures, it is considered suitable for describing many heterogeneous adsorption systems at a wide range of pressures as it properly predicts a finite amount adsorbed when the gas pressure is sufficiently high [77].

$$w_k^* = w_{sk}^* \frac{\left(b_k p_k\right)^{1/n_k}}{1+\left(b_k p_k\right)^{1/n_k}}; \qquad w_{sk}^* = w_{s0k}^* \exp\left[\chi_k\left(1-\frac{T}{T_0}\right)\right] \qquad \text{(Eq. 3.3-1; 3.3-2)}$$

$$b_k = b_{0k} \exp\left[\frac{Q_k}{R_g T_0}\left(\frac{T_0}{T}-1\right)\right]; \quad \frac{1}{n_k} = \frac{1}{n_{0k}} + \alpha_k\left(1-\frac{T_0}{T}\right) \qquad \text{(Eq. 3.3-3; 3.3-4)}$$

Using the method of least squares, the isotherms' parameters were found. The results are listed in Tab. 3.3-1. The experimental equilibrium curves described by the Sips isotherm model are shown in Fig. 3.3-1. No significant difference in the course of oxygen and nitrogen isotherms was observed. Nevertheless, the measurement of thermodynamic equilibrium exposes a limited applicability range of Sips isotherm at low pressures. The experimental equilibrium loading is estimated with a highest relative error of 51.74 % in the case of oxygen adsorption at 20 °C detected at 0.0094 bar abs; and 22.53 % in the case of nitrogen adsorption at 40 °C detected at 0.1110 bar abs. At high pressures, equilibrium loading is predicted very accurately with respect to both components.

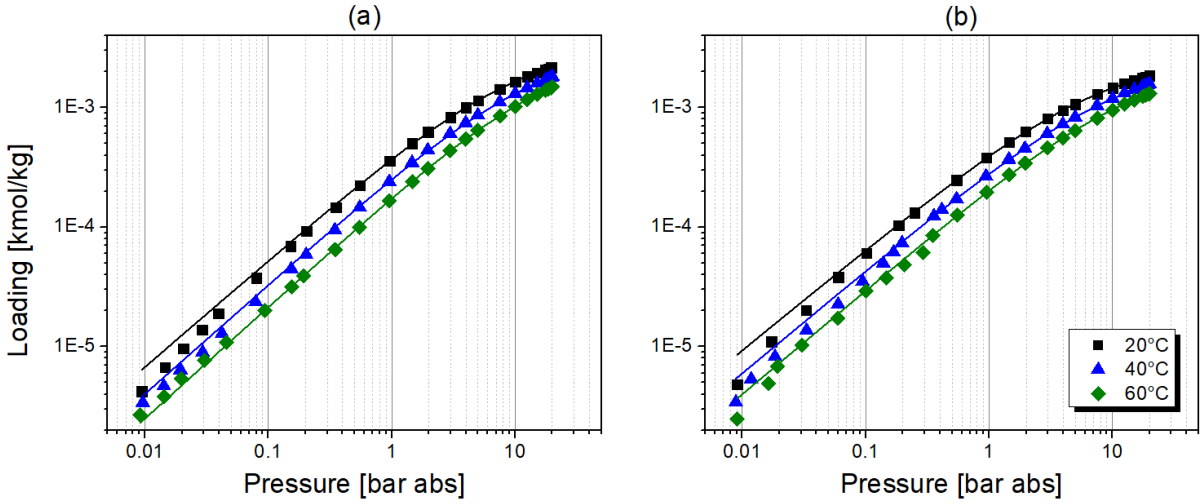

Fig. 3.3-1 Experimental adsorption isotherms of (a) oxygen and (b) nitrogen on the CMS represented by the Sips model

As presented in Fig. 3.3-2, nitrogen exhibits a slightly enhanced equilibrium affinity to the CMS adsorbent at low pressures (< 2 bar abs), whereas the opposite effect is observed at higher pressures, regardless of the adsorption temperature.

Tab. 3.3-1 Sips isotherm parameters of oxygen and nitrogen adsorption on CMS

	$w_{s0}^{*}\,[kmol/kg]$	$\chi[-]$	$b_0[1/bar]$	$Q[kJ/kmol]$	$n_0[-]$	$\alpha[-]$
O_2	3.384×10^{-3}	1.104	9.436×10^{-2}	1.222×10^{4}	1.120	3.341×10^{-1}
N_2	2.707×10^{-3}	1.146	1.205×10^{-1}	1.187×10^{4}	1.185	2.263×10^{-1}

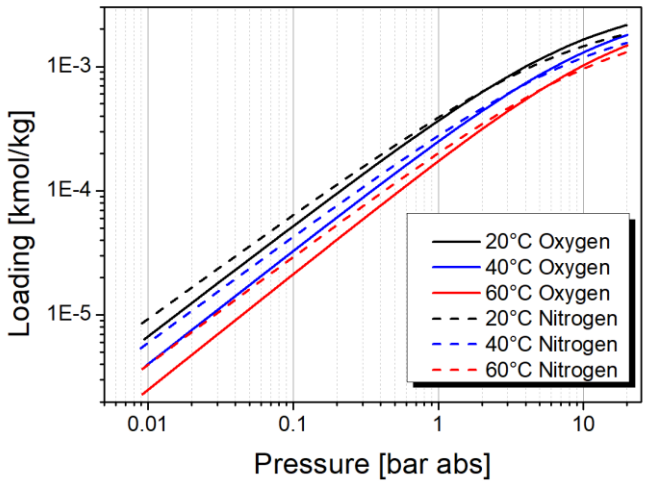

Fig. 3.3-2 Comparison of adsorption isotherms of oxygen and nitrogen on the CMS represented by the Sips model

In this work, the ideal adsorption solution theory (IAST) is selected since it is one of the most reliable, respected, and frequently-used methods for predicting multicomponent adsorption equilibrium using only adsorption isotherms of pure components [61]. The method is thermodynamically consistent as an adsorption analog to Raoult's law applies. However, the IAST is not a universal method of predicting multi-component adsorption equilibria and should be carefully validated for systems with molecules that vary significantly in size, polarity, or adsorption interactions. Moreover, the method could also not provide accurate predictions for adsorbents with heterogeneous surfaces [61]. For those reasons, the adsorption of a synthetic

air mixture (20 vol.-% O_2 and 80 vol.-% N_2) was experimentally studied in order to validate the correctness of the multi-component calculation by the IAST approach.

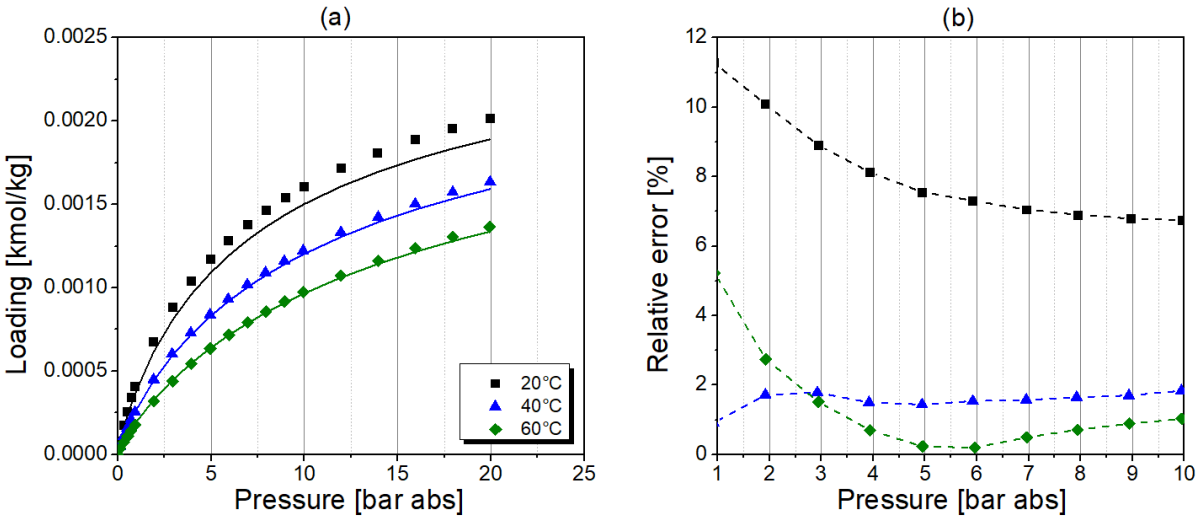

Fig. 3.3-3 (a) experimental adsorption isotherms of synthetic air mixture on the CMS represented by the IAST model; (b) the absolute value of relative error of the equilibrium loading with the IAST model

The equilibrium data were collected in the pressure range of 0 – 20 bar abs at temperature levels of 20, 40, and 60 °C. The results are plotted in Fig. 3.3-3a. The IAST calculation underestimates the experimental multi-component adsorption equilibrium data in the whole pressure range at 20 and 40 °C. At 60 °C, the experimental data are overestimated up to about 5 bar abs and underestimated posteriorly. However, the accuracy of the equilibrium prediction exhibited here is acceptable. As presented in Fig. 3.3-3b, in the pressure range of practical application of the PSA system i.e. 1 – 10 bar abs, the maximal absolute relative error of IAST estimation equals 11.2 % at 20 °C, 1.84 % at 40 °C, and 5.07 % at 60°C. Moreover, considering the PSA operation, increased deviations in the equilibrium loading are observed during the desorption rather than the adsorption step. For that reason, the relative error at atmospheric pressure level is significantly higher than at adsorption pressure levels while considering 20 and 60 °C. At 40 °C, the estimation error is rather insensitive to the variation of system pressure.

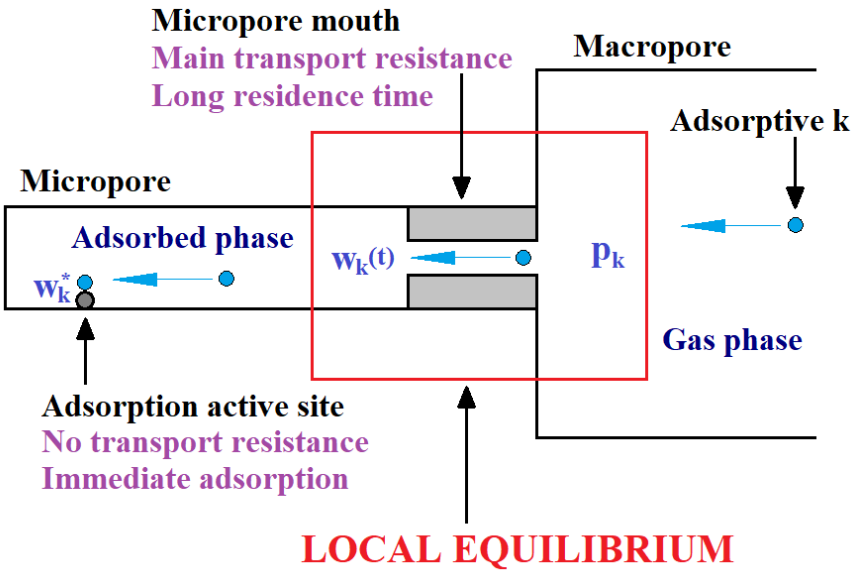

Fig. 3.3-4 Graphical representation of the local equilibrium concept

Additionally, according to the model assumption, which states that mass transfer resistance at the CMS micropore-mouth dominates, the existence of a local equilibrium between the component concentration in the gas and solid phases is accepted. Since the mass transfer is the rate-limiting step rather than adsorption kinetics, the adsorption and desorption rates are considered to be much faster than the rate at which the steady-state is achieved within the adsorbent particle [78]. Therefore, the equilibrium is reached locally in a short time span, which is expressed in Eq. 3.3-5 and Fig. 3.3-4. This postulation is particularly relevant with respect to the slow-diffusing component of the gas mixture.

$$w_k \cong w_k^* = w_{sk}^* \frac{\left(b_k p_k\right)^{1/n_k}}{1+\left(b_k p_k\right)^{1/n_k}} \qquad \text{(Eq. 3.3-5)}$$

3.4 Isosteric heat of adsorption

Prior knowledge regarding isosteric heat of adsorption of pure components in the gas mixture is particularly important for PSA technology since it measures temperature changes within the adsorber during the adsorption (exothermic) and desorption (endothermic) steps. Therefore, the evaluation of adsorption equilibria and kinetics corresponding to local temperature levels in the system is feasible [79].

$$\left(-\Delta H_k\right)_\theta = R_g \frac{\partial \ln p_k}{\partial\left(1/T_g\right)} \qquad \text{(Eq. 3.4-1)}$$

$$\theta_k = \frac{w_k}{w_{sk}^*} = \frac{w_k}{w_{s0k}^* \exp\left[\chi_k\left(1-\frac{T}{T_0}\right)\right]} \qquad \text{(Eq. 3.4-2)}$$

In this work, the isosteric heat of adsorption was estimated based on the pure component adsorption isotherms with the Clausius-Clapeyron method displayed in Eq. 3.4-1. The effect of loading as well as temperature on the adsorption enthalpy was considered since the adsorbent surface coverage θ depends on the process temperature as stated in Eq. 3.4-2. The results are presented in Fig. 3.4-1.

Tab. 3.4-1 Equation and fitting parameters describing the adsorption enthalpy of oxygen and nitrogen on the CMS

	$-\Delta H_k = Aw_k^{\,5}\exp\left(\frac{G}{T}\right) + Bw_k^{\,4}\exp\left(\frac{H}{T}\right) + Cw_k^{\,3}\exp\left(\frac{I}{T}\right) + Dw_k^{\,2}\exp\left(\frac{J}{T}\right) + Ew_k\exp\left(\frac{K}{T}\right) + F\exp\left(\frac{L}{T}\right)$					
	A × 10^{-14}	**B × 10^{-12}**	**C × 10^{-9}**	**D × 10^{-6}**	**E × 10^{-3}**	**F × 10^{-1}**
O_2	2.384	-1.474	4.914	-8.498	8.454	-1.490
N_2	3.906	-1.826	5.312	-7.997	6.931	-1.363
	G × 10^{-1}	**H × 10^{-1}**	**I × 10^{-1}**	**J**	**K × 10^{-1}**	**L × 10^{-1}**
O_2	-1.084	6.320	4.032	2.323	-2.619	2.584
N_2	-1.087	8.365	4.669	2.793	-1.921	2.548

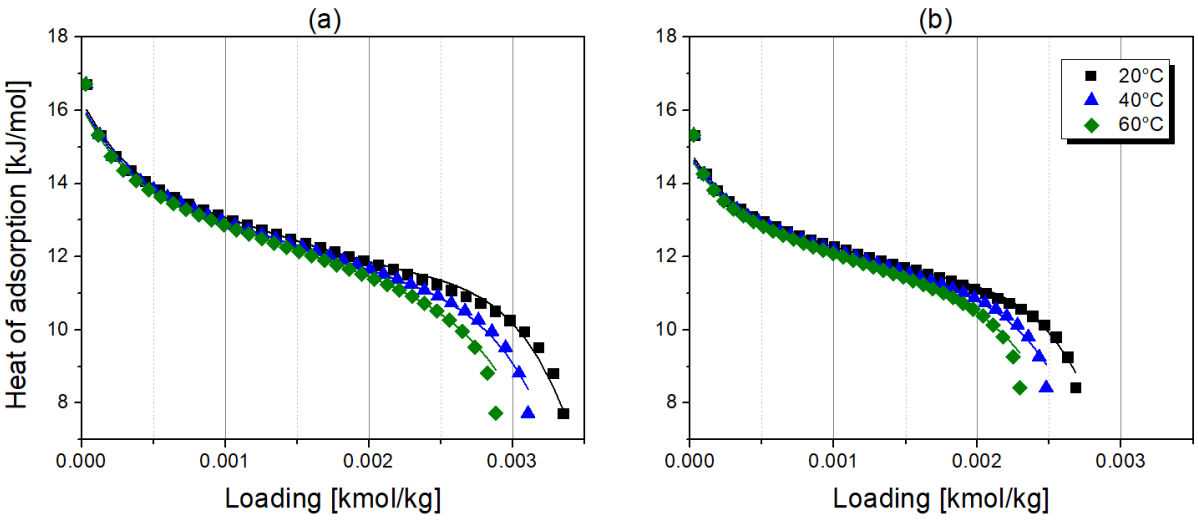

Fig. 3.4-1 Heat of adsorption of (a) oxygen and (b) nitrogen evaluated by the Clausius-Clapeyron method; represented by polynomial functions

The adsorption enthalpy decreases with the surface coverage, pointing out the heterogeneous structure of the CMS adsorbent. Both studied components exhibit comparable adsorption enthalpy which does not exceed 17 kJ/mol at minimum loading. Moreover, the temperature effect on isosteric heat of adsorption proved to be insignificant except for the adsorbent near-saturation condition. A polynomial function was implemented in the process simulator to calculate the heat of adsorption. The resulting equation and fitting parameters are given in Tab. 3.4-1.

3.5 Mass transfer kinetics

In the case of nitrogen generation via kinetically-controlled air separation in the PSA technology, the crucial aspect is the correct representation of the mass transfer kinetics in highly microporous CMS adsorbent. The classification of pore size as recommended by IUPAC is often used to delineate the range of pore size based on the diameter of their cross-section *d*:

- Micropores $d < 2$ nm
- Mesopores $2 \text{ nm} < d < 50$ nm
- Macropores $d > 50$ nm

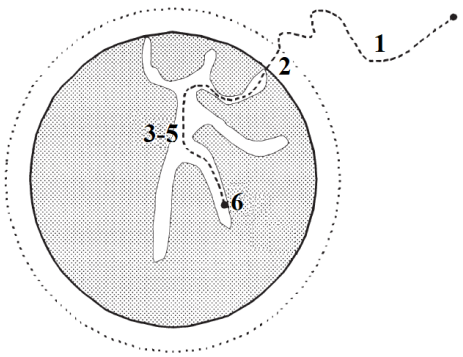

Fig. 3.5-1 Mass transfer in adsorbent particle [51]

Generally, the mass transport from bulk phase to adsorption active sites of a porous solid is divided into several steps according to particular diffusion mechanism at different spatial conditions, which are: (1) convection to the boundary layer of the adsorbent; (2) film diffusion in the adsorbent boundary layer; (3) continuum diffusion in macropores; (4) Knudsen diffusion in mesopores*; (5) surface diffusion in micropores; and (6) adsorption on active sites, as visualised in Fig 3.5-1 [51]. Furthermore, multiple diffusion mechanisms contribute simultaneously, especially considering the intraparticle transport. Mass transfer resistances occur at each step; however, their significance depends on the inner geometry of the adsorbent as well as on the physicochemical properties of the adsorbate. Therefore, if mass transfer resistance at a specific step notably dominates, the individual diffusion mechanism can be considered to be rate-limiting in the system.

In highly microporous CMS adsorbent, micropore entrances (so-called micropore-mouths) are intentionally narrowed in order to enable effective mixtures separation by the sieving effect on the basis of molecules size and shape [80]. Details of the adsorbent internal structure are presented in Chapter 4.1. It is assumed that the mass transfer resistance at the CMS micropore-mouth dominates since the diameter of micropore entrances is the smallest within the entire pore system. Therefore, the potential energy of molecules is most likely to increase rapidly at that place which is associated with the occurrence of repulsion forces [81]; consequently, further micropore penetration and transport to adsorbent active sites are significantly inhibited. Hence, the rate-limiting step of mass transport is the micropore diffusion which applies to both micropore-mouths of predominant resistances, and micropores themselves of minor resistances. This statement is in agreement with the majority of publications which confirm that in the case of kinetically-controlled air separation on CMS adsorbents the rate-controlling step obeys mechanisms of the surface barrier, the diffusional molecular transport within micropores, or superposition of both [44–46,82–87].

The approach of a lumped resistance of the mass transfer was selected, with the rate of transport expressed as a quadratic function of the solid film loading, as presented in Eq. 3.5-1. The applied quadratic driving force (QDF) empirical model is adequate for process simulation because the detailed characteristics of local adsorption kinetic models, e.g. Fickian diffusion, are lost during repeated averaging of its properties needed to obtain the final process performance [37]. Moreover, since the QDF approach eliminates the integration step at the particle level, its implementation significantly reduces the computational time required for realistic process simulation. It was confirmed that the QDF model provides a better approximation of mass transfer of pure gases within the microporous adsorbents than the linear driving force (LDF) approach at low adsorbate concentration [37,73]. For this reason, the quadratic driving force is the model of choice in this work since the generation of high-purity nitrogen is considered; therefore, the oxygen concentration is very low downstream the mass transfer zone in the adsorber column. Since both LDF and QDF models describe the parabolic concentration profile within the adsorbent particle similarly, in this work the mass transfer coefficient (MTC) follows the Glueckauf approximation [70] as shown in Eq. 3.5-2.

* Knudsen diffusion occurs when the pore diameter is smaller than the mean free path of the diffusing gas molecules. The free mean path of oxygen and nitrogen at 1 bar abs, 25 °C equals 64.5 nm and 61.8 nm, respectively [67].

$$\frac{\partial w_k}{\partial t} = MTC_k \frac{w_k^{*2} - w_k^2}{2w_k} \qquad \text{(Eq. 3.5-1)}$$

$$MTC = \frac{D_e}{r_p^2} \qquad \text{(Eq. 3.5-2)}$$

It is assumed that the effective diffusion coefficient D_e, which characterises macroscopically the mass diffusion across the entire pore space of adsorbent, corresponds to the surface diffusion coefficient D_s, as shown in Eq. 3.5-3. For that reason, the mass transfer in micropores mainly obeys the surface diffusion mechanism.

$$D_e \cong D_s \qquad \text{(Eq. 3.5-3)}$$

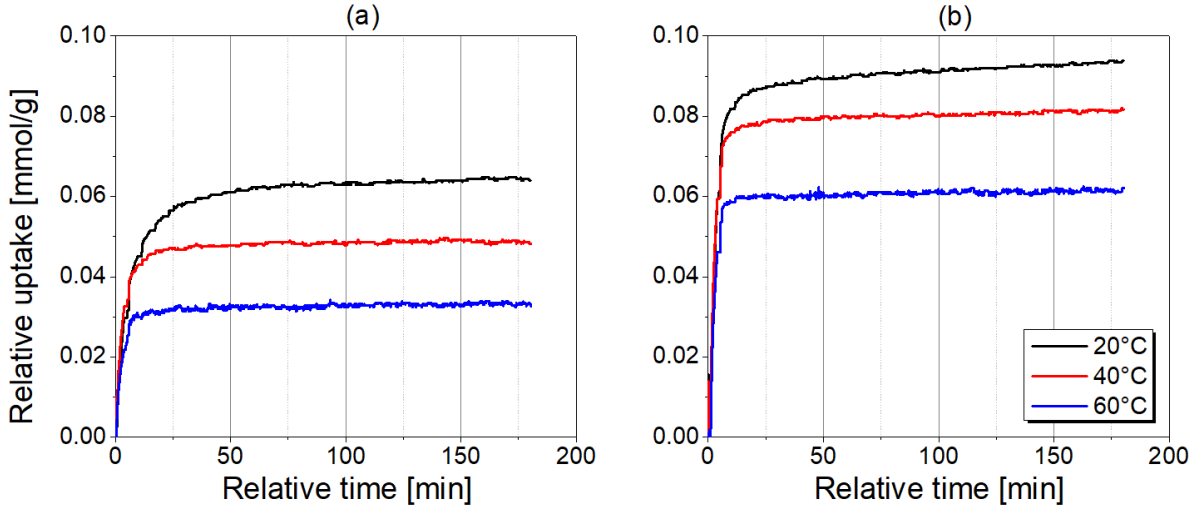

Fig. 3.5-2 Kinetic curves of relative uptake calculated from adsorption isotherm data of synthetic air: (a) at 0.92 bar abs, (b) at 7.94 bar abs

Several studies acknowledged that the mass transfer rate within the CMS adsorbent increases with pressure [88–91] which is exceptionally relevant in the case of PSA systems operated under elevated pressure in the range of 5 – 15 bar abs. The explanation of this phenomenon has been considered as an effect of surface diffusion mechanism in which strong dependence of surface concentration or pressure was confirmed as the effect of system nonlinearity [92]. In this work, the relationship between mass transfer kinetics and pressure has been recognised based on the experimental investigation of adsorption isotherms of synthetic air. The kinetic curves of relative uptake have been plotted at pressure levels of 0.92 and 7.94 bar abs which correspond to standard PSA operating pressure levels during adsorption and desorption, respectively. The results are presented in Fig. 3.5-2. The equilibrium adsorbent loading is reached faster in the system at elevated pressure and temperature conditions.

For that reason, the Darken-relation was selected to estimate diffusion coefficients in the studied system [93]. The approach was developed based on the assumption of chemical potential gradient as the driving force of the mass transfer which depends on the equilibrium isotherm between gas and solid phases. It states that surface diffusivity at any loading is equal to the value at zero loading multiplied by a thermodynamic correction factor [34] as presented in Eq. 3.5-4.

$$D_s = D_0 \frac{d\ln p}{d\ln w} = D_0 \frac{w}{p}\frac{dp}{dw} \qquad \text{(Eq. 3.5-4)}$$

Therefore, the Darken approach for the estimation of pressure-dependent mass transfer kinetics requires the precise approximation of thermodynamic equilibrium data for the subsequent quantification of adsorption isotherm slope. Consequently, imprecisions presented in Chapter 3.3 would affect the accuracy of the kinetic model in the considered system. Since micropore diffusion is an activated process, an Arrhenius term is adopted in order to describe the temperature dependence of surface diffusivity at zero loading [32] as shown in Eq. 3.5-5.

$$D_0 = A\exp\left(\frac{-E_a}{R_g T_s}\right) \qquad \text{(Eq. 3.5-5)}$$

In summary, the mass transfer rate of a single component in the considered system is calculated according to Eq. 3.5-6. Implementation of equations describing the mass transfer kinetics in the process simulator is presented in Appendix 10.9. Factors of sorption frequency A_k and sorption activation energy E_{ak} were considered as model fitting parameters which are presented in Tab. 3.5-1. Therefore, the diffusion process of oxygen in CMS adsorbent is much faster in comparison to the nitrogen, as was previously confirmed in many publications [85,86,91].

$$\frac{\partial w_k}{\partial t} = \left[\frac{1}{r_p^2} A_k \exp\left(\frac{-E_{ak}}{R_g T_s}\right)\frac{w_k}{p_k}\frac{dp_k}{dw_k}\right]\frac{w_k^{*2} - w_k^2}{2w_k} \qquad \text{(Eq. 3.5-6)}$$

Since the kinetic diameters of oxygen (3.46 Å) and nitrogen (3.64 Å) are relatively similar, the large discrepancy in kinetic parameters can only be explained by the acentric factor which characterises a molecule with respect to both geometry and polarity. It was suggested that the paramagnetic properties of oxygen give rise to strong attraction force to carbon atoms on the inter-surface of the CMS adsorbent, thus the mass transport proceeds rapidly [88]. Nitrogen, however, is supposed to dimerise in the CMS pores and create large van der Waals molecules, thus its mass transfer rate is inhibited [88]. Moreover, since the heat of adsorption of oxygen on CMS is larger than its sorption activation energy, jumps between active sites on the surface of adsorbent can be admitted as the controlling process of the mass transfer [33]. On the other hand, the heat of adsorption of nitrogen on CMS is smaller than its sorption activation energy, indicating the dominance of repulsive forces at micropore entrances, recognised as the controlling step [33]. These considerations may acknowledge precedent discussion about the nature of oxygen and nitrogen kinetics in micropores of CMS.

Tab. 3.5-1 Kinetic parameters of oxygen and nitrogen

	Oxygen	**Nitrogen**
Arrhenius pre-exponential factor A/r_p^2 [1/s]	1.7534	118.8268
Sorption frequency A [m^2/s]	1.208×10^{-6}	8.186×10^{-5}
Activation energy E_a [kJ/kmol]	1622.33	25098.55

4 Experimental program

Pressure swing adsorption was also studied experimentally in order to validate the developed mathematical model, presented in Chapter 3.

4.1 Selected adsorbent

The generation of nitrogen via PSA technique is performed by contacting the compressed air with a carbon molecular sieves (CMS) which is commonly manufactured by chemical vapour deposition (CVD) of hydrocarbons on highly microporous activated carbon precursor [94–96]. By means of this technology, micropore entrances become artificially narrowed by the superstructure of pyrolytic carbon, creating physical obstacles within the adsorbent pore system, so-called micropore-mouths [97]. Therefore, the pore system consists mainly of micropores (d_{pore} < 2 nm) and ultramicropores (d_{pore} 0.3 ÷ 0.7 nm) [98–100]. The internal structure of CMS adsorbent and general pore size distribution are presented in Fig. 4.1-1. The ultramicropores are mainly responsible for molecular sieving while the micropores provide negligible resistance to diffusion, but provide high capacity sorption sites for gas molecules [101].

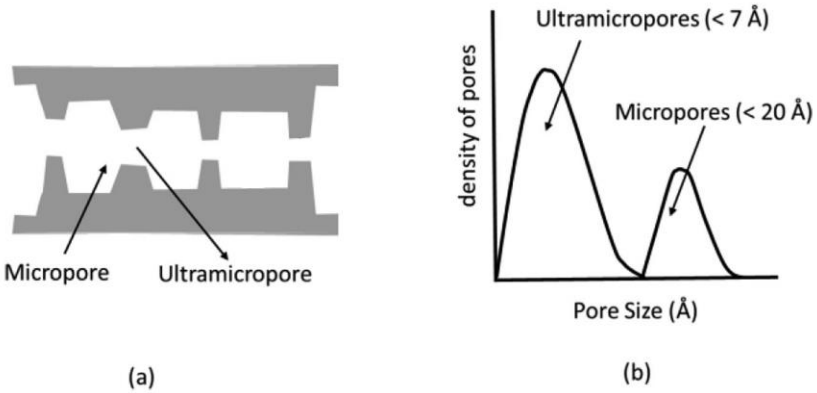

Fig. 4.1-1 (a) internal structure of CMS; (b) general pore size distribution of CMS [99]

In this work, Shirasagi MSC CT-350, taken from the lot M12OE1 and provided by CarboTech AC GmbH, is exploited. Standard specifications of the material are given in Tab. 4.1-1. A picture of the utilised adsorbent is shown in Fig. 4.1-2.

Tab. 4.1-1 Specifications of Shirasagi MSC CT-350 [102,103]

Parameter	Specification
Raw material	Coconut shells
CAS number	7440-44-0
Appearance	Cylindrical
Colour	Black
Particle diameter [mm]	1.8 ± 0.2
Real density [g/mL]	2.0 ÷ 2.2
Bulk density [g/mL]	0.68 ÷ 0.73
Ignition point [°C]	400

Fig. 4.1-2 Adsorbent Shirasagi MSC CT-350

4.2 PSA pilot-plant

The experimental data are obtained during the operation of a 2 × 2 L twin-bed PSA pilot-plant placed in a temperature adjustable climate chamber (-5 °C ÷ +100 °C, Binder). The unit is fed with dry compressed air. To control the product purity level, the product stream flow rate is adjusted. This control strategy represents the common operation of commercial plants. Properties of adsorber columns are displayed in Tab. 4.2-1.

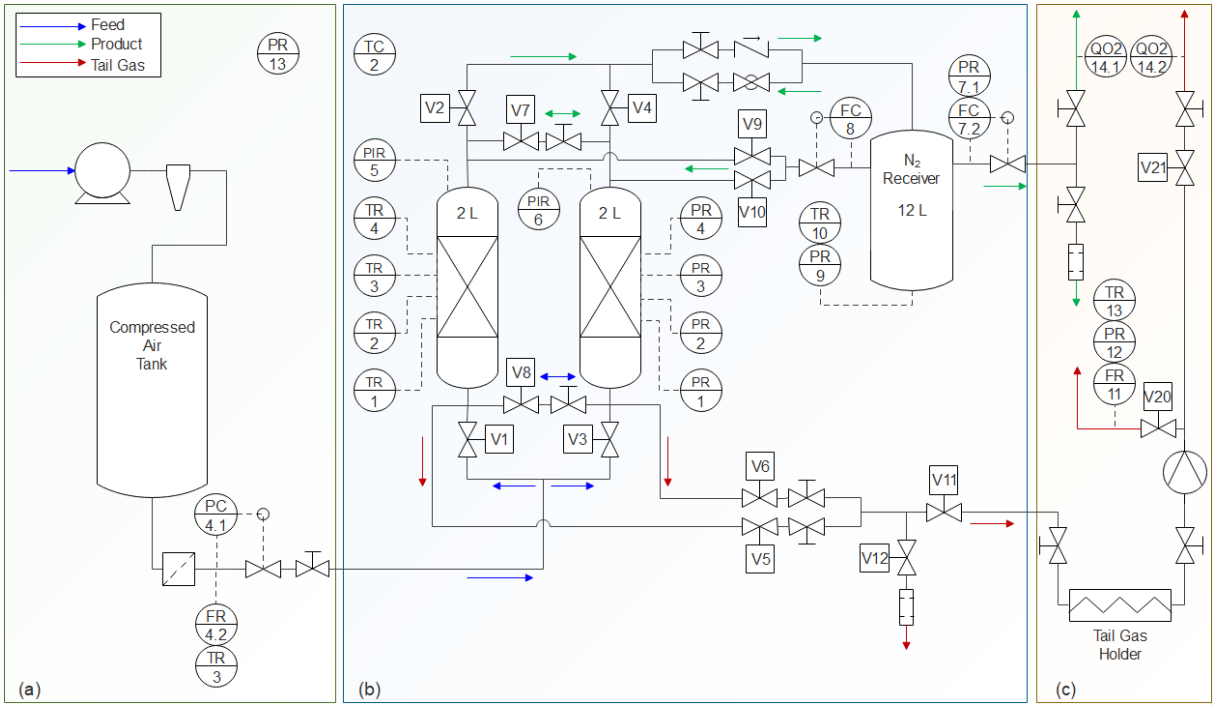

Fig. 4.2-1 Scheme of the PSA experimental set-up

A scheme of the PSA test unit is shown in Fig. 4.2-1. Three main sections can be recognised: the feed gas preparation and pre-treatment section (a), the twin-bed PSA plant section (b), and the product and tail gas analytics section (c). Devices are connected with a 6 mm internal diameter PA12 polyamide piping resistant to oxygen diffusion.

Tab. 4.2-1 Adsorber column properties

Parameter	Left Adsorber	Right Adsorber
Column length [mm]	594 ± 1	594 ± 1
Column external diameter [mm]	70 ± 1	70 ± 1
Column internal diameter [mm]	66 ± 1	66 ± 1
Packed bed length [mm]	582 ± 1	580 ± 1
Packed bed volume [l]	1.990 ± 0.006	1.983 ± 0.006
Mass of adsorbent [g]	1416.89 ± 0.01	1408.42 ± 0.01
Filling bulk density [g/l]	712.005 ± 2.158	710.247 ± 2.161

The feed gas in section (a) supplies ambient air compressed up to 11 bar abs by a compressor (KAESER Airtower 3), which is equipped with a refrigeration dryer and a hydrocyclone for moisture removal. The feed streamline further consists of a 500 L compressed air tank, followed by a 0.01 µm sieve filter and an activated carbon filter (Omega Air) for a subsequent exclusion of solid particles and oil vapours. The pressure is controlled by a Norgren manual pressure regulator (PC 4). The feed flow rate is measured by a thermal mass flow meter (FM 4) from Bronkhorst, type F-112AC.

The air distribution system of the two adsorbers in section (b) contains a stainless steel perforated plate and a layer of a metal wire mesh placed at the bottom of the bed. The two stainless steel adsorber columns (A1 and A2) are packed with Shirasagi MSC CT-350 by the snowstorm filling method. A coconut fiber mat is placed at the top of the adsorbent bed to fix the packed bed even under strong pressure fluctuations.

Four thermocouples type K (TIR 1-4) from TMH and four pressure transmitters (PIR 1-4) from Aplisens, type PCE-28.SMART, are placed at equal intervals along the wall of columns in order to measure temperature and pressure distributions inside the packed bed. Additionally, the closing flange of both adsorbers is equipped with a pressure transmitter (PIR 5, PIR 6) to track the pressure variation at the top of the packed bed. The product receiver vessel is installed together with temperature (TIR 10) and pressure (PIR 9) sensors. Moreover, temperature indicators (Aplisens CTX) are placed in the feed pipeline (TIR 3), as well as inside of the climate chamber (TIR 2) for an operating temperature control. Thermal mass flow controllers (Bronkhorst F-201AV and F-201CV) are installed for the regulation of the flow rates of product (FC 7) and purge* (FC 8) streams. Two output streams – the product gas and the tail gas – are analysed in order to measure their oxygen concentration. Oxygen analysers (Michell XZR400A4 and Servomex MultiExact 5400) are adapted for the measurement of trace amounts in the product gas (ppm range) by a zirconium dioxide sensor (QO2 14.1) and of the tail gas concentration by a high-precision paramagnetic sensor (QO2 14.2). A drum-type gas meter (FM 11) determines the flow rate of the tail gas (Ritter TG1/5). Due to the non-continuous flow of the tail gas stream during the PSA process cycle, the tail gas is periodically collected in a rubber holder whenever the determination of the oxygen concentration and the flow rate are required. The test unit is equipped with externally piloted bi-directional pneumatic solenoid valves (V1-14) from Festo MF series, allowing the leak-tight operation in both flow directions. The system is fully automated by a PLC system (Beckhoff Automation), coded in TwinCAT 3™ software.

* supplying the purge from the N_2-receiver allows a precise control of purge flow rate and purge time slots; in practice, however, a simpler realisation is preferred

Pictures of the feed gas preparation and pre-treatment section, the twin-bed PSA plant section, and the product and tail gas analytics section are shown in Fig. 4.2-2.

Fig. 4.2-2 (top left) the feed gas preparation and pre-treatment section; (top right) the twin-bed PSA plant section; (bottom) the product and tail gas analytics section

4.3 Cycle organisation

In this work, the PSA cycle consists of the following steps: (1) co- and counter-current bed pressure equalisation; (2) co-current pressurisation by feed, with (3) counter-current backflow of product; (4) production; (1) co- and counter-current bed pressure equalisation; (5) counter-current blow-down; (6) counter-current purge by product gas; and optionally (7) the cutting step implemented as an interruption of blow-down and purge steps, respectively. The scheme of the seven-step cycle design is presented in Tab. 4.3-1.

Particular steps are implemented into the PSA cycle due to the following main objectives:

a) equalisation step: reduction of the compressed air consumption by utilisation of gas from the high-pressure column for pre-pressurisation of the low-pressure column before the following production step;
b) back-flow step: reduction of the axial dispersion thus inhibition of premature adsorber breakthrough during pressurisation step, as well as the acceleration of achieving the operating pressure level in the system;
c) purge step: acceleration of the packed bed regeneration during the blow-down step through the drain of oxygen-enriched gas from interparticle voids with product gas;
d) cutting step: reduction of product gas losses due to over-sufficient purge.

The scheme indicates a high level of process intensification. Various cycle steps run simultaneously which allows high performance figures, particularly at short cycle times, that will be shown later in the experimental results.

Tab. 4.3-1 Scheme of PSA cycle design

Step	PSA cycle		Description
	PSA half-cycle	PSA half-cycle	
1			Equalisation
2			Pressurisation
3			Back-flow
4			Production
1			Equalisation
5			Blow-down
6			Purge
7			Cutting

In order to enable data comparisons and to establish the baseline conditions for further process intensification strategies, the reference process is proposed. The cycle features of the reference process as well as its operating conditions are displayed in Tab. 4.3-2. The cutting step is not considered for the reference process since the optimal placement of this step depends on the CMS properties and cannot be fixed independently from the selected CMS-type or even CMS-lot. The flow rate of the purge stream is adjusted in the PSA system according to Eq. 4.3-1.

$$Q_{purge} = \frac{X \cdot V_{adsorber}}{t_{purge}} \qquad \text{(Eq. 4.3-1)}$$

where: Q_{purge} is the flow rate of the purge stream [m^3_n/h], $V_{adsorber}$ is the volume of the packed-bed [m^3], t_{purge} is time of the purge step [h], and X is a proportionality factor [-]. The magnitude of the proportionality factor X can be associated with the packed-bed porosity as it exhibits the adsorber volume fraction occupied by oxygen-enriched desorption gas, which should be replaced by nitrogen-enriched product gas.

Tab. 4.3-2 Cycle design and operating conditions of the reference process

Operating pressure [bar abs]	8
Operating temperature [°C]	20
Half-cycle time [s]	60
Production time / Blow-down time [s]	59 / 59
Equalisation time [s]	1
Equalisation strategy	Top/Top + Bottom/Bottom
Purge time [s]	59
Purge proportionality factor X [%]	40
Purge flow rate [m^3_n/h]	0.0485
Backflow	Yes
Cutting time [s]	0

Additionally, the operation scheme of particular valves in the pilot-plant during performing the reference process is presented in Fig. 4.3-1.

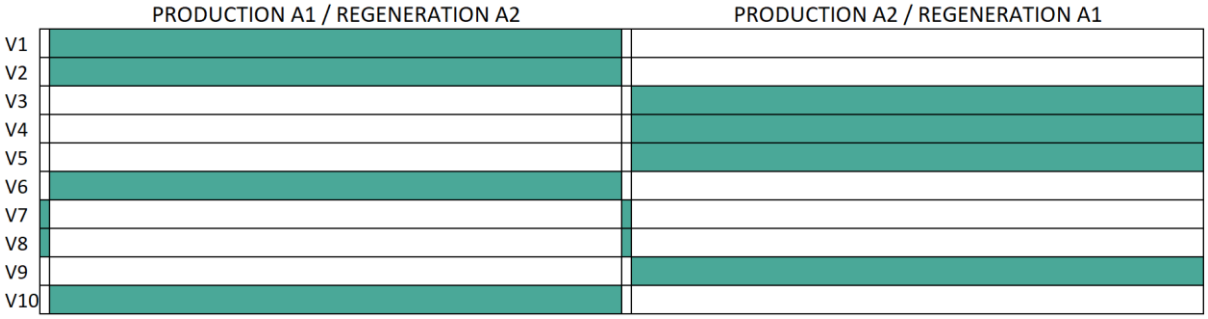

Fig. 4.3-1 Valves operation scheme in the reference cycle

4.4 Performance indicators

Multiple process variables and cycle organisation strategies give an opportunity for customising the system to individual requirements, which is the great advantage of the PSA technology. In the interest of creating a common concept of straightforward assessment and comparison of the PSA unit efficiency, so-called performance indicators (PIs) are introduced to evaluate the influence of process variables and cycle design.

The main goal of PIs is to provide condensed information, which are necessary for the plant design, such as production yield, adsorber sizing, and energy requirement. Tab. 4.4-1 [104] itemises PIs for the N_2-PSA – operated with a constant product flow rate – as the purity, the productivity, the recovery, and the air demand. In commercial applications, productivity values are listed for a certain purity class separately. Recovery and air demand can be used interchangeably since they are dependent variables, carrying both the same information content. In case of the N_2-PSA technology, the air demand has been proved as the more appropriate parameter.

In the N_2-PSA technology it is accepted that the product purity comprises the content of both nitrogen and argon since many industrial applications do not require an additional separation of inert gas mixtures. Consequently, in this work, the determination of the product purity is performed by assuming a binary gas mixture, where simply the difference to the oxygen concentration results in the nitrogen purity.

PSA performance indicators according to Tab. 4.4-1 can be obtained through two fundamental strategies: explicitly by the evaluation of the process streams throughputs, and implicitly by solving macroscopic material balances. In the first strategy, the productivity can be evaluated directly based on reading of the flow meter in the product pipeline, whereas the air demand bases on the readings of the flow meters in the feed and the product pipelines. Explicit PIs determination is a very simple and low-cost method; however, its biggest disadvantage is a lack of comparison data to confirm the correctness of the measurement. Therefore, the implicit method of the determination of performance indicators by solving macroscopic material balances is proposed as an important additional strategy for data verification. For this reason, two equations, the general (Eq. 4.4-1, GMB) and the component (here oxygen) (Eq. 4.4-2, OMB) material balances, are introduced in order to achieve the same performance information from two further independent solutions.

Tab. 4.4-1 Performance indicators of the N_2-PSA process [104]

	General definition	**At specific product purity class**
Purity	$\frac{c_i^{product}}{\sum_{i=1}^{N} c_i^{product}}$	$y^{product} = const$
Productivity	$\frac{c_i^{product} Q_i^{product}}{V_{CMS}}$	$\frac{Q^{product}}{V_{CMS}}$
Recovery	$\frac{c_i^{product} Q_i^{product}}{\int_0^t c_i^{feed} Q_i^{feed} dt}$	$\frac{y^{product} Q^{product}}{\int_0^t y^{feed} Q^{feed} dt}$
Air demand	$\frac{\int_0^t Q^{feed} dt}{Q_i^{product}}$	$\frac{\int_0^t Q^{feed} dt}{Q^{product}}$

$$Q_{feed}\rho_{feed} = Q_{product}\rho_{product} + Q_{tail-gas}\rho_{tail-gas} \quad \text{(Eq. 4.4-1)}$$

$$Q_{feed}\rho_{feed}x_{O_2\,feed} = Q_{product}\rho_{product}x_{O_2\,product} + Q_{tail-gas}\rho_{tail-gas}x_{O_2 tail-gas} \quad \text{(Eq. 4.4-2)}$$

Subsequently, equations for the calculation of performance indicators – the productivity (Eq. 4.4-3–4.4-4) and the air demand (Eq. 4.4-5–4.4-6) – are derived.

$$\frac{Q_{product}}{V_{CMS}} = \frac{1}{V_{CMS}\rho_{product}}\left(Q_{feed}\rho_{feed} - Q_{tail-gas}\rho_{tail-gas}\right) \quad \text{(Eq. 4.4-3)}$$

$$\frac{Q_{product}}{V_{CMS}} = \frac{1}{V_{CMS}\rho_{product}x_{O_2\,product}}\left(Q_{feed}\rho_{feed}x_{O_2\,feed} - Q_{tail-gas}\rho_{tail-gas}x_{O_2 tail-gas}\right) \quad \text{(Eq. 4.4-4)}$$

$$\frac{Q_{feed}}{Q_{product}} = \frac{\rho_{product}}{\rho_{feed}} + \frac{Q_{tail-gas}\rho_{tail-gas}}{Q_{product}\rho_{feed}} \quad \text{(Eq. 4.4-5)}$$

$$\frac{Q_{feed}}{Q_{product}} = \frac{\rho_{product}x_{O_2\,product}}{\rho_{feed}x_{O_2\,feed}} + \frac{Q_{tail-gas}\rho_{tail-gas}x_{O_2 tail-gas}}{Q_{product}\rho_{feed}x_{O_2\,feed}} \quad \text{(Eq. 4.4-6)}$$

A perfectly determined performance indicator attains exactly the same value whether calculated from the two material balances (according to the implicit method) or directly read from the flow meters (according to the explicit method). In fact, it is necessary to accept a certain tolerance of incompatibilities between values due to inevitable measuring errors. Any significant differences in values of performance indicators are the evidence of a faulty operation of the PSA system, e.g. leakages, incorrect calibration of measuring devices, errors in transmitting electrical signals to the equipment, errors in the software code, accumulation of pollutants in valves, diffusion intake due to porous or inadequate piping or seals, or exhausted filters.

In this work, a performance indicator value is considered to be determined correctly when the difference between the results obtained from the different established calculation paths does not exceed a tolerance level of 1 %, determined as a relative error δ_{exp}. If δ_{exp} between differently calculated performance indicators is lower than 1 %, obtained values are considered as correct. If δ_{exp} is larger than 1 %, obtained values are discarded. Admittedly, this 1 %-tolerance level of δ_{exp} seems to be set arbitrarily, however justified by laboratory experience gained in decades of quality control. Additionally, separate performance indicators of each single adsorber can also be calculated, which allows the disclosure of potential imbalances of operation between two packed beds.

Maintaining such a strict tolerance becomes more challenging the higher the product purity is addressed. Here the accuracy of measuring devices comes to the fore since a limited measurement precision mathematically prohibits solving equations with an arbitrary low tolerance.

4.5 Measurement accuracy

In order to solve the balance equations (Eq. 4.4-1 and 4.4-2), precise data of the feed, the product, and the tail gas flow rates are required. However, only one of three flows is constant in a PSA system and the others fluctuate along the cycle. In this study, the product flow rate is set constant. Thus, the measurement of feed and tail gas flow rates during the rapid system pressurisation/depressurisation could be burdened by a comparably high experimental error mainly due to the limitation in scan-speed of the measuring devices as presented in Fig. 4.5-1.

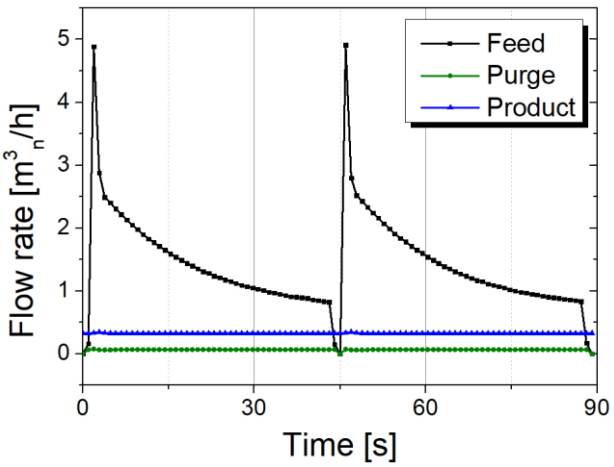

Fig. 4.5-1 Flow rate of process streams during the PSA cycle

The mean value of the fluctuating feed flow rate shown in Fig. 4.5-1 is calculated as an integral over the time. The assembled feed flow meter reveals 0.5 s of response time with a measurement accuracy of ± 0.6 %. Anyhow, the integrated value of the feed mass flow rate is always lower than the sum of product and equalised tail gas mass flow rates. In particular, the first seconds of the PSA half-cycle are not tracked fast enough by conventional flow meters. Consequently, the air demand determined by the explicit method is always slightly lower than determined by the implicit method, as shown in Tab. 4.5-1. Thus, it comes as no surprise that the relative error between explicit and implicit methods of the air demand determination does exceed the implemented 1 %-tolerance level.

Tab. 4.5-1 Air demand of the reference process calculated according to different strategies

	Explicit method	**Implicit method**		**Relative error δ_{exp}**	
		GMB	OMB	Explicit/ Implicit	Implicit/ Implicit
Air demand [m^3_n/h air / m^3_n/h N_2]	3.09 ± 0.03	3.17 ± 0.01	3.18 ± 0.01	2.75 %	0.32 %

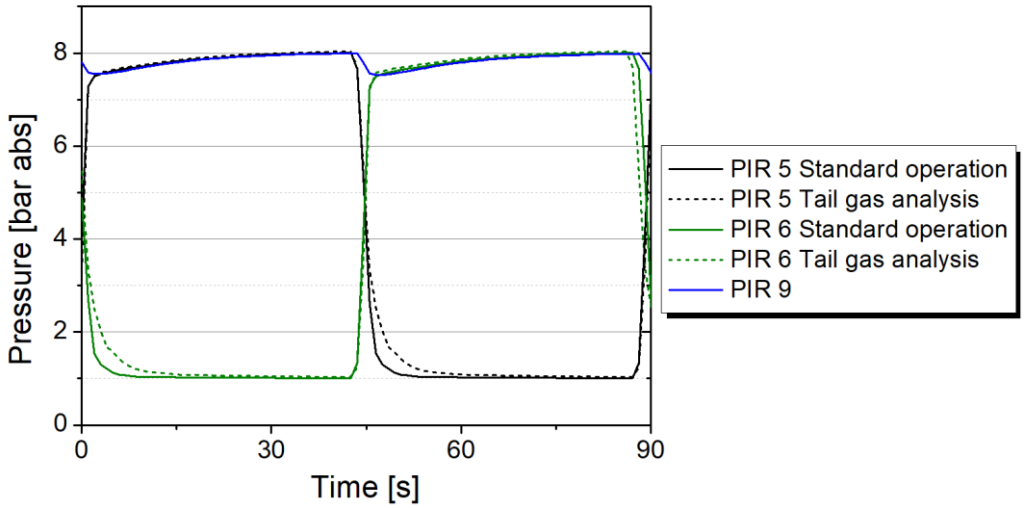

Fig. 4.5-2 Pressure in adsorbers during the PSA cycle

To reduce the experimental error, the fluctuating tail gas is collected in a gas holder to be equalised over the time and then analysed on quantity and composition parallel to the continuing

operation of the PSA test rig. Therefore, this particular data can be determined under steady-state conditions. Construction and commissioning of such devices require higher investment costs and longer start-up times due to the large number of signals integrated in the software code. Despite that, the strategy ensures high accuracy of obtained performance indicators, which is shown in Tab. 4.5-1. The relative error between implicit methods of determination of the air demand does not exceed the implemented 1 %-tolerance level. For this reason, methods that require the direct measurement of the feed stream flow rate are not applied for the determination of performance indicators in this work. Consequently, the productivity values are established only through the explicit method, and the air demand values are established only through the implicit method.

However, the measurement of the tail gas flow rate is also burdened with challenges. Since the tail gas is captured by the holder vessel, the generation of additional flow resistances occur due to the fact that the gas is not directly discharged into the environment. The comparison of adsorber pressure profiles during the standard operation and the tail gas analysis is presented in Fig. 4.5-2. The magnitude of the driving force for the desorption process is affected and the bed is not fully regenerated during the cycle with implemented tail gas analysis. As a result, cyclic-steady-state (CSS) conditions are disturbed and the product purity decreases slightly until the system returns to the standard operation. Therefore, continuous tracking of air demand is not recommended since a product of lower purity is generated.

All experimental parameters required for PIs determination are listed in Tab. 4.5-2 along with their measurement accuracies provided by the manufacturers of the equipment. The measurement accuracy of the packed bed volume is presumed, corresponding to the precision of the used calliper. The PSA experiment according to the reference process (as presented in Chapter 4.3) was performed ten times in order to determine the reproducibility error of the experimental set-up. Results are shown in Tab. 4.5-3. The reproducibility error is much lower than 1 % in the case of the air demand determined through the implicit method.

Tab. 4.5-2 Experimental parameters for solving mass balances of the PSA system

Parameter	**Measurement accuracy [%]**
Oxygen concentration in the product [ppm O_2]	0.1
Oxygen concentration in the tail gas [vol.-% O_2]	0.01
Flow rate of the product [m^3_n/h]	0.5
Flow rate of the tail gas [L/s]	0.2
Temperature of the tail-gas [°C]	0.08
Pressure of the tail-gas [bar]	0.3
Volume of the packed bed [m^3]	0.3

Moreover, a Monte-Carlo simulation on Eq. 4.4-5 and 4.4-6 was performed in order to investigate the influence of the combined measurement accuracy of all listed experimental values on the calculated air demand at different levels of product purity. The statistical analysis of probabilistic data obtained by a Monte Carlo simulation in the group of 1000 data points compared with experimentally obtained PI is presented in Tab. 4.5-4. As expected, the measurement uncertainty $\sigma_{\bar{X}}$ increases with the product purity which is an obvious consequence of narrowing the measuring range of the oxygen concentration in the product.

The normal distribution of collected probabilistic PIs around their mean values, together with experimentally found results (one data point marked with a red vertical line), are presented in

Fig. 4.5-3. The measured air demand is scattered around the Monte Carlo-simulated mean value – especially in the case of the 100 ppm data set, the experimentally found value is far from the peak of the normal distribution function. However, the deliberated data point cannot be considered as incorrect, but only as less likely to be measured.

Tab. 4.5-3 Results of the reproducibility test

	Productivity [m^3_n/h N_2 / m^3 CMS]	**Air demand [m^3_n/h air / m^3_n/h N_2]**		
	Explicit method	Implicit method		
		GMB	OMB	Relative error δ_{exp} [%]
1	58.16	4.95	4.97	0.40
2	58.17	4.93	4.94	0.20
3	58.15	4.96	4.98	0.40
4	58.16	4.93	4.94	0.20
5	58.17	4.96	4.97	0.20
6	58.15	4.94	4.94	0.00
7	58.16	4.97	4.99	0.40
8	58.16	4.94	4.97	0.61
9	58.17	4.93	4.92	0.20
10	58.16	4.94	4.97	0.61
$\bar{X}$	58.16	4.95	4.96	
σ	0.007	0.014	0.022	
$\sigma_{\bar{X}}$	0.01 %	0.29 %	0.45 %	

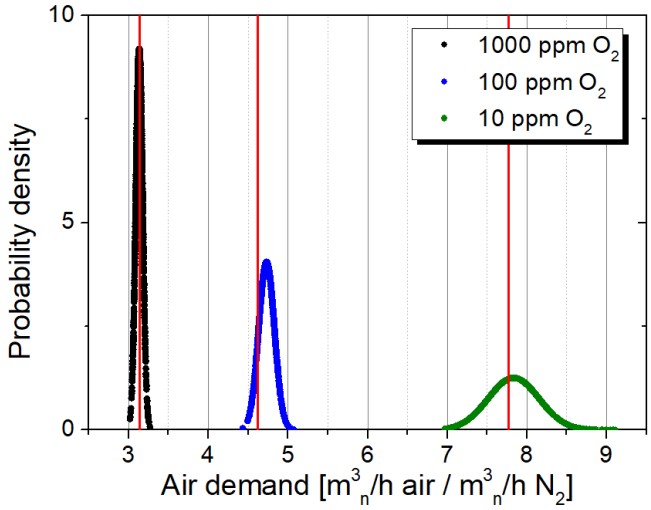

Fig. 4.5-3 Normal distribution of the air demand at different product purity levels

The distribution of the relative error δ_{sim} is presented in Fig. 4.5-4. The relative error δ_{sim} of the air demand is determined in every Monte Carlo run from the difference between Eq. 4.4-5 and 4.4-6. δ_{sim} surpasses δ_{exp} with a corresponding probability at every deliberated product purity level. This finding confirms that determination and comparison of differently calculated air demand values provide a very sensitive method to prove; and thus, to accept or to discard experimental high-purity data.

Tab. 4.5-4 Comparison of Monte-Carlo simulated PIs with experimental PI

Product purity [ppm O_2]	**1000**			**100**			**10**		
	Air demand [m^3_n/h air / m^3_n/h N_2]								
	$\bar{X}$	**σ**	$\sigma_{\bar{X}}$	$\bar{X}$	**σ**	$\sigma_{\bar{X}}$	$\bar{X}$	**σ**	$\sigma_{\bar{X}}$
Implicit (GMB)	3.17	0.04	1.13%	4.66	0.09	1.88%	7.83	0.30	3.82%
Implicit (OMB)	3.18	0.05	1.64%	4.81	0.11	2.38%	7.85	0.34	4.36%
Average	3.18	0.04	1.39%	4.73	0.10	2.13%	7.84	0.32	4.09%
Experimental result	3.18			4.62			7.78		

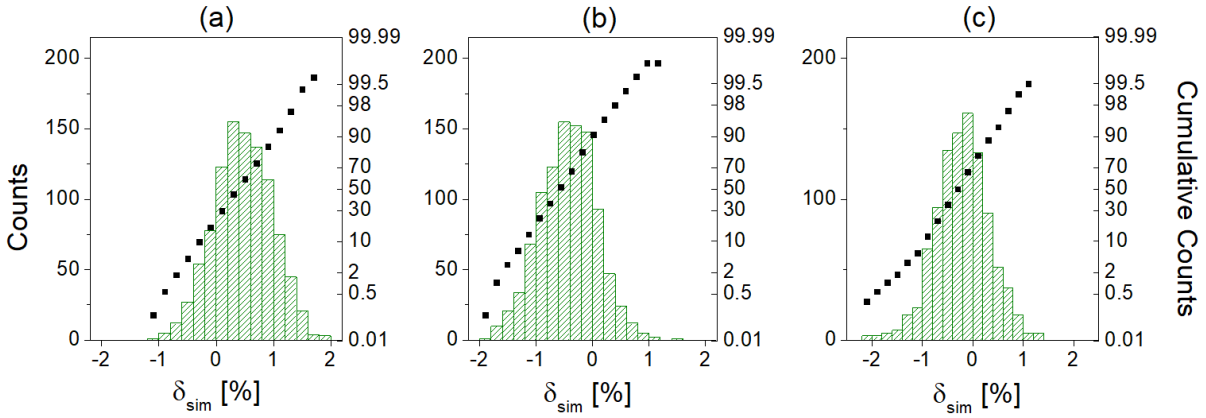

Fig. 4.5-4 Simulated distribution of the relative error δ_{sim} for the air demand at different product purity levels: (a) 1000 ppm O_2, (b) 100 ppm O_2, (c) 10 ppm O_2

The precision of determined performance indicators depends not only on the accuracy of the measuring equipment, but also on a number of experimental systematic and random errors, which must be recognised as well; although, they prove to be difficult to consider in statistical analysis. From experience, some of the most common errors are:

- inaccuracy in the determination of oxygen concentration in the product; the deviation between the measured and the required values progressively expand between calibration routines of the zirconia dioxide sensor;
- inaccuracy in the determination of the tail gas flow rate; the drum-type flow meter is filled with water, which evaporates at a higher rate during the summertime – so a regular recalibration is required; moreover, the inevitable build-up of biofilms disrupts the rotation of the drum; and
- insufficient homogenisation of the oxygen concentration in the tail gas; due to a non-continuous tail gas flow rate during a cycle and thus a non-uniform gas concentration caused by different oxygen levels during depressurisation, blow-down, and purge steps, a thorough gas mixing is required before sending the gas probe to the analyser.

Sensitivity studies show an increase in the standard deviation of the performance indicators, along with a decreasing measurement accuracy of utilised devices in every considered purity range. Therefore, minimising the measurement error by means of using precise equipment and performing a very accurate calibration allows the collection of results with a difference smaller than the assumed δ_{exp} at almost every considered purity level.

5 Validation of the mathematical model

Product purity, productivity, and air demand are the three main performance indicators used for the evaluation of the N_2-PSA effectiveness. When operating the adsorber, the product purity at the outlet of the system is the consequence of the gas flow rate through the column. This would suggest that a representation of process performance data should consider productivity as an independent variable, while the product purity, as well as the air demand, are dependent variables. This approach is consistent with the conventional demonstration of PSA performance results in the literature. However, in commercial applications, values for productivity and air demand are listed for a certain purity class separately, since the nitrogen quality, not quantity, indicates go/no-go decisions for a specific gas application.

In this work, experimental results of PSA performance indicators, i.e. productivity and air demand, are compared with the outcome of the mathematical model at fixed product purity levels, which is consistent with commercial conventions. The difference between simulated and empirical results is expressed as the relative error of the simulation Φ according to Eq. 5-1. Thus, the performance indicator value is underestimated by the mathematical model when Φ is positive; reversely, it is overestimated when Φ is negative.

$$\Phi = 100\% \cdot \left(\frac{PI_{EXP} - PI_{SIM}}{PI_{EXP}} \right) \qquad \text{(Eq. 5-1)}$$

Selected operating conditions, cycle organisation strategies, and plant design parameters are in agreement with the vast majority of relevant industrial applications. The effects presented here on PSA performance indicators are studied individually. Therefore, one parameter is investigated at a time, while all others follow the conditions of the reference process (as described in Chapter 4.3). The process performance data were collected upon reaching the cycle-steady-state (CSS); namely, when process variables do not fluctuate over subsequent PSA cycles. In order to assure cycle-steady-state conditions in the system, performance indicators are determined after at least ten hours of uninterrupted operation of the PSA unit.

5.1 Effect of operating conditions

5.1.1 Operating temperature

Since nitrogen generators are commonly exploited in both cold and warm environments, the influence of operating temperature on the PSA performance indicators is investigated in the range of 5 – 45 °C. Experimental and simulated results are presented in Tab. 5.1.1-1–2 and Fig. 5.1.1-1.

Independent from the purity level, Fig. 5.1.1-1 shows that productivity and air demand, simulated with the model premises listed in Chapter 3, fit well to experimental data in the temperature range between 12 °C and 36 °C.

At investigated conditions, the productivity reaches its maximum at 28 °C and 20 °C at a purity level of 1000 and 10 ppm O_2, respectively. The effect is evident when taking into consideration a competition of both adsorption thermodynamic and kinetic factors, which is especially relevant for kinetically-controlled separations. The equilibrium loading in the adsorbent is

elevated and the mass transfer rate is inhibited at the same time at low process temperatures. The opposite relationship is observed at high operating temperatures. Consequently, the maximum nitrogen productivity is detected at moderate ambient temperatures providing a trade-off between the equilibrium and kinetics factors. At the product purity of 1000 ppm O_2, the productivity is underestimated with the highest simulation error at 5 °C. It is most likely the consequence of the IAST prediction, which is comparably weak at low temperatures as presented in Fig. 3.3-3. However, at 10 ppm O_2, the highest relative error of the simulated productivity is detected at 45 °C, which indicates that probably inaccuracies of other effects superimposing the relative error.

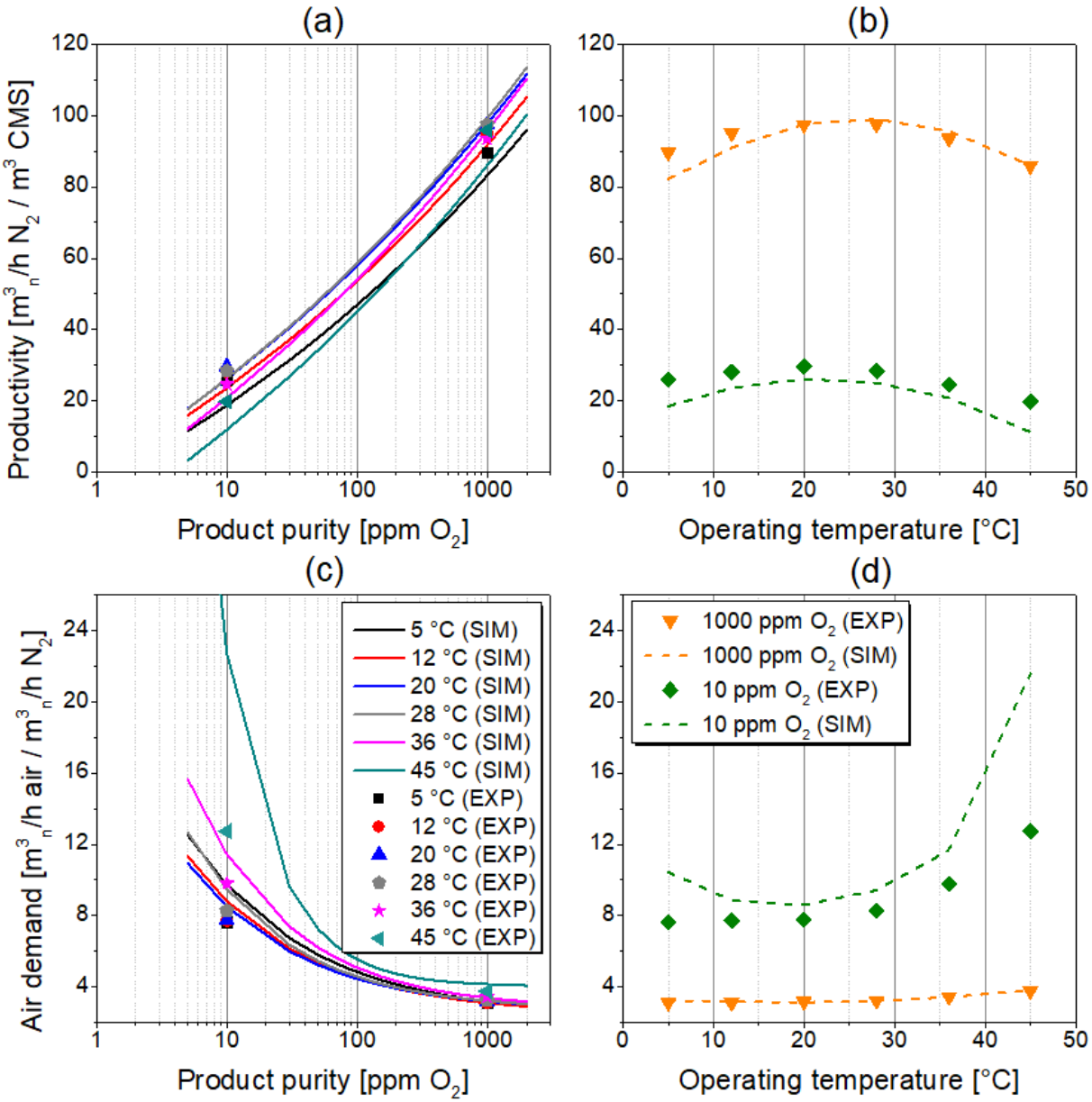

Fig. 5.1.1-1 PSA performance at different operating temperatures: (a, b) productivity; (c, d) air demand; (a, c) as a function of product purity; (b, d) as a function of operating temperature

The lowest air demand was measured at 5 °C and 12 °C, at purity levels of 10 and 1000 ppm O_2, respectively; however, the mathematical model predicts a minimum at about 20 °C regardless the product purity. It comes as no surprise since both of the determined performance indicators, productivity and air demand, are not independent from each other. They are a function of the required nitrogen purity, as well as of applied process conditions. Therefore, the

highest relative error of the simulated productivity results also in the highest relative error of the simulated air demand at the same measurement point.

Tab. 5.1.1-1 PSA performance at different operating temperatures at product purity of 1000 ppm O_2

Temperature [°C]	**Productivity [m^3_n/h N_2 / m^3 CMS]**			**Air demand [m^3_n/h air / m^3_n/h N_2]**		
	EXP	SIM	Φ [%]	EXP	SIM	Φ [%]
5	89.62	82.20	8.28	3.13	3.253	-3.93
12	95.00	91.00	4.21	3.12	3.164	-1.41
20	97.35	97.60	-0.26	3.18	3.147	1.04
28	97.42	99.00	-1.62	3.24	3.239	0.03
36	93.50	95.60	-2.25	3.45	3.428	0.64
45	85.87	86.01	-0.17	3.77	3.810	-1.06

Tab. 5.1.1-2 PSA performance at different operating temperatures at product purity of 10 ppm O_2

Temperature [°C]	**Productivity [m^3_n/h N_2 / m^3 CMS]**			**Air demand [m^3_n/h air / m^3_n/h N_2]**		
	EXP	SIM	Φ [%]	EXP	SIM	Φ [%]
5	26.06	18.50	29.01	7.65	10.435	-36.41
12	28.10	23.65	15.83	7.72	8.854	-14.69
20	29.64	26.14	11.79	7.78	8.601	-10.55
28	28.36	25.00	11.85	8.28	9.431	-13.90
36	24.60	20.78	15.52	9.78	11.681	-19.44
45	19.80	11.30	42.93	12.73	21.587	-69.58

5.1.2 Adsorption pressure

As the compression of air is a dominating factor of PSA operating costs, the adsorption pressure is mainly determined by economical constraints defined by the plant operator. Therefore, the influence of adsorption pressure on PSA performance indicators is investigated in the range of 6 – 10 bar abs. The results are presented in Tab. 5.1.2-1–2 and Fig. 5.1.2-1.

Tab. 5.1.2-1 PSA performance at different adsorption pressures at product purity of 1000 ppm O_2

Pressure [bar abs]	**Productivity [m^3_n/h N_2 / m^3 CMS]**			**Air demand [m^3_n/h air / m^3_n/h N_2]**		
	EXP	SIM	Φ [%]	EXP	SIM	Φ [%]
6	68.00	73.50	-8.09	3.27	3.217	1.62
7	82.65	86.35	-4.48	3.19	3.164	0.82
8	97.35	97.60	-0.26	3.18	3.147	1.04
9	109.69	107.00	2.45	3.1	3.160	-1.94
10	116.48	114.60	1.61	3.13	3.198	-2.17

Fig. 5.1.2-1 shows that the process simulation is capable to predict the influence of the operating pressure very well in the whole investigated pressure range.

Tab. 5.1.2-2 PSA performance at different adsorption pressures at product purity of 10 ppm O_2

Pressure [bar abs]	**Productivity [m^3_n/h N_2 / m^3 CMS]**			**Air demand [m^3_n/h air / m^3_n/h N_2]**		
	EXP	SIM	Φ [%]	EXP	SIM	Φ [%]
6	25.94	26.00	-0.23	6.70	6.967	-3.99
7	28.35	26.96	4.90	7.05	7.582	-7.55
8	29.64	26.14	11.79	7.78	8.601	-10.55
9	22.40	23.90	-6.70	10.45	10.149	2.88
10	19.79	20.50	-3.59	12.80	12.598	1.58

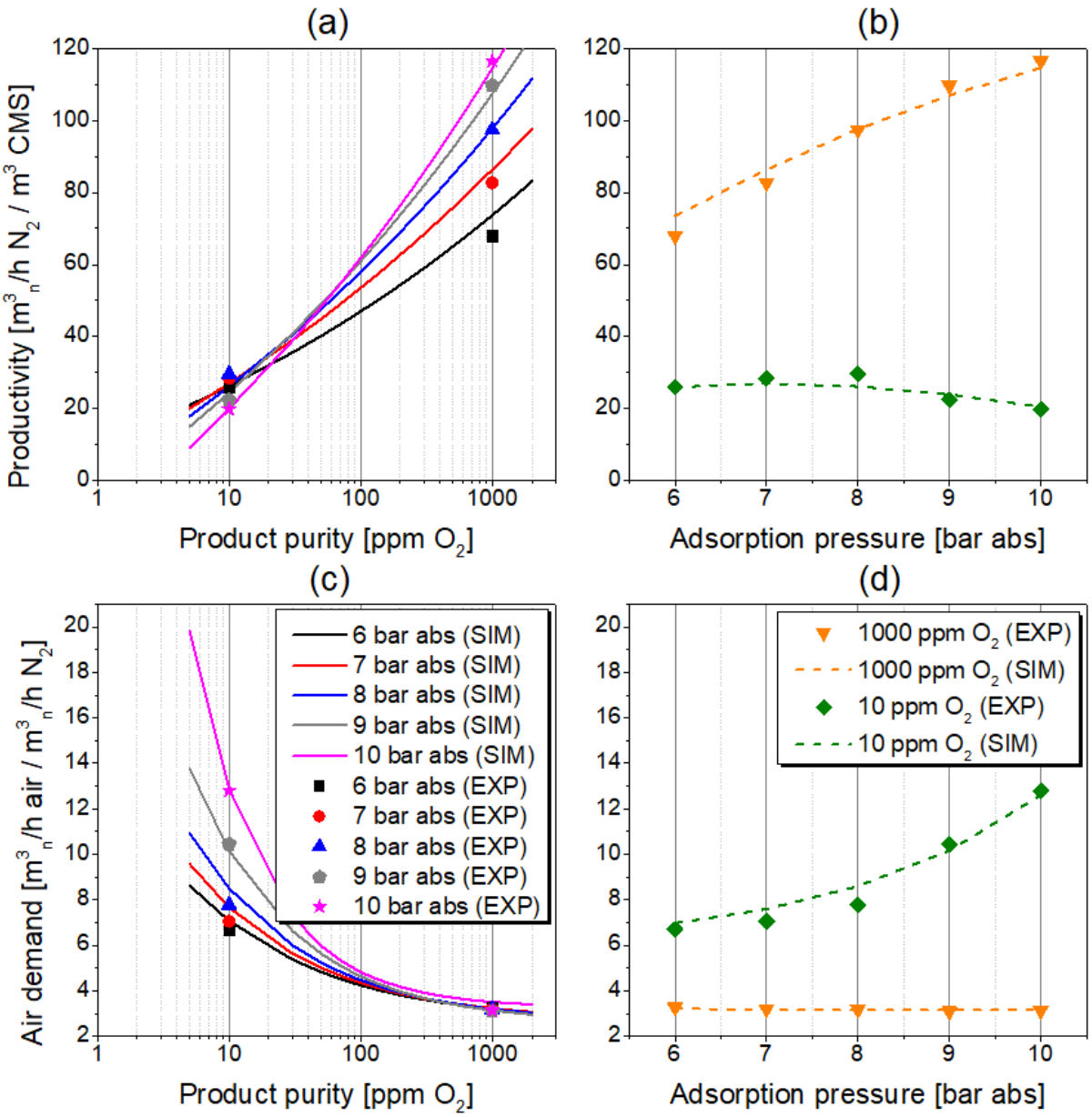

Fig. 5.1.2-1 PSA performance at different adsorption pressures: (a, b) productivity; (c, d) air demand; (a, c) as a function of product purity; (b, d) as a function of adsorption pressure

The experiments show that the effect of operating pressure on the PSA performance differs remarkably depending on the required product purity level. At 1000 ppm O_2, the nitrogen productivity exhibits a near linear increment with increasing adsorption pressure. This trend is evident since the driving force of mass transfer from bulk to the adsorbent is elevated, resulting in a raised oxygen loading in the CMS; thus, in a more efficient separation. Therefore, an effortless prediction of productivity results at different pressure levels is possible, which is very much appreciated in practice. However, such extrapolation of data would be possible exclusively in the range of pressure corresponding to the linear course of the oxygen isotherm. The air demand remains rather insensitive to the change of adsorption pressure.

The opposite effect is detected at 10 ppm O_2. The nitrogen productivity initially increases slightly with the adsorption pressure up to about 8 bar abs in order to decrease again posteriorly. This very distinct behaviour can be explained with respect to the conditions in the adsorber column. Since the product flow rate is reduced in order to generate nitrogen of higher purity standard, the MTZ in the column during adsorption is situated mainly at the bottom of the adsorber while the mass axial dispersion becomes less significant. Therefore, the top part of the packed bed is occupied almost exclusively by purified nitrogen. Moreover, as the superficial gas velocity along the column decreases, the contact time between gas and solid phases extends; hence, the system approaches the thermodynamic equilibrium state. As presented in Fig. 3.3-1, CMS adsorbs both nitrogen and oxygen; therefore, the overly excessive adsorption of the nitrogen occurs in the top part of the packed bed. Consequently, the flow rate of nitrogen, which leaves the system as a product stream, is reduced.

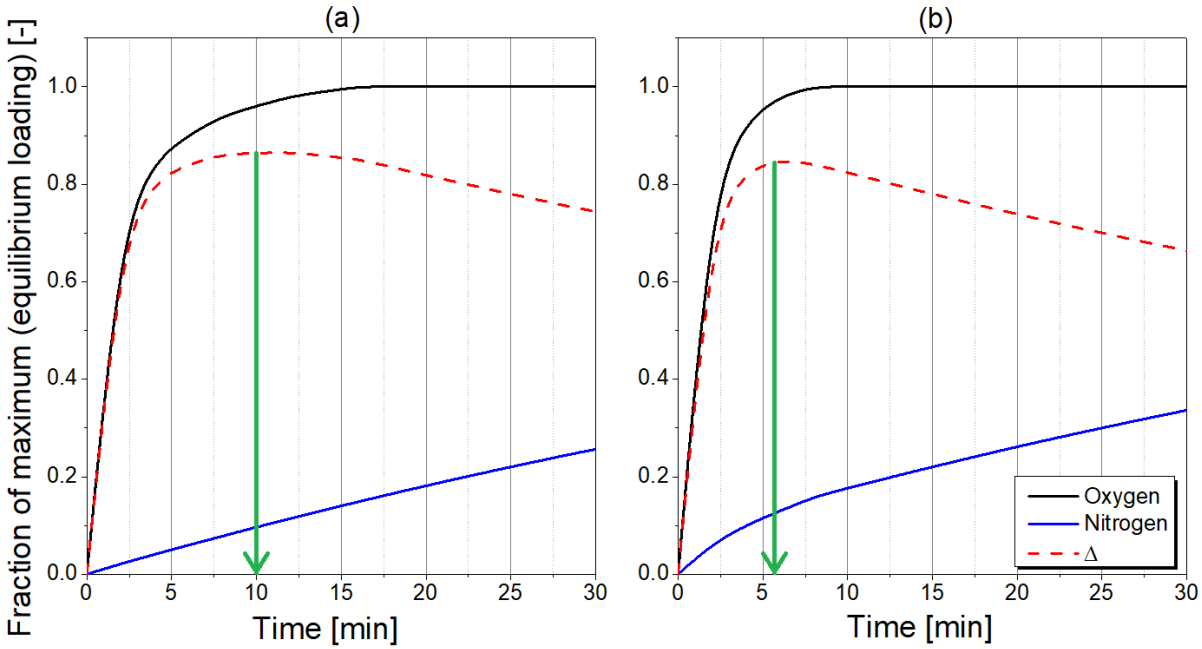

Fig. 5.1.2-2 Graphical representation of fractional uptake rates of oxygen and nitrogen together with their difference Δ: (a) at lower operating pressure/temperature, (b) at higher operating pressure/temperature; green arrow indicates the maximum selectivity [16]

As an interim conclusion it can be noted that the variation of productivity with the adsorption pressure is insignificant. Thus, it is recommended to operate a PSA plant equipped with Shirasagi MSC CT-350 at lower pressure levels due to a notably reduced air demand. In this way, high-purity nitrogen can be generated with lower operating costs.

The effectiveness of air separation with CMS depends on both equilibrium and kinetic factors; thus, the adsorption pressure should be adjusted to reinforce the effective oxygen adsorption, but to diminish the nitrogen adsorption at the same time. Furthermore, the proper estimation of the contact time of gas and solid phases is of essential importance in the case of kinetically controlled separations. Excessively prolonged duration of adsorption diminishes separation selectivity by approaching the thermodynamic equilibrium state. On the other hand, too short adsorption is not beneficial either, since diffusivity limitations occur. Therefore, the existence of an optimal contact time of phases is expected which greatly depends on applied process conditions, i.e. operating temperature and gas pressure.

Since the mass transfer coefficients of oxygen and nitrogen increase with their partial pressures, as presented in Eq. 3.5-6, the thermodynamic equilibrium state is approached faster in the system as the adsorption pressure increases. In the face of this situation, Fig. 5.1.2-2a plots the fractional uptake as a function of time for oxygen and nitrogen. The highest selectivity in the system is expected when the difference of fractional uptake rates attains the maximum. In the case of PSA operation, the contact time of phases is controlled indirectly by the adjustment of the product flow rate and therefore depends on the required product purity level. Furthermore, the occurrence of the peak selectivity at a specific contact time depends on system pressure as well as on temperature. As slopes of kinetic curves would be higher at elevated pressure and temperature due to faster sorption of gases, the selectivity peak shifts towards shorter contact times, as represented in Fig. 5.1.2-2b. Accordingly, when the high-purity nitrogen is generated, the productivity decreases because the system operates in conditions of prolonged contact time of phases, which is located on the right-hand side of the selectivity peak.

However, the presented effect of the PSA dynamic behaviour during the generation of a high-purity product will depend considerably on the CMS material and may not occur in every system due to different structure parameters and mass transfer conditions.

Referring to Fig. 3.3-3b, the relative error of simulated performance indicators should decrease at higher pressure levels. Although, at the investigated conditions, the trend of the simulation accuracy is not clearly visible, which probably suggests that inaccuracies of other effects are compensated within computed values of the relative error.

5.2 Effect of cycle organisation

5.2.1 Half-cycle time

The proper adjustment of the cycle time in a PSA process is the most relevant factor while aiming for a performance improvement. The shape of the mass transfer zone (MTZ) is sensitive to the adsorption duration at high product purities [44]. Thus, in PSA systems, additional effects of the mass axial dispersion and the pressure drop along the fixed-bed should be taken into consideration since the modification of a half-cycle time changes the time span proportion of pressurisation and production steps. The consequences of those effects e.g. premature column breakthrough or reduced working pressure are more pronounced as the half-cycle time is shortened. However, in industrial practice, brief cycle times are aimed for in order to increase the number of cycles per hour of PSA operation and thus boost-up nitrogen productivity. For that reason, the influence of the half-cycle time on PSA performance indicators is investigated in the range of 40 – 60 s. The results are presented in Tab. 5.2.1-1–2 and Fig. 5.2.1-1.

When the low-purity (1000 ppm O_2) product is generated the productivity increases as the half-cycle time is shortened. This finding confirms that the multiplication of the number of cycles per hour brings benefits for the process performance as the kinetic selectivity is exploited further. As such, the premature breakthrough of the adsorbent fixed-bed does not occur, even at relatively high gas superficial velocity causing extended oxygen MTZ. By the reduction of half-cycle time to 40 sec, productivity is increased by 11.5 %. Although, the opposite effect is found when the high-purity (10 ppm O_2) product is generated. In that case, the productivity decreases as the half-cycle time is shortened. It means that either the time provided for a mass transfer is insufficient and, thus, the diffusivity limit was encountered; or a premature column breakthrough occurs due to axial dispersion effects during the pressurisation step. Nevertheless, the observation could also be explained as a combination of both effects.

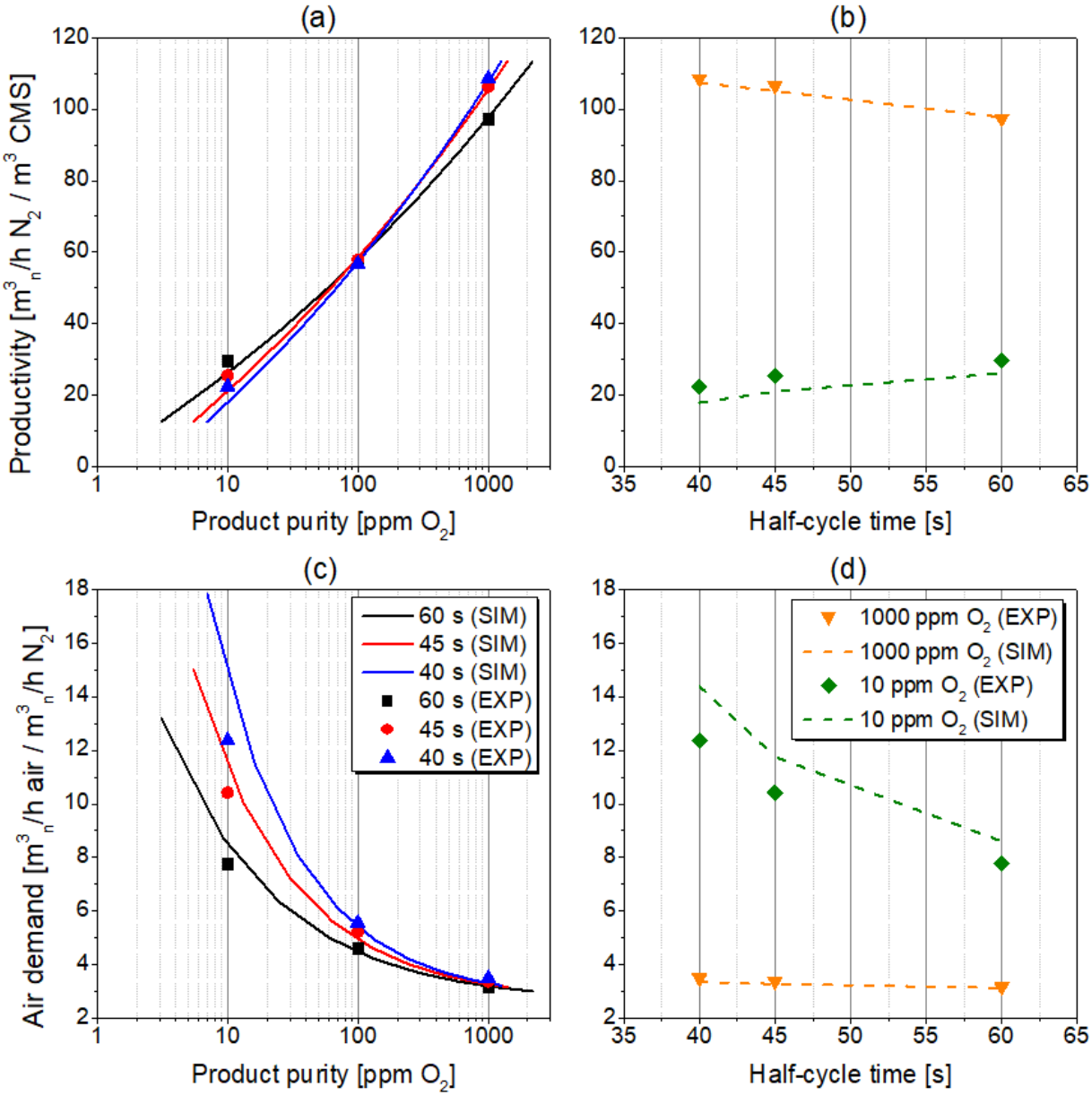

Fig. 5.2.1-1 PSA performance at different half-cycle times: (a, b) productivity; (c, d) air demand; (a, c) as a function of product purity; (b, d) as a function of half-cycle time

At every investigated process condition, the reduction of the half-cycle time results in an increased air demand due to the aforementioned change of time proportion for the different steps in the cycle. The adjustment of short half-cycle times makes the pressurisation step more

significant in relation to the production step. Since the specific volume of compressed air is required to achieve the operating pressure level, a smaller amount of compressed air is utilised for the production purpose at a short half-cycle time in comparison to a long half-cycle time. Consequently, at shortened half-cycle time the air demand is higher in order to maintain the targeted purity of the product.

Tab. 5.2.1-1 PSA performance at different half-cycle times at product purity of 1000 ppm O_2

Half-cycle time [s]	**Productivity [m^3_n/h N_2 / m^3 CMS]**			**Air demand [m^3_n/h air / m^3_n/h N_2]**		
	EXP	SIM	Φ [%]	EXP	SIM	Φ [%]
40	108.54	107.40	1.05	3.50	3.358	4.06
45	106.55	105.10	1.36	3.38	3.28	2.96
60	97.35	97.60	-0.26	3.18	3.147	1.04

Tab. 5.2.1-2 PSA performance at different half-cycle times at product purity of 10 ppm O_2

Half-cycle time [s]	**Productivity [m^3_n/h N_2 / m^3 CMS]**			**Air demand [m^3_n/h air / m^3_n/h N_2]**		
	EXP	SIM	Φ [%]	EXP	SIM	Φ [%]
40	22.38	17.87	20.15	12.37	14.395	-16.37
45	25.46	21.04	17.34	10.42	11.756	-12.82
60	29.64	26.14	11.79	7.78	8.601	-10.55

Tab. 5.2.1-1 shows that model predictions at investigated half-cycle times agree well with the experimental data at 1000 ppm; however, at 10 ppm, the relative error increases with decreasing half-cycle time, as stated in Tab. 5.2.1-2. As the half-cycle time is reduced, the consequences of a slightly imprecise estimation of the pressure curves during the initial phase of the PSA half-cycle are more pronounced. This is especially true within the first few seconds, as the interchange of gas in the system is very rapid. The precise quantitative representation of pressure in the adsorber column is, therefore, very challenging, as already discussed by means of Fig. 3.2-3. Moreover, any deviations from plug flow conditions are more pronounced at shortened PSA cycle times, especially while operating a pilot-scale system. For those reasons, the highest errors of the simulated performance indicators are found at the half-cycle time of 40 s.

5.2.2 Purge flow rate

The counter-current purge step is performed at atmospheric pressure level, simultaneously to the counter-current blow-down. During purge of the column, a specific amount of product gas accumulated in the N_2-receiver tank is reversed into the adsorber and evacuated from the system as part of the tail-gas. An implementation of this step into the PSA cycle supports the bed regeneration since the interparticle voids are filled with purified nitrogen gas; thereby the amount of oxygen in the column is reduced before the following production step. Consequently, the application of the purge stream affects the concentration profiles along the adsorber column during both adsorption and desorption. Accordingly, the influence of the purge proportionality

factor on the PSA performance indicators is investigated in the range of 30 – 60 %. The results are presented in Tab. 5.2.2-1–2 and Fig. 5.2.2-1.

An increased purge flow rate into the system ensures elevated nitrogen productivity values regardless of the investigated purity level. The efficiency of the desorption process is diminished as the operating temperature decreases. As such, an additional reinforcement in the form of the oxygen expulsion from the packed-bed void volume by the nitrogen purge stream is required in order to regenerate the adsorber bed properly. The effect is more pronounced at a low product purity level (1000 ppm O_2) than at a high product purity level (10 ppm O_2). This is due to the extended oxygen MTZ in the adsorber column caused by the high gas superficial velocity, which leads to intensified axial mass dispersion. Hence, the quantity of oxygen accumulated in the system during the adsorption is higher in the case of low-purity rather than high-purity nitrogen production. For that reason, at 1000 ppm O_2, more oxygen is desorbed during the blow-down and shall be purged to enable the adsorbent bed regeneration. Since the air demand remains rather insensitive to the change of the purge flow rate, it is recommended to operate the PSA unit with an increased purge stream flow rate wherever the process conditions are corresponding.

Tab. 5.2.2-1 PSA performance at different purge flow rates at product purity of 1000 ppm O_2

Purge proportionality factor [%]	**Purge flow rate [m^3_n/h]**	**Productivity [m^3_n/h N_2 / m^3 CMS]**			**Air demand [m^3_n/h air / m^3_n/h N_2]**		
		EXP	SIM	Φ [%]	EXP	SIM	Φ [%]
30	0.0364	94.35	94.81	-0.49	3.19	3.169	0.66
40	0.0485	97.3	97.60	-0.26	3.18	3.147	1.04
50	0.0606	98.7	100.19	-1.51	3.17	3.129	1.29
60	0.0727	100.4	102.95	-2.54	3.18	3.112	2.14

Tab. 5.2.2-2 PSA performance at different purge flow rates at product purity of 10 ppm O_2

Purge proportionality factor [%]	**Purge flow rate [m^3_n/h]**	**Productivity [m^3_n/h N_2 / m^3 CMS]**			**Air demand [m^3_n/h air / m^3_n/h N_2]**		
		EXP	SIM	Φ [%]	EXP	SIM	Φ [%]
30	0.0364	29.40	25.03	14.87	7.7	8.798	-14.26
40	0.0485	29.64	26.14	11.79	7.78	8.601	-10.55
50	0.0606	30.12	27.50	8.69	7.73	8.354	-8.07
60	0.0727	30.55	28.58	6.44	7.78	8.208	-5.50

Fig. 5.2.2-1 verifies that the model predicts the influence of the purge flow rate in a very precise matter. The trends are correctly identified; however, the model accuracy shows different tendencies at different purities.

At the lower product purity level of 1000 ppm O_2, the relative error of simulated PSA performance parameters increase with a rising purge flow rate. This outcome can be explained since the elevated purge flow rate results in a reinforcement of the non-uniform distribution of the counter-current gas flow through the column in the experimental set-up, particularly at the

top of the adsorber. Thus, the fixed bed regeneration in the existing PSA plant is not accomplished as efficiently as it is predicted by the process simulation, which does not fully account for those effects. The point is particularly valid when low-purity nitrogen is required, since the MTZ in the column during adsorption becomes extended due to the intensified mass axial dispersion at the elevated product flow rate; therefore, an efficient bed regeneration comes to the fore while aiming for PSA performance enhancement. Consequently, the PSA performance simulation is more accurate as the purge flow rate in the system decreases.

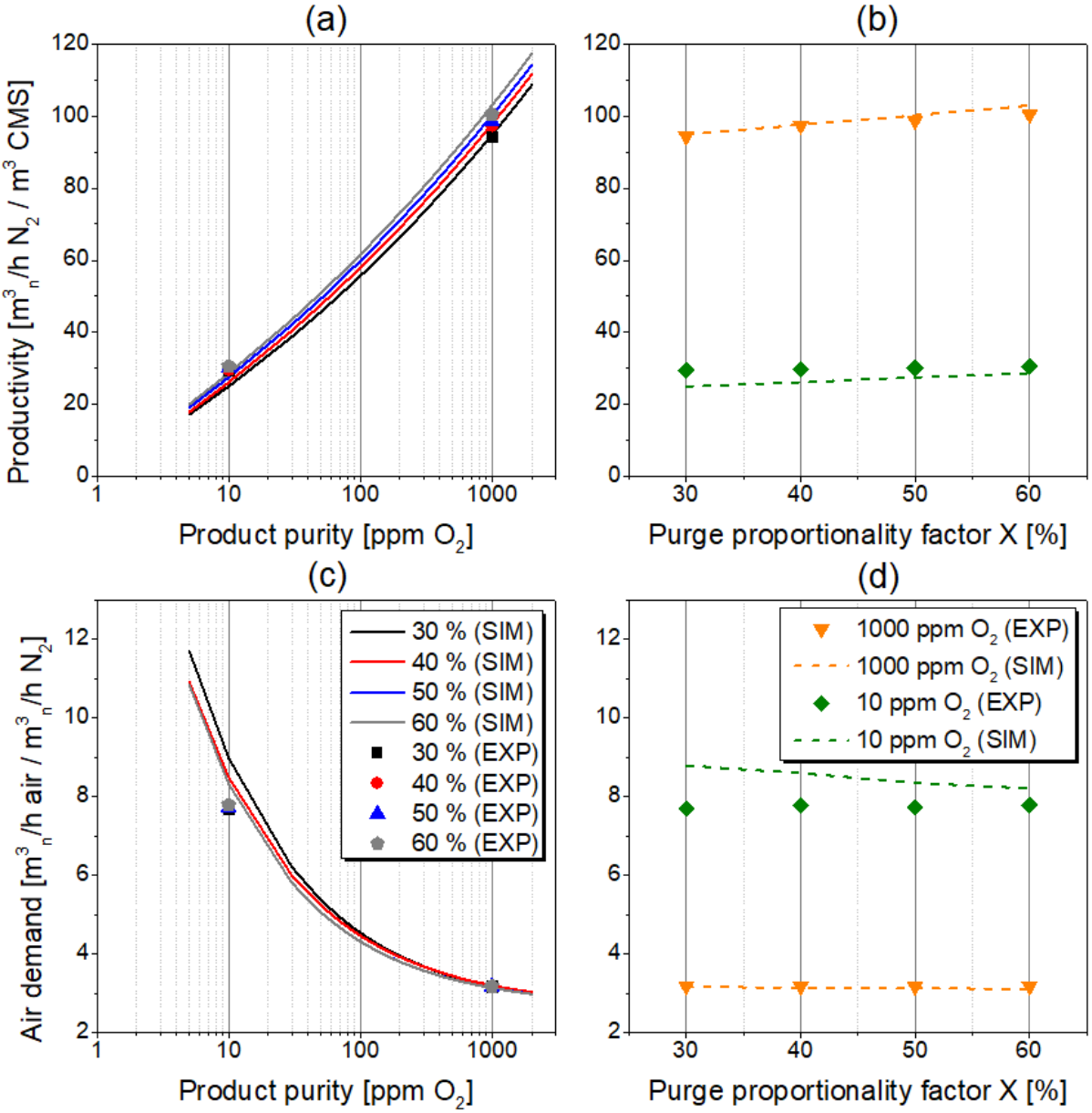

Fig. 5.2.2-1 PSA performance at different purge proportionality factor: (a, b) productivity; (c, d) air demand; (a, c) as a function of product purity; (b, d) as a function of purge proportionality factor

Oppositely, at a higher product purity level of 10 ppm O_2, the relative error of simulated PSA performance parameters decreases with increasing purge flow rate. While the generation of high-purity nitrogen is required, the product flow rate is lowered, so the MTZ in the column during the adsorption is situated mainly at the bottom of the adsorber. Therefore, an efficient adsorbent fixed bed regeneration is primarily required in the bottom section of the column. However, since the counter-current purge is provided at the top of the adsorber column, its velocity decreases progressively and reaches a minimum at the bottom due to a pressure drop

on the fixed bed. Consequently, as the purge flow rate is decreased in the process simulation, the minimum required gas velocity could perhaps not be achieved for the proper adsorbent regeneration since the mathematical model does not account for any grade of gas channelling, which is evident and inevitable in every experimental PSA set-up. Accordingly, the accuracy of performance prediction increases with a purge flow rate in the system.

5.2.3 Cutting time

The cutting step is a supplementary cycle design element implemented at the end of the PSA cycle terminating the blow-down and purge steps before finishing the adsorption step in the adjacent column. Cutting can be adapted in order to improve the PSA process performance of kinetic-based separation since the difference in the sorption rates of molecules in the feed gas mixture can be exploited. Whereas the duration of the blow-down step is reduced, the desorption of gases from the CMS adsorbent could still progress while the adsorber column is not opened to the ambient, as shown in Fig. 5.2.3-1. The effect is more pronounced for components with slow mass transfer kinetics due to insufficient time provided for its complete desorption from the adsorbent surface. Since in this work nitrogen is the component with slow kinetics, it is expected that losses of adsorbed nitrogen to the wasted tail-gas can be avoided. However, the effect is highly dependent on the utilised CMS-type. Besides, analogously to the previous case of changing the purge stream flow rate, the implementation of a cutting step also impacts the oxygen mass transfer zone along the adsorber during production and regeneration; thus, its adoption greatly depends on the process conditions. Hence, the influence of the cutting time on the PSA performance indicators is investigated in the range of 0 – 15 s. During experiments, the purge proportionality factor equals 40 %. The results are presented in Tab. 5.2.3-1–2 and Fig. 5.2.3-2.

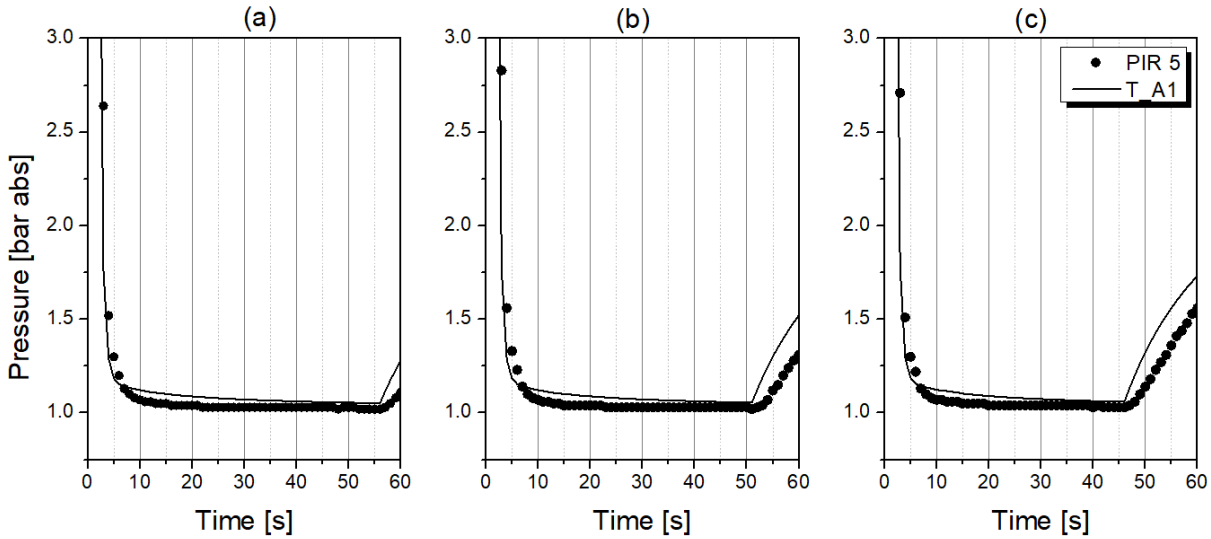

Fig. 5.2.3-1 Experimental and simulated pressure profiles during the blow-down step at product purity of 1000 ppm O_2 at different cutting times: (a) 5 s, (b) 10 s, (c) 15s

Tab. 5.2.3-1–2 show that the model predicts the influence of the cutting time on PIs very sufficiently regardless of the cutting time and purity level. This finding confirms that the implemented kinetic model represents the existing mass transfer conditions quite realistically; since any imprecision in the description of kinetics would overthrow the correctness of the mathematical model, particularly during the simulation of PIs as a function of this parameter.

At experimentally investigated conditions, the application of a cutting step is particularly advantageous for the generation of product at the higher purity level of 10 ppm O_2, since the air demand can be reduced whereas the productivity remains rather unaffected. It indicates that the oxygen desorption occurs in the initial phase of the blow-down and the purge steps, respectively, so the packed-bed with a narrow mass transfer zone is regenerated sufficiently. Moreover, the tail-gas becomes less diluted by nitrogen. It signifies that the desorption of nitrogen progresses during the cutting step, which ensures lower oxygen concentration in the adsorber at the beginning of the subsequent production. Furthermore, higher initial pressure in the system is obtained.

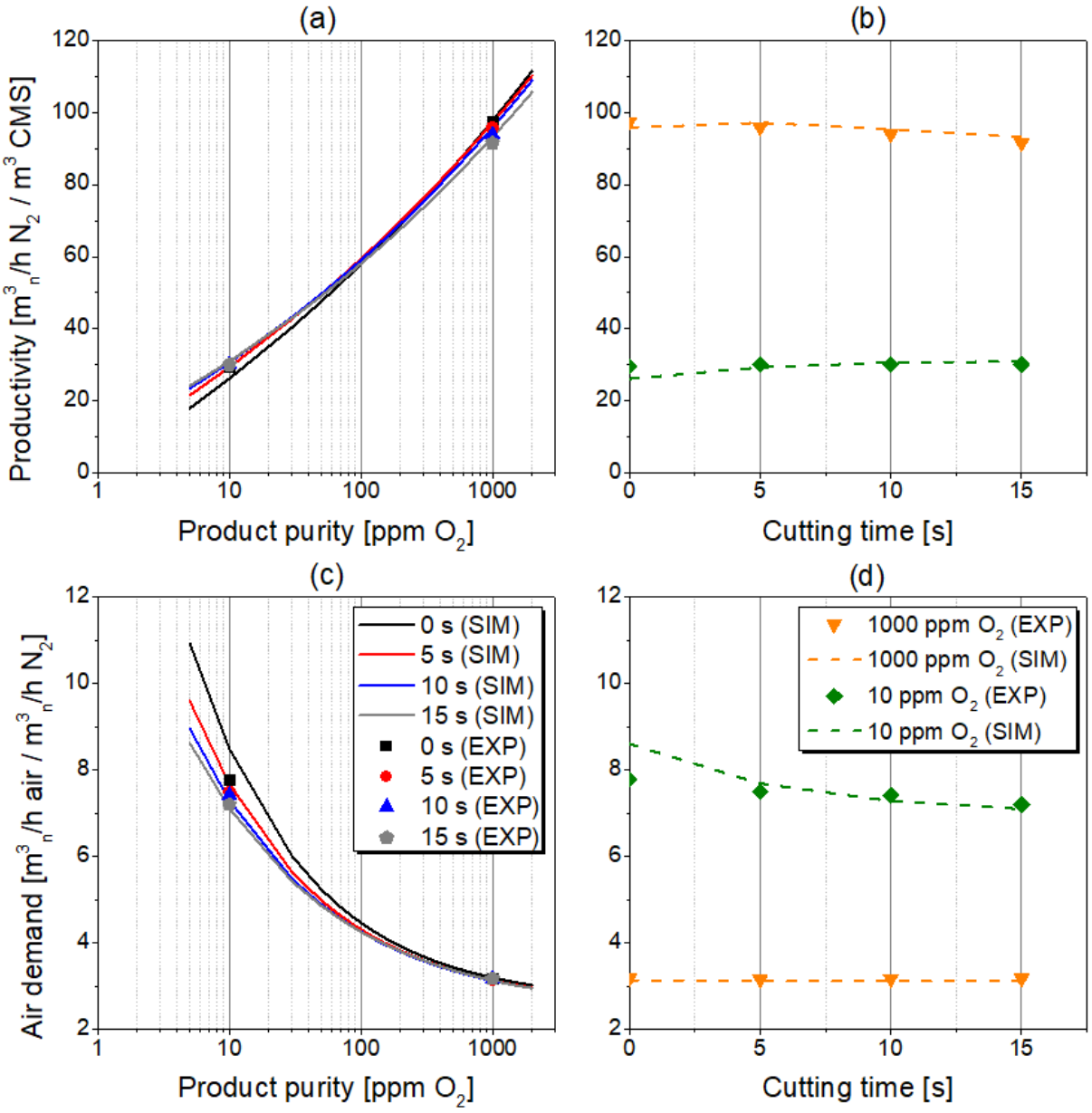

Fig. 5.2.3-2 PSA performance at different cutting time: (a, b) productivity; (c, d) air demand; (a, c) as a function of product purity; (b, d) as a function of cutting time

When nitrogen of a lower purity (1000 ppm O_2) is required, cutting should not be considered in the PSA cycle as a slight decline in productivity occurs. It indicates that an insufficient amount of time was provided for a desorption of oxygen, which forms a wide MTZ along the adsorber. Consequently, the packed-bed is not properly regenerated before the following production step, and the premature oxygen breakthrough occurs. Since the air demand remains

rather insensitive to the cutting time, it is recommended to operate the PSA unit without the adoption of cutting, while using Shirasagi MSC CT-350, wherever the process conditions are corresponding.

At the lower product purity level of 1000 ppm O_2, the relative error of the PSA simulation increases slightly with the cutting time; however, this effect is statistically insignificant. Surprisingly, the opposite and much more pronounced trend is detected at the higher product purity level of 10 ppm O_2. Since the precision of the calculated equilibrium loading at 20 °C increases with the system pressure, as shown in Fig. 3.3-3b, the elevated pressure at the end of the half-cycle could be a reason for an overall decrease in the relative error of the PSA simulation.

Tab. 5.2.3-1 PSA performance at different cutting times at product purity of 1000 ppm O_2

Cutting time [s]	**Purge time [s]**	**Purge flow rate [m^3_n/h]**	**Productivity [m^3_n/h N_2 / m^3 CMS]**			**Air demand [m^3_n/h air / m^3_n/h N_2]**		
			EXP	SIM	Φ [%]	EXP	SIM	Φ [%]
0	59	0.0485	97.35	97.60	-0.257	3.18	3.147	1.038
5	54	0.0530	95.85	97.15	-1.352	3.16	3.125	1.108
10	49	0.0584	93.9	95.40	-1.597	3.17	3.126	1.388
15	44	0.0650	91.5	93.21	-1.865	3.18	3.129	1.604

Tab. 5.2.3-2 PSA performance at different cutting times at product purity of 10 ppm O_2

Cutting time [s]	**Purge time [s]**	**Purge flow rate [m^3_n/h]**	**Productivity [m^3_n/h N_2 / m^3 CMS]**			**Air demand [m^3_n/h air / m^3_n/h N_2]**		
			EXP	SIM	Φ [%]	EXP	SIM	Φ [%]
0	59	0.0485	29.64	26.14	11.795	7.78	8.601	-10.553
5	54	0.0530	30.10	29.31	2.616	7.49	7.685	-2.603
10	49	0.0584	30.10	30.65	-1.825	7.42	7.281	1.873
15	44	0.0650	30.10	30.95	-2.831	7.20	7.097	1.431

5.3 Effect of plant design

5.3.1 Flow resistances in the piping system

The rates of pressure build-up and fall-off influence the main driving forces of adsorption and desorption during the PSA cyclic operation. Hence, the issue of pressure drop in the system comes to the fore when optimising the process performance. Whereas the column dimensions and armatures, together with the size of the adsorbent pellets, are selected at the plant design stage, the performance of already existing PSA plants can still be improved by the proper adjustment of controlled flow resistances in the piping system. Therefore, the influence of the regulation of controlled flow resistances in the piping system on the PSA performance indicators is investigated at reference process conditions at a product purity level of 1000 ppm O_2. Experimental results are presented in Tab. 5.3.1-1 and Fig. 5.3.1-1.

As demonstrated in Fig. 5.3.1-1, controlled flow resistances in the piping system have an evident impact on the dynamic behaviour of the PSA system and, thus, a significant effect on

the process performance. The control valve in the feed pipeline mainly regulates the volume ratio of the co-current feed and counter-current backflow streams in the adsorber column during the pressurisation step. As shown in Fig. 5.3.1-1a, the favourable stem position was found at an opening of 53 %. This indicates an optimal amount of product gas reversed to the system as a backflow; not so excessive as to decrease the productivity, and not so insufficient as to slow down the pressure build-up in the system or to cause a premature adsorber breakthrough due to dispersion effects. Moreover, when adjusting the feed control valve to the favourable stem position, the productivity increases by 2.94 % and the air demand decreases by 2.86 % in relation to the process with minimised controlled flow resistances in the PSA piping system, according to the description specified in Chapter 3.2.

Tab. 5.3.1-1 Experimental PSA performance at various controlled flow resistances in the piping system at reference process conditions at product purity level of 1000 ppm O_2

	Stem position [%-opening]	**Productivity [m^3_n/h N_2 / m^3 CMS]**	**Air demand [m^3_n/h air / m^3_n/h N_2]**
Feed pipeline	100	80.67	3.49
	72	82.60	3.40
	53*	83.04	3.39
	34	82.60	3.42
	25	81.92	3.44
	15	81.72	3.45
	6	80.13	3.49
Tail-gas pipeline	100*	80.67	3.49
	81	80.67	3.51
	53	80.03	3.53
	25	74.87	3.62
	15	67.15	3.85
Equalisation pipeline	100	80.67	3.49
	75	83.50	3.41
	50	89.65	3.22
	25*	94.71	3.19
	5	95.37	3.39

* Favourable stem position

Considering the tail-gas pipeline in Fig. 5.3.1-1b, it is shown that any increase of the flow resistance causes a declined PSA performance due to the reduction of the driving force for the desorption process, resulting in a deterioration of the fixed-bed regeneration.

The pressure equalisation step is introduced to the cycle mainly for the reduction of operating costs, since the already compressed and purified air can be transferred partly to the adjacent column. Control valves in pressure equalisation pipelines (Top + Bottom) regulate the volume of gas exchanged between both of the columns during the equalisation step, as well as the subsequent starting pressure for pressurisation and blow-down steps, respectively. Since it acts as an idle period during the PSA operation, the time of the pressure equalisation step should remain as short as possible. It is expected that the complete pressure alignment to the arithmetic average level, by minimising the flow resistance, would lead to the minimal air demand. However, during the rapid pressure reduction in the high-pressure column a simultaneous desorption of the fast-adsorbing gas takes place. Thus, the desorbed oxygen is eventually transferred into the low-pressure column, contaminating the previously regenerated adsorbent. Consequently, the adsorption capacity in the following production step is declined. For this

reason, the optimum position of stems was found at 25 % opening, as presented in Fig. 5.3.1-1c. When adjusting equalisation control valves to the favourable stem position, the productivity increases by 18.22 % and the air demand decreases by 8.60 % in relation to the process with minimised controlled flow resistances in the PSA piping system. The pressure measured at the top of the adsorber columns after pressure equalisation is presented in Fig. 5.3.1-2. The diagram shows that a remaining pressure difference of about 1.36 bar between the columns after equalisation results in the optimal PSA performance in this plant.

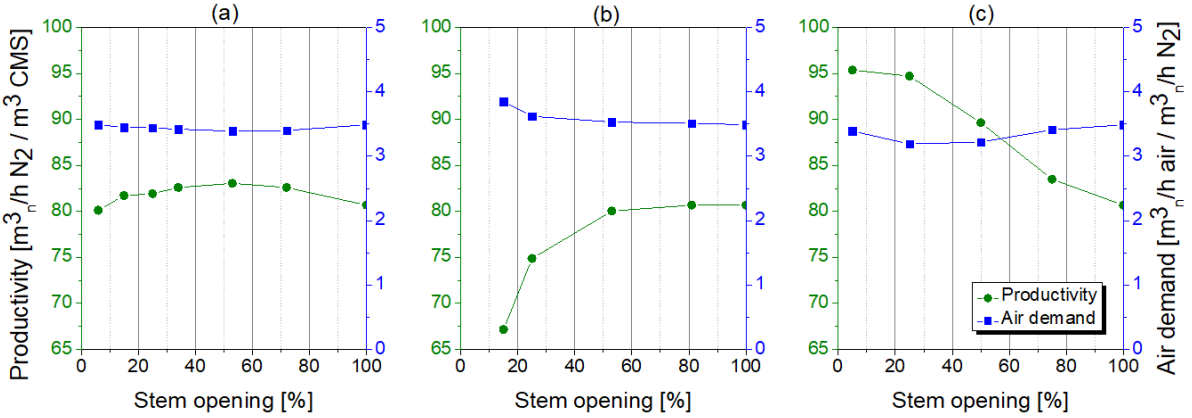

Fig. 5.3.1-1 Experimental PSA performance at various controlled flow resistances in the piping system at reference process conditions at product purity level of 1000 ppm O_2: (a) feed pipeline, (b) tail-gas pipeline, (c) equalisation pipelines

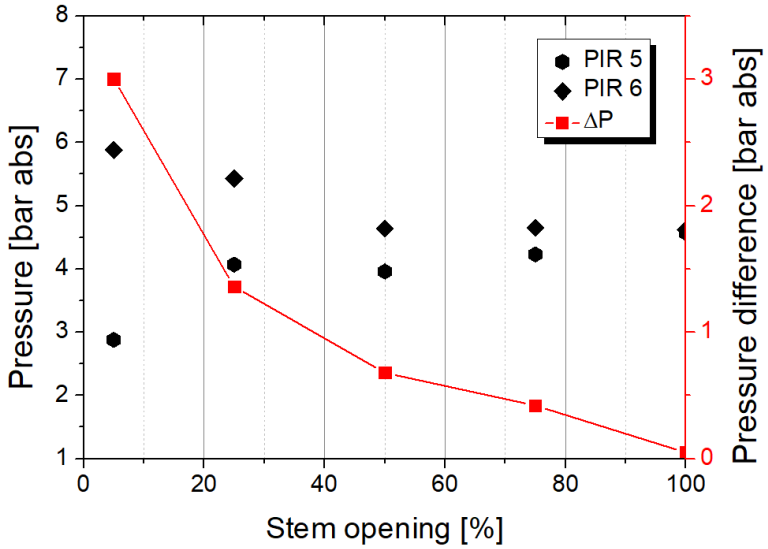

Fig. 5.3.1-2 Pressure in the adsorber columns after pressure equalisation at different stem positions of the equalisation valves (Top/Top + Bottom/Bottom) at reference process conditions at product purity level of 1000 ppm O_2

Control valves in all investigated pipelines were adjusted according to their individual, favourable stem opening. PSA performance indicators were determined and compared to those of the process with minimised controlled flow resistances in the PSA piping system at two product purity levels. The results are presented in Tab. 5.3.1-2. Optimisation of controlled flow resistances, performed by setting the stem position of the discussed control valves to their individually-established favourable position, enhanced the PSA performance regardless the product purity level; however, the effect becomes more significant as the product purity increases. In spite of that, to demonstrate the overall optimum of PSA performance indicators

in the function of controlled flow resistances in the piping system, a multi-parameter optimisation should be executed.

Additionally, the trim of both top and bottom equalisation control valves has been experimentally investigated, whilst other control valves have remained in their individual optimum position of the stem. The effect on the PSA performance of the asymmetric settings was considered at reference process conditions. The results are presented in Tab. 5.3.1-3–4. In the case of pressure equalisation exclusively through the bottom equalisation pipeline, the targeted oxygen residual concentration in the product gas could not be accomplished at both investigated product purity levels. The same effect is observed while performing the pressure equalisation exclusively through the top pipeline at high product purity level.

Tab. 5.3.1-2 Experimental PSA performance at minimised and optimised controlled flow resistances in the piping system at reference process conditions

	Minimised controlled flow resistances		**Optimised controlled flow resistances**		**Increment [%]**	
Product purity [ppm O_2]	10	1000	10	1000	10	1000
Productivity [m^3_n/h N_2 / m^3 CMS]	12.67	80.65	29.64	97.35	133.94	20.71
Air demand [m^3_n/h air / m^3_n/h N_2]	15.93	3.49	7.78	3.18	-51.16	-8.88

At the product purity of 1000 ppm O_2 the favourable pressure equalisation strategy proved to be an asymmetric setting with a 2/3 of the gas transferred through the top equalisation pipeline and a 1/3 through the bottom one. However, at the product purity of 10 ppm O_2, the favourable pressure equalisation strategy maintains a symmetric setting of equalisation control valves.

Tab. 5.3.1-3 Effect of the asymmetric pressure equalisation on the PSA performance at product purity of 1000 ppm O_2

Pressure equalisation (Top) + (Bottom)	**Stem position [%-opening]**	**Productivity [m^3_n/h N_2 / m3 CMS]**	**Air demand [m^3_n/h air / m^3_n/h N_2]**
(0) + (1)	0 + 100	-	-
(1/3) + (2/3)	12.5 + 37.5	84.50	3.47
(1/2) + (1/2)	25 + 25	97.35	3.18
(2/3) + (1/3)*	37.5 + 12.5	99.15	3.13
(1) + (0)	100 + 0	84.25	3.52

* Favourable pressure equalisation strategy

The observed effect is directly related to the development of the mass transfer zone within the adsorbent fixed-bed in the cyclic steady state (CSS) conditions, which can be tracked via the

measurement of temperature alteration during the production step; assuming that the propagation velocity of the temperature front is not higher than of the concentration front. Since the PSA experimental unit can be considered as a non-adiabatic system, the formation of a pure thermal wave front, as described by Pan and Basmadjian [105], will not occur. The experimental temperature profiles at investigated product purity levels are presented in Fig. 5.3.1-3.

Tab. 5.3.1-4 Effect of the asymmetric pressure equalisation on the PSA performance at product purity of 10 ppm O_2

Pressure equalisation (Top) + (Bottom)	**Stem position [%-opening]**	**Productivity [m^3_n/h N_2 / m^3 CMS]**	**Air demand [m^3_n/h air / m^3_n/h N_2]**
(0) + (1)	0 + 100	-	-
(1/3) + (2/3)	12.5 + 37.5	22.40	9.83
(1/2) + (1/2)*	25 + 25	29.64	7.78
(2/3) + (1/3)	37.5 + 12.5	25.70	8.65
(1) + (0)	100 + 0	-	-

* Favourable pressure equalisation strategy

At low product purity the gas velocity in the packed-bed is relatively high so that the MTZ becomes elongated due to mass dispersion effects. In that case, an increase of the flow resistance in the bottom equalisation pipeline reduces the driving force for the desorption process, which results in the minor transfer of the highly oxygen-enriched gas into the bottom part of the adjacent column. Thus, the adsorption capacity in the subsequent production step is not harmfully affected. Moreover, the appropriate adjustment of the flow resistance in the top equalisation pipeline allows the straightforward transfer of the highly purified nitrogen gas into the top part of the neighbour column which supports the subsequent backflow stream.

On the other hand, at high product purity, the gas velocity in the packed-bed is relatively low and the mass transfer occurs mainly in the bottom part of the adsorbent fixed-bed. In that case, the top part of the bed serves as the nitrogen safeguard bulk that ensures nearly complete oxygen rejection from the compressed air feed stream. The symmetric setting of equalisation control valves results in the highest performance, since the top part of both adsorber columns is not contacted with oxygen-enriched gas – neither in co- nor counter-current pressure equalisation stream, so the nitrogen safeguard bulk is not harmfully affected. The graphical representation of the MTZ with related favourable pressure equalisation strategies at investigated product purity levels is introduced in Fig. 5.3.1-4. These results motivate a more realistic simulation of mass transfer effects in PSA adsorbers as being state-of-the-art today.

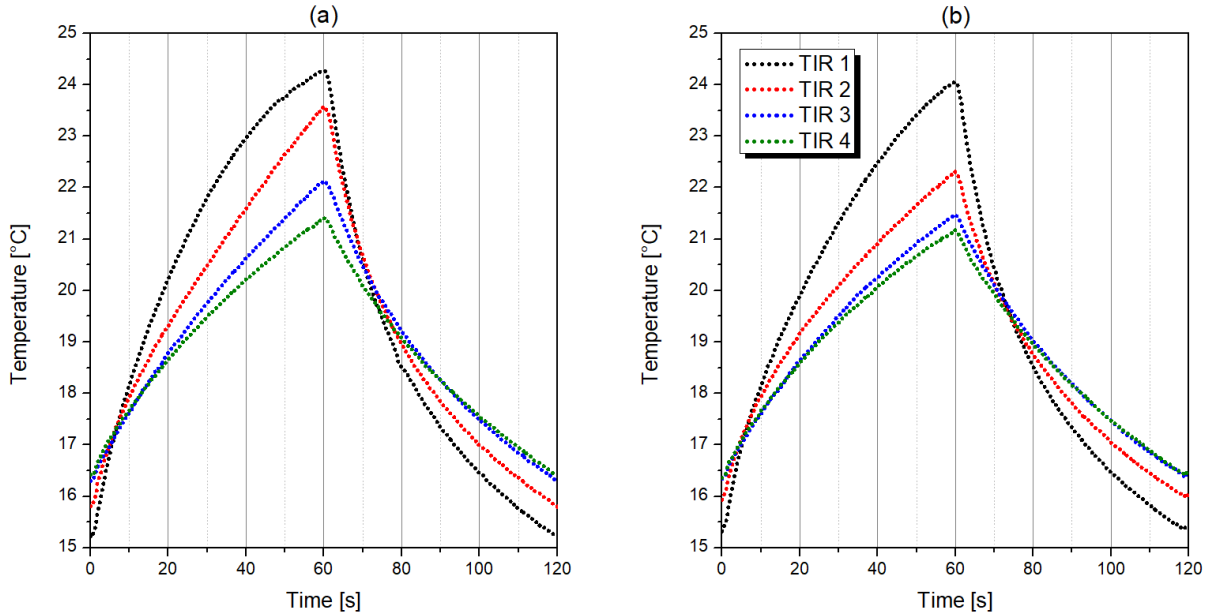

Fig. 5.3.1-3 Experimental temperature profiles along the adsorbent fixed-bed at reference process conditions: (a) at product purity of 1000 ppm O_2, (b) at product purity of 10 ppm O_2

Therefore, taking into consideration observed effects of controlled flow resistances in the piping system, their influence on PSA performance indicators is studied numerically. In order to do so, only specific flow coefficients *Cv* of valve models V, representing flow resistances in considered pipelines, are adjusted; while all other valve models V in the process simulator representing controlled flow resistances, are simulating the action of the ball valve. This strategy implemented in process simulator illustrates the corresponding method applied to experimental research. Introduced *Cv* values are selected according to the strategy given in Appendix 10.6. Results presenting the influence of individually adjusted flow resistances in particular pipelines are shown in Tab. 5.3.1-5 and Fig. 5.3.1-5.

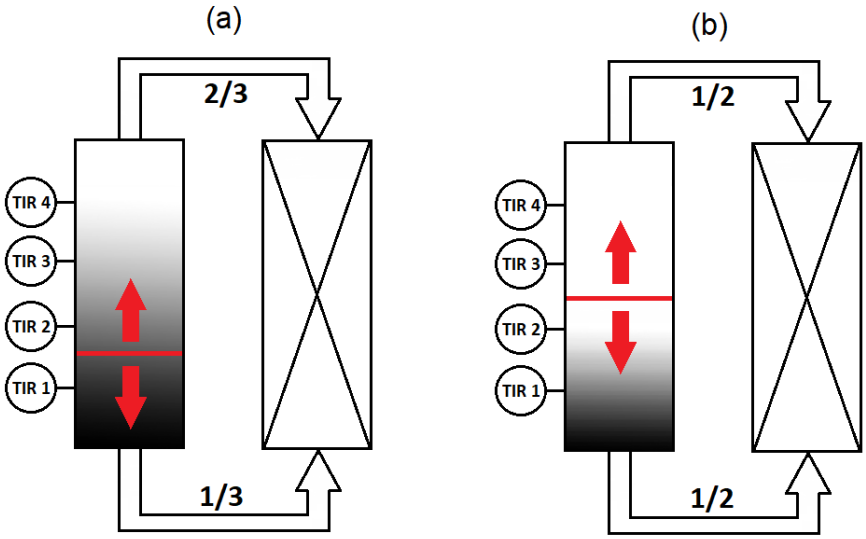

Fig. 5.3.1-4 Visual demonstration of the oxygen MTZ development with related favourable pressure equalisation strategy: (a) at product purity of 1000 ppm O_2, (b) at product purity of 10 ppm O_2

Tab. 5.3.1-5 PSA performance at different at various controlled flow resistances in the piping system at reference process conditions at product purity level of 1000 ppm O_2

	Stem position [%-opening]	Cv [kmol/s/bar]	Productivity [m^3_n/h N_2 / m^3 CMS]			Air demand [m^3_n/h air / m^3_n/h N_2]		
			EXP	SIM	Φ [%]	EXP	SIM	Φ [%]
Feed pipeline (V2, V3)	6	5.0×10^{-4}	80.13	70.4	12.14	3.49	3.806	15.23
	15	1.0×10^{-3}	81.72	70.1	14.22	3.45	3.811	-10.46
	25	5.0×10^{-3}	81.92	69.9	14.67	3.44	3.810	-10.76
	35	1.5×10^{-2}	82.60	69.9	15.38	3.42	3.809	-11.37
	53	5.0×10^{-1}	83.04	70.2	15.46	3.39	3.797	-12.01
Tail gas pipeline (V6, V7)	15	1.5×10^{-5}	67.15	48.3	28.07	3.85	4.602	-19.53
	25	3.0×10^{-5}	74.87	58.5	21.86	3.62	4.150	-14.64
	53	9.0×10^{-5}	80.03	66.5	16.91	3.53	3.889	-10.17
Equalisation pipeline (V10, V11)	5	1.1×10^{-5}	95.37	95.1	0.28	3.39	3.335	1.62
	25	2.5×10^{-5}	94.71	97.5	-2.95	3.19	3.149	1.29
	50	3.0×10^{-5}	89.65	97.0	-8.20	3.22	3.140	2.48
	75	7.4×10^{-5}	83.50	93.8	-12.34	3.41	3.142	7.86

The process simulation predicts qualitatively the PSA performance at different controlled flow resistances in the piping system. However, the accurate modelling of the pressure drop across the specific control valves is strongly associated with the proper fitting of experimental pressure profiles measured at the top of adsorbers, which can be seen in Appendix 10.6.

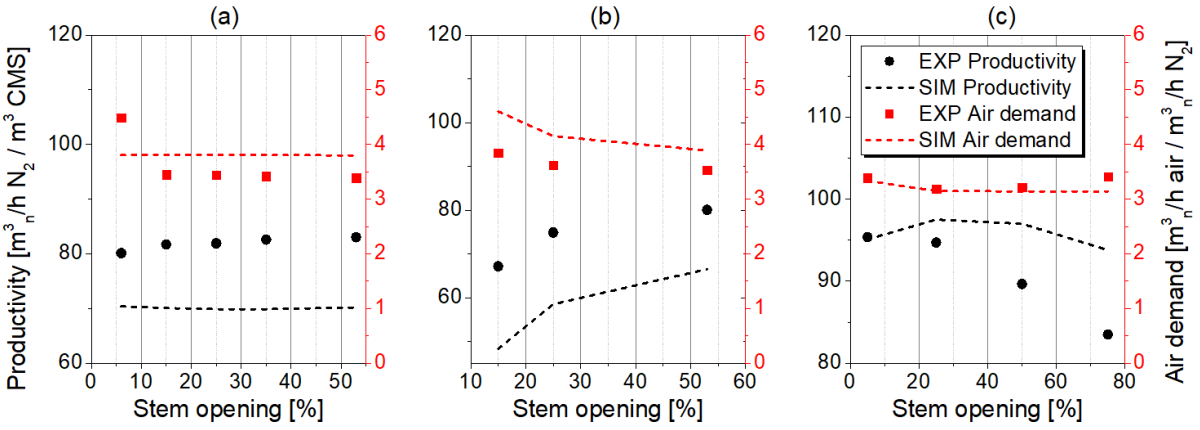

Fig. 5.3.1-5 Experimental and simulated PSA performance at various controlled flow resistances in the piping system at reference process conditions at product purity level of 1000 ppm O_2: (a) feed pipeline, (b) tail-gas pipeline, (c) equalisation pipelines

Regarding the regulation of flow resistances in the feed pipeline, the productivity is underestimated since the mathematical model overestimates the pressure at the beginning of the production step, as shown in Fig. A.6-2. For that reason, a higher gas flow rate along the column is predicted, which intensifies the mass dispersion effect. As a result, the premature column breakthrough occurs during process simulation. The relative error of productivity approximation is rather insensitive to modifications of flow resistances since the quality of pressure profiles estimation, as presented in Fig. A.6-2a–d, does not vary significantly. In the case of flow resistances modification in the tail gas pipeline, the productivity is strongly underestimated since the mathematical model does not predict correctly the pressure changes

during regeneration step, as shown in Fig. A.6-4. Especially, the presumed desorption pressure level of 1 bar abs is not achieved while numerical simulation. It can be seen in Fig. A.6-4a that the quality of pressure profiles estimation decreases while increasing the pressure drop across the control valve. For that reason, the relative error of PSA performance approximation increases notably. Concerning the regulation of flow resistances in the equalisation pipelines, the productivity is slightly overestimated since the mathematical model underestimates the pressure at the beginning of the blow-down step, as shown in Fig. A.6-3. Therefore, the larger driving force for desorption; hence, better regeneration of the packed bed is predicted by the process simulation. Moreover, as shown in Fig. A.6-3a, the quality of pressure profiles estimation decreases while increasing the pressure drop across the control valves. As a result, the relative error of PSA performance approximation is elevated. Besides, relative errors of the air demand approximation, presented in Tab. 5.3.1-5, originate in inaccuracies of the productivity prediction.

Tab. 5.3.1-6 *Cv* values applied for investigating the asymmetric pressure equalisation

Pressure equalisation (Top) + (Bottom)	**Stem position [%-opening]**	**Cv [kmol/s/bar] (Top)**	**Cv [kmol/s/bar] (Bottom)**
(0) + (1)	0 + 100	-	-
(1/3) + (2/3)	12.5 + 37.5	1.25×10^{-5}	2.85×10^{-5}
(1/2) + (2/2)	25 + 25	2.50×10^{-5}	2.50×10^{-5}
(2/3) + (1/3)	37.5 + 12.5	2.85×10^{-5}	1.25×10^{-5}
(1) + (0)	100 + 0	-	-

Additionally, the effect of asymmetric settings of equalisation valves on the PSA performance was studied numerically, whilst other control valves have remained in their individual optimum position of the stem. Applied flow coefficients *Cv* are presented in Tab. 5.3.1-6. The results are shown in Tab. 5.3.1-7–8 and Fig. 5.3.1-6–7.

Tab. 5.3.1-7 PSA performance at asymmetric pressure equalisation at reference process conditions at product purity level of 1000 ppm O_2

No.	**Pressure equalisation (Top) + (Bottom)**	**Productivity [m^3_n/h N_2 / m^3 CMS]**			**Air demand [m^3_n/h air / m^3_n/h N_2]**		
		EXP	SIM	Φ [%]	EXP	SIM	Φ [%]
1	(0) + (1)	-	-	-	-	-	-
2	(1/3) + (2/3)	84.50	89.40	-5.80	3.47	3.386	2.42
3	(1/2) + (2/2)	97.35	97.60	-0.26	3.18	3.147	1.04
4	(2/3) + (1/3)	99.15	98.70	0.45	3.13	3.139	-0.29
5	(1) + (0)	84.25	51.40	38.99	3.52	4.766	-35.40

The model predicts the influence of asymmetric settings of equalisation valves sufficiently, regardless of the applied strategy and purity level. The only exception remains the simulation of the PSA process with a fully-opened top equalisation valve and a fully-closed bottom equalisation valve at product purity of 1000 ppm O_2. The productivity is significantly underestimated, most probably due to the overestimation of gas interstitial velocity during the

equalisation step. Therefore, enhanced oxygen transfer from the high-pressure column to the low-pressure column results in the packed-bed contamination, especially in the top section of the adsorber column. Consequently, the air demand value is significantly overestimated.

Tab. 5.3.1-8 PSA performance at asymmetric pressure equalisation at reference process conditions at product purity level of 10 ppm O_2

No.	Pressure equalisation (Top) + (Bottom)	Productivity [m^3_n/h N_2 / m^3 CMS]			Air demand [m^3_n/h air / m^3_n/h N_2]		
		EXP	SIM	Φ [%]	EXP	SIM	Φ [%]
1	(0) + (1)	-	-	-	-	-	-
2	(1/3) + (2/3)	22.40	16.80	25.0	9.83	13.039	-32.64
3	(1/2) + (2/2)	29.64	26.14	11.79	7.78	8.601	-10.55
4	(2/3) + (1/3)	25.70	25.10	2.33	8.65	8.962	-3.61
5	(1) + (0)	-	-	-	-	-	-

At both product purity levels, the relative error of simulation decreases with increasing flow resistance in the bottom equalisation pipeline. In this specific case, the gas is transferred mostly co-currently from the high-pressure column to the low-pressure column. Since the top section of the adsorber column is predominantly occupied by nitrogen, the effect of enhanced oxygen desorption causing the packed bed contamination is probably balanced with the gas near-wall channelling effect, which is inevitable in practice. Thus, the oxygen-enriched gas accumulates in columns voids and does not affect the separation performance within the adsorbent bed itself during the transition phase. The outcome is more pronounced at a product purity level of 10 ppm O_2 rather than at 1000 ppm O_2.

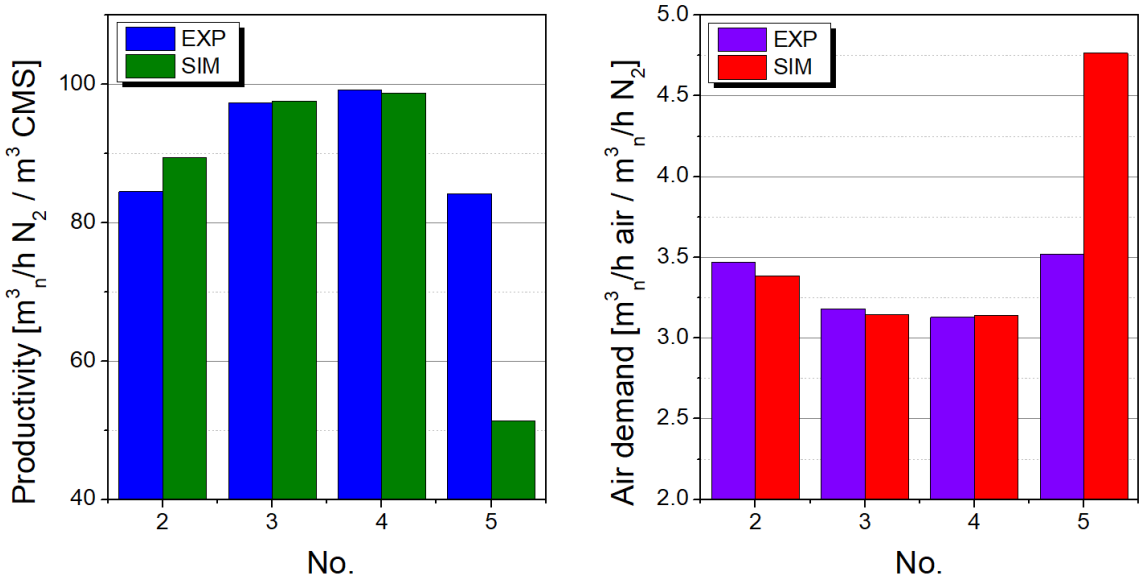

Fig. 5.3.1-6 PSA performance at asymmetric pressure equalisation at reference process conditions at product purity level of 1000 ppm O_2

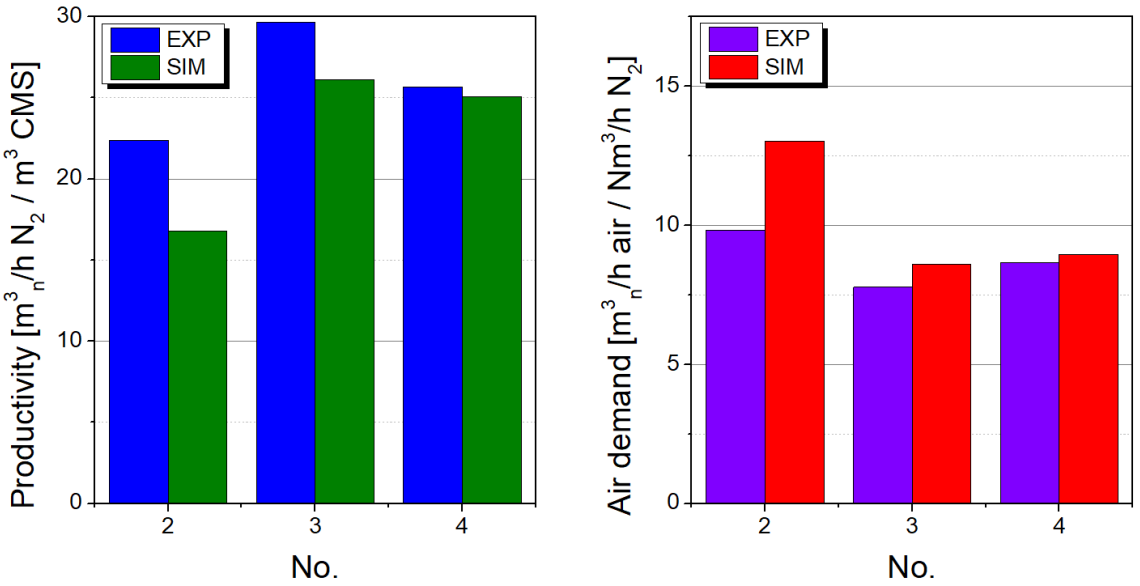

Fig. 5.3.1-7 PSA performance at asymmetric pressure equalisation at reference process conditions at product purity level of 10 ppm O_2

5.3.2 Volume of the N_2-receiver tank

The N_2-receiver tank is implemented in the PSA unit in order to operate the cyclic process with a constant flow rate of a high-pressure nitrogen stream that is requested in the majority of industrial applications. Moreover, a mixing space for the product gas is provided which is generated during the production step at inconstant composition. In the considered pilot plant, the purge and the backflow streams, directed counter-currently to the adsorber columns, are served also from the N_2-receiver tank. The selection of the smallest possible buffer vessel is of essential importance while aiming for a reduction of the unit footprint. However, an insufficient volume of the tank would give rise to enlarged pressure differences in the system and could be a reason for reduced unit performance. Thus, the influence of the N_2-receiver volume on the PSA performance indicators is investigated in the range of 5 – 12 L by replacing the originally assembled tank by smaller tanks. The results are presented in Tab. 5.3.2-1–2 and Fig. 5.3.2-1.

During the PSA operation, the pressure maintained in the N_2-receiver directly affects the gas flow rate through the packed bed which consequently influences the mass transfer conditions. The experimental pressure profiles of adsorbers and product buffer tank at different volume ratios of the N_2-receiver to the adsorber column are presented in Fig. 5.3.2-2. As a consequence of the co-current pressurisation of the packed bed with a simultaneous counter-current backflow of product, the pressure in the N_2-receiver tank declines at the beginning of the PSA cycle. That pressure downfall becomes more extensive as the volume of the product buffer tank is reduced. An increased pressure difference between the adsorber column and the N_2-receiver is created which causes an enlarged gas velocity in the adsorbent fixed-bed and, therefore, a decreased contact time of gas and solid phases. Furthermore, the final production pressure is achieved in the adsorber column with a significant delay, diminishing the efficiency of the adsorption process. For that reason, at every investigated process condition, the reduction of the volume ratio of the N_2-receiver tank to the adsorber column results in lower nitrogen productivity and higher air demand.

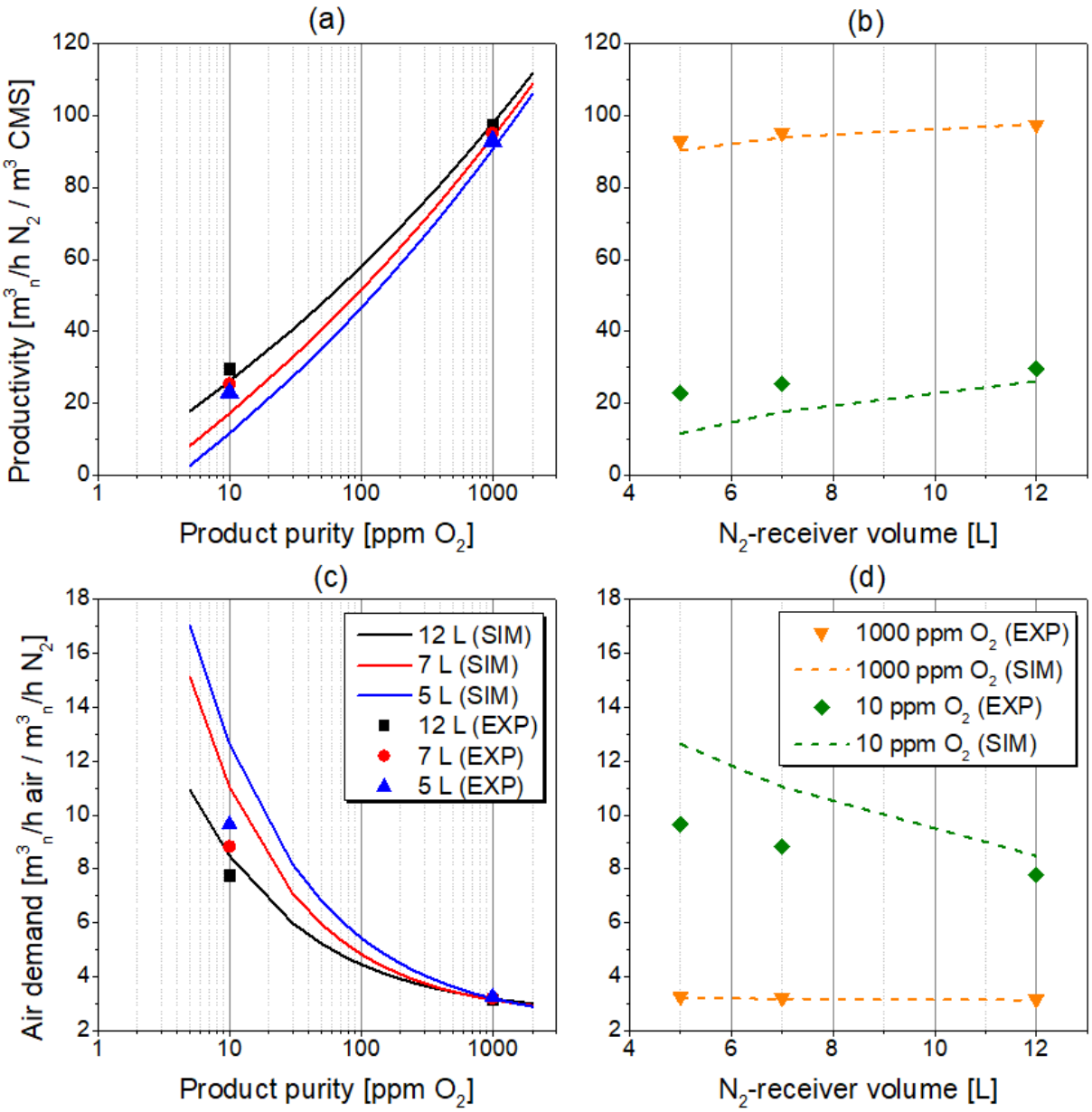

Fig. 5.3.2-1 PSA performance at different N_2-receiver volumes: (a, b) productivity; (c, d) air demand; (a, c) as a function of product purity; (b, d) as a function of N_2-receiver volume

However, the volume reduction of the product buffer vessel is recommended when low purity nitrogen is required. In this case, the gas velocity in the packed column is already relatively high; so that its further increase caused by the enlarged pressure difference between the adsorber column and the N_2-receiver tank does not have a significant impact on the mass transfer dynamics. The modification between largest and smallest volume of N_2-receiver causes a decrease in productivity and an increase in air demand merely by 5 % and 3 %, respectively. On the other hand, the generation of nitrogen at a high purity level demands a product buffer vessel of large volume. In this case, every acceleration of the gas within the adsorber causes an enlargement of the mass transfer zone, leading to the premature breakthrough of oxygen. Thus, modification between the largest and the smallest volume of N_2-receiver causes a decrease in the productivity and an increase in the air demand by nearly 23.5 % and 24 %, respectively. This is unacceptable for the purposes of industrial PSA operations.

Tab. 5.3.2-1 PSA performance at different N_2-receiver volumes at product purity of 1000 ppm O_2

N_2-receiver volume [L]	**Productivity [m^3_n/h N_2 / m^3 CMS]**			**Air demand [m^3_n/h air / m^3_n/h N_2]**		
	EXP	SIM	Φ [%]	EXP	SIM	Φ [%]
5	92.80	90.30	2.694	3.27	3.239	0.948
7	95.00	93.90	1.158	3.22	3.187	1.025
12	97.35	97.60	-0.257	3.18	3.147	1.038

Tab. 5.3.2-2 PSA performance at different N_2-receiver volumes at product purity of 10 ppm O_2

N_2-receiver volume [L]	**Productivity [m^3_n/h N_2 / m^3 CMS]**			**Air demand [m^3_n/h air / m^3_n/h N_2]**		
	EXP	SIM	Φ [%]	EXP	SIM	Φ [%]
5	22.82	11.00	51.797	9.65	18.282	-89.451
7	25.47	17.20	32.470	8.84	12.273	-38.835
12	29.64	26.14	11.795	7.78	8.601	-10.553

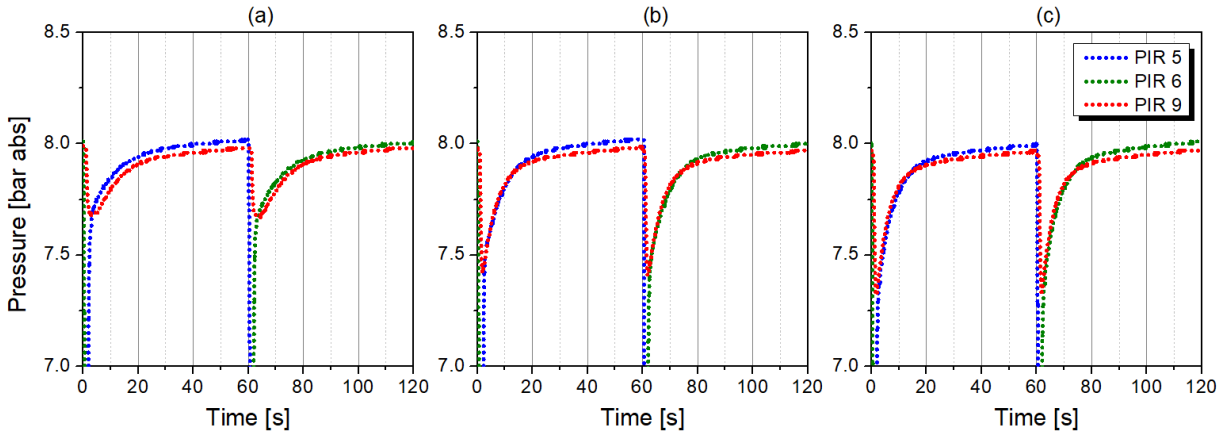

Fig. 5.3.2-2 Experimental pressure profiles of adsorber columns and N_2-receiver tank at different N_2-receiver volumes: (a) 12 L, (b) 7 L, (c) 5 L

Tab. 5.3.2-1 shows that the model predicts the influence of the N_2-receiver volume sufficiently at the lower product purity level of 1000 ppm O_2. However, as the product purity requirement increases, the PSA simulation exhibits a significant relative error with the reduction of N_2-receiver volume. As presented in Fig. 5.3.2-3, the quantitative representation of experimental pressure profiles becomes more challenging the smaller the tank volume. Dynamic process simulation exhibits a bigger slope of the N_2-receiver pressure profile during the pressurisation and back-flow steps, respectively. Therefore, the superficial velocity of the gas in the packed bed is overestimated, especially in the initial phase of the production step, so the contact time between phases is reduced and the premature column breakthrough occurs consequently. Since the efficient production of high-purity nitrogen (10 ppm O_2) is promoted at prolonged cycle times, as already proofed in Chapter 5.2.1, the productivity is underestimated to maintain the target purity level. Hence, the air demand is overestimated accordingly.

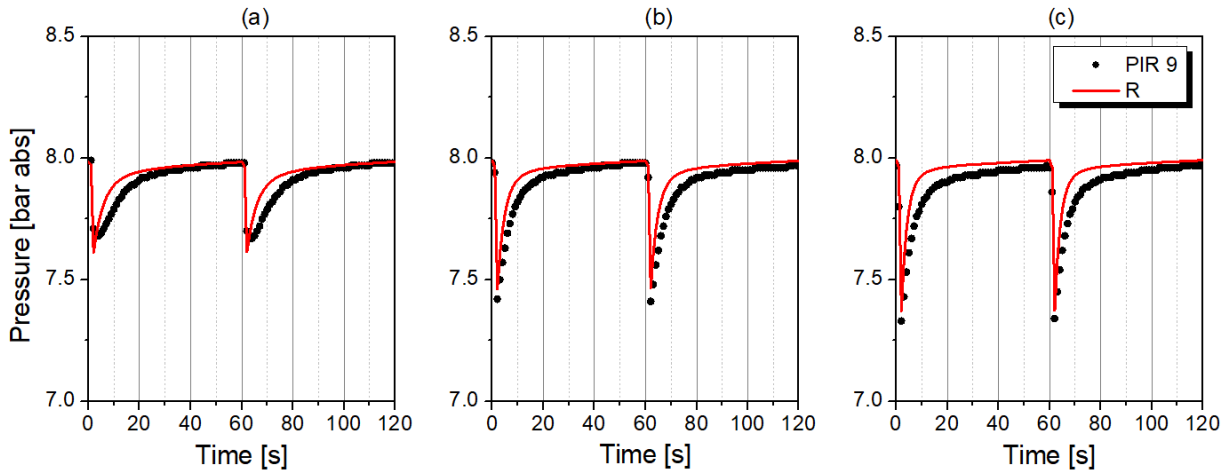

Fig. 5.3.2-3 Experimental and simulated pressure profiles of N_2-receiver tank at different N_2-receiver volumes: (a) 12 L, (b) 7 L, (c) 5 L

5.4 Accuracy evaluation of the results

The relative error of simulated PSA performance indicators increases significantly with increased nitrogen purity. At the investigated product purity of 10 ppm O_2, the largest deviation equals 51.80 % in case of productivity and -89.45 % in case of air demand, which was detected while the PSA operation with 5 L N_2-receiver tank. In contrast, at product purity of 1000 ppm O_2, the largest deviation equals 38.99 % in case of productivity and -35.40 % in case of air demand, which was identified during the PSA operation with asymmetric exploitation of equalisation valves, while the top valve is fully-opened and the bottom valve is fully-closed.

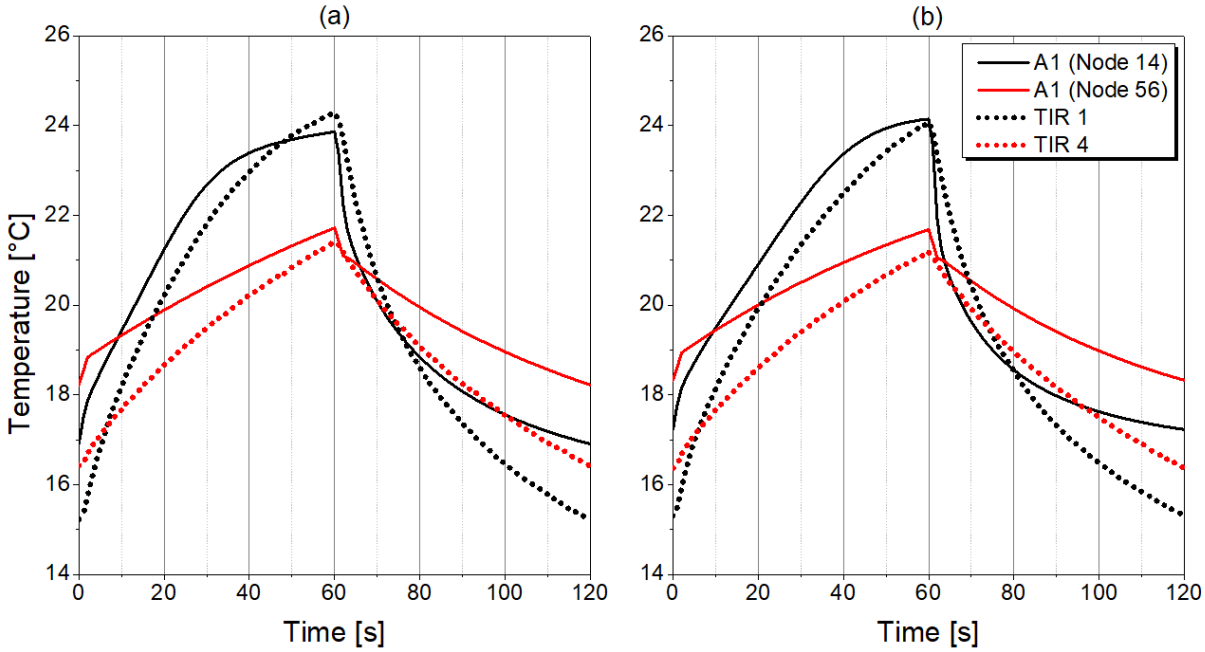

Fig. 5.4-1 Experimental and simulated temperature profiles at selected positions of the adsorber during the PSA reference cycle: (a) at product purity of 1000 ppm O_2, (b) at product purity of 10 ppm O_2

Due to the fact that the slopes of presented performance indicators curves become significantly larger at increased purity requirement, every minor inaccuracy in oxygen concentration measurement, even in the range of observational error, has a substantial impact on the

determined productivity and air demand values. For instance, if simulating the PSA process at fixed productivity, the highest relative errors obtained at product purity of 10 ppm O_2 would correspond to an absolute error of merely 12.09 ppm O_2 in purity prediction, and 0.238 m^3_n/h air / m^3_n/h N_2 in air demand prediction; both of which do not amount to much in an absolute scale. This issue would be unlikely to occur while using CMS adsorbents of improved separation efficiency, especially in the high-purity range; since they exhibit less pronounced gradients of productivity and air demand in the function of nitrogen purity. Therefore, these materials would probably be represented better by the PSA mathematical model rather than the originally selected Shirasagi MSC CT-350 grade in this work.

However, a few general conclusions can be stated. At almost every investigated process condition, the developed model underestimates the productivity and consequently overestimates the air demand at a product purity level of 10 ppm O_2. The possible explanations of this effect include minor inaccuracies originating both in PSA experimental set-up and in the mathematical description of the process, e.g.

- underestimation of the adsorbent equilibrium loading by the IAST approach as presented in Fig. 3.3-3, most likely due to coarse IAST theory assumptions as neglecting adsorbate-adsorbate and adsorbate-surface interactions as well as omitting heterogeneous surface of CMS;
- lack of experimental equilibrium data of pure oxygen adsorption at very low pressure (< 0.01 bar abs) as presented in Fig. 3.3-1a, as well as deviations in the amount adsorbed prediction by Sips isotherm model at low pressures;
- inaccuracies in the estimation of oxygen mass transfer rate according to Darken approach due to inexact calculation of the slope of isotherm at very low pressure;
- inhomogeneous gas distribution along the adsorber column in the pilot-plant and therefore channelling effects;
- adsorption/desorption of other air components, especially carbon dioxide and moisture, which most likely cause superimposing effects on the gas temperature along the adsorber column, as presented in Fig. 5.4-1; or
- imprecise evaluation of the multi-component diffusion process in the pore system of the CMS adsorbent.

It is highly possible that different inaccuracies are overlapping, therefore increasing the simulation error of the performance indicators. It is most likely, that – in combination with a modified IAST approach – the biggest improvement of the model is possible by introducing an additional gaseous key component combining the effects of moisture and carbon dioxide adsorption for a better simulation of their thermal influences. However, the measurement of pure oxygen isotherm at very low pressure (1×10^{-5} bar abs) could also bring a certain improvement in simulation accuracy.

6 PSA process dynamics

After validation of the mathematical model, a discussion of column dynamics is performed. Breakthrough curves of the adsorber column during PSA cycle at product purity levels of 1000, 100, and 10 ppm O_2 are presented in Fig. 6-1. The product gas is generated with variant composition; therefore, the integral average of the oxygen concentration within the production step corresponds to the required nitrogen purity level, which is marked with dotted lines. During blow down and purge steps, the oxygen concentration at the top of the column refers to the product gas accumulated in the N_2-receiver tank. At the time of co- and counter-current equalisation steps, the oxygen concentration in the gas phase rapidly increases as a consequence of either oxygen desorption whereas the total pressure in the adsorber is reduced, or the transfer of oxygen-enriched gas from the adjacent column while the total pressure in the adsorber is increased.

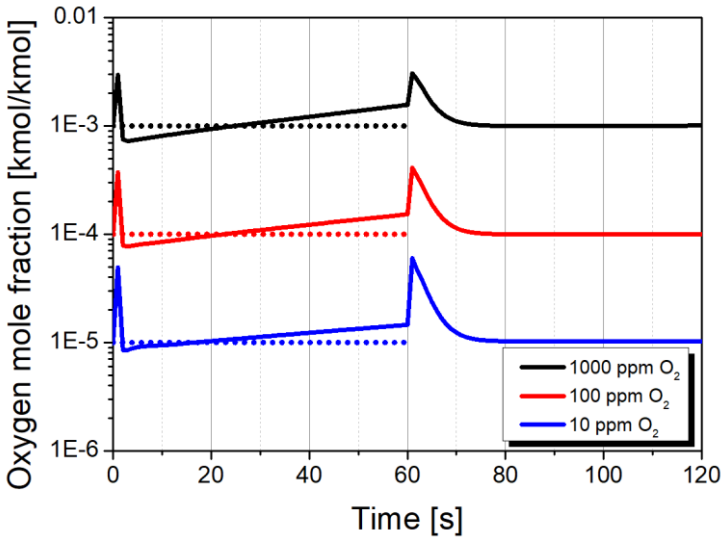

Fig. 6-1 Oxygen breakthrough curves during the PSA reference cycle at different product purity levels; here time ranges of 0 – 60 s and 60 – 120 s indicate production and regeneration steps, respectively; dotted lines represent the target nitrogen purity level

The MTC of oxygen and nitrogen during the PSA cycle at the product purity of 1000 O_2 are presented in Fig. 6-2. It is evident that the MTC of oxygen is remarkably higher than of nitrogen due to the elevated mass transfer rate in the CMS pore system. According to the Darken relation implemented in the definition of the mass transfer coefficient presented in Eq. 3.5-6, the MTC increases with adsorbent loading, therefore increases during adsorption in the column accordingly. In contrast, the MTC decreases during regeneration since adsorbent loading decreases. No significant dissimilarity in the course of MTC curves was detected at different nitrogen purity levels. Surprisingly, a larger value of the MTC is detected during the desorption than during the adsorption. Since the blow-down step is performed at atmospheric pressure level, values of oxygen and nitrogen partial pressure are lower than 1, which consequently affects the MTC increase for both components, as stated in Eq. 3.5-6. The finding suggests that the mass transfer associated with desorption occurs faster than associated with adsorption. Therefore, the mean oxygen and nitrogen mass transfer rates were calculated as an integral average based on curves presented in Fig. 6-3. The results are shown in Tab. 6-1.

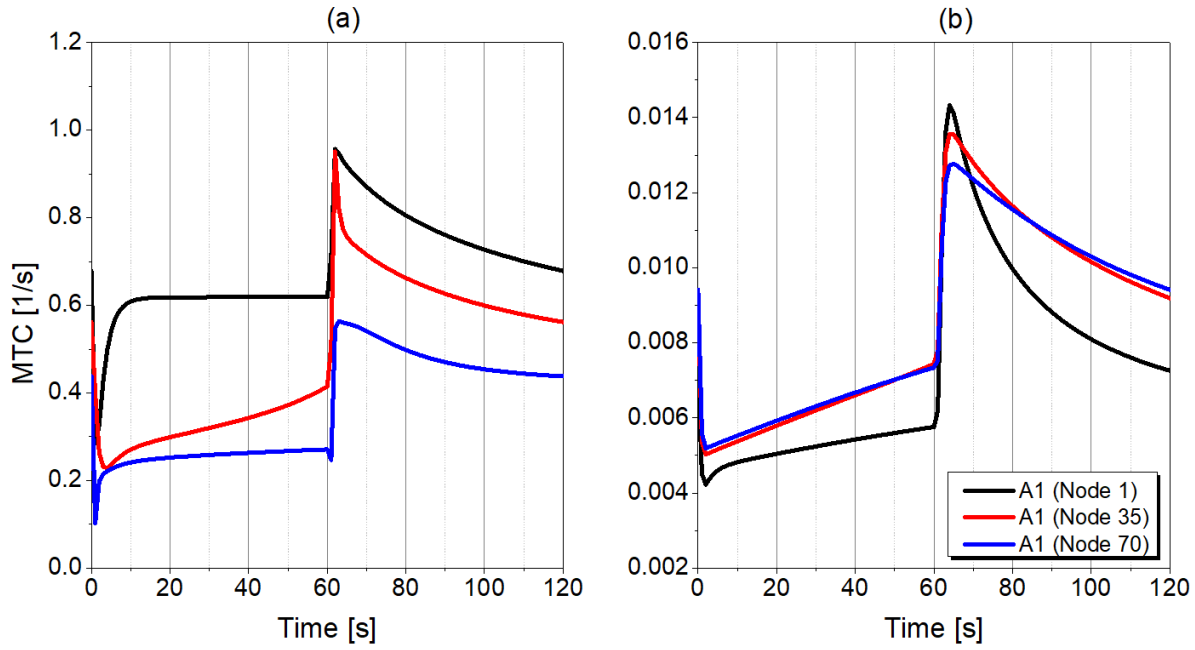

Fig. 6-2 Mass transfer coefficients during the PSA reference cycle at 1000 ppm O_2 at selected positions of adsorber length: (a) MTC of oxygen; (b) MTC of nitrogen; here nodes 1, 35, and 70 indicate the bottom, the middle, and the top of the column, respectively; here time ranges of 0 – 60 s and 60 – 120 s indicate production and regeneration steps, respectively

For both of the components, no notable difference in the average value of mass transfer rates during adsorption and desorption is observed. The finding confirms experimental results presented by Möller et al., showing that the uptake rate during adsorption equals the uptake rate during the desorption [106]. In the bottom section of the adsorber column, a larger mass transfer rate is associated with oxygen rather than nitrogen; despite its significantly lower concentration in the gas phase. In the middle and top sections of the adsorber column, the rate of nitrogen transport dominates. Moreover, it appears in Fig. 6-3 that the oxygen transport occurs very rapidly, while the nitrogen is transferred steadily.

Tab. 6-1 Average mass transfer rates of oxygen and nitrogen during the PSA reference cycle at 1000 ppm O_2 at selected positions of adsorber length

	$\partial w/\partial t$ (average)[kmol/kg/s]			
	Oxygen		**Nitrogen**	
	Adsorption	Desorption	Adsorption	Desorption
Node 1	3.541×10^{-6}	-3.688×10^{-6}	2.380×10^{-6}	-2.414×10^{-6}
Node 35	1.402×10^{-6}	-1.113×10^{-6}	3.370×10^{-6}	-3.432×10^{-6}
Node 70	2.730×10^{-8}	-2.585×10^{-8}	3.471×10^{-6}	-3.535×10^{-6}

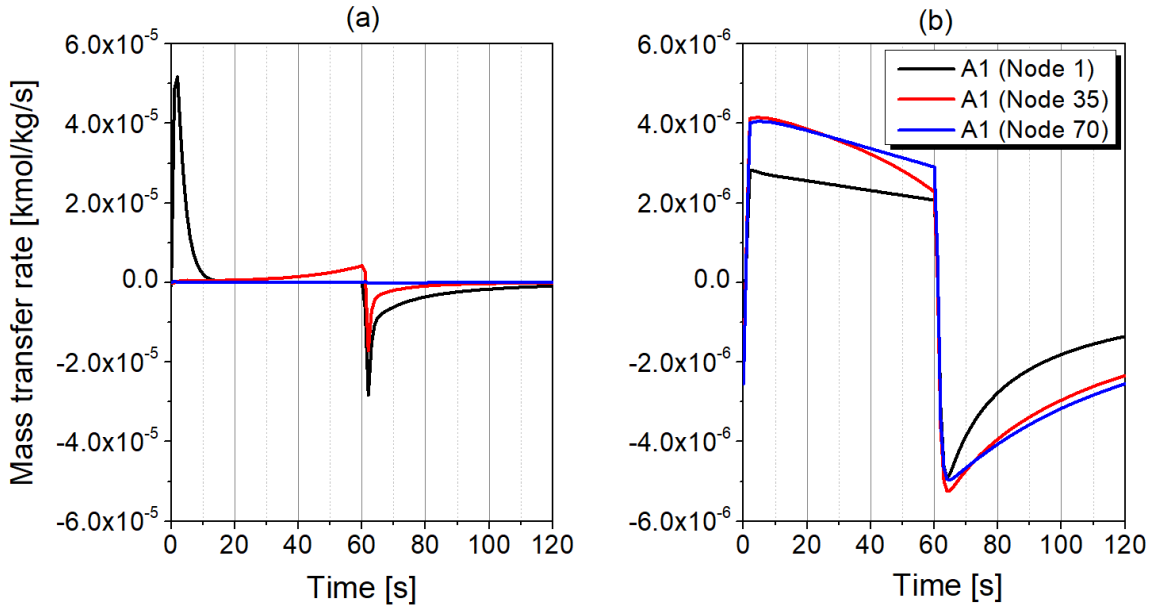

Fig. 6-3 Mass transfer rate during the PSA reference cycle at 1000 ppm O_2 at selected positions of adsorber length : (a) $\partial w/\partial t$ of oxygen; (b) $\partial w/\partial t$ of nitrogen; here nodes 1, 35, and 70 indicate the bottom, the middle, and the top of the column, respectively; here time ranges of 1 – 60 s and 61 – 120 s indicate the production and regeneration steps, respectively

The superficial gas velocity in the adsorber column during PSA cycle at product purity levels of 10 ppm O_2 and 1000 ppm O_2 is presented in Fig. 6-4. The application of the co-current pressurisation by feed with simultaneous counter-current backflow of product results in significantly reduced superficial velocity during adsorption rather than during desorption. Furthermore, a fast counter-current flow rate of the oxygen-enriched gas during the blow-down step enables effective bed regeneration. At the time of equalisation steps, superficial velocity peaks towards positive values whenever the gas is transferred co-currently; and towards negative values whenever the gas is transferred counter-currently into the adjacent adsorber column. No significant difference in the gas superficial velocity is observed at different product purity levels; however, the production of the nitrogen of increased purity is associated with a slightly slower flow of the gas through the column.

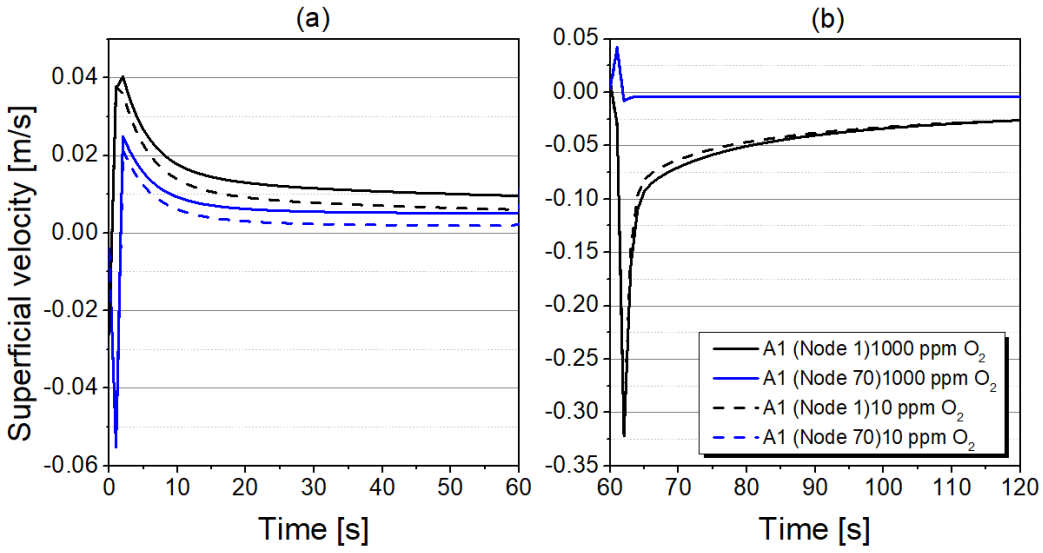

Fig. 6-4 Gas superficial velocity during the PSA reference cycle at different product purity levels at selected positions of adsorber length: (a) during the production; (b) during the regeneration; here nodes 1 and 70 indicate the bottom and the top of the column, respectively

The oxygen MTZ during production and regeneration steps is presented in Fig. 6-5 at product purity levels of 1000 and 10 ppm O_2. The wave-front of oxygen concentration is self-sharpening during adsorption and self-flattering during desorption, which is a result of the favourable-type isotherm. The roll-up effect can be spotted at the time of production step, indicating the replacement of nitrogen molecules by oxygen inside the CMS; most likely due to much faster oxygen kinetics. An extended MTZ along the adsorber occurs in case of lower purity level, which indicates an enhanced mass dispersion caused by the elevated gas superficial velocity. In contrast, at a high nitrogen purity level the MTZ is situated mostly in the bottom part of the bed, so the top part is occupied almost exclusively by purified nitrogen gas. The corresponding MTZ of nitrogen is presented in Fig. 6-6.

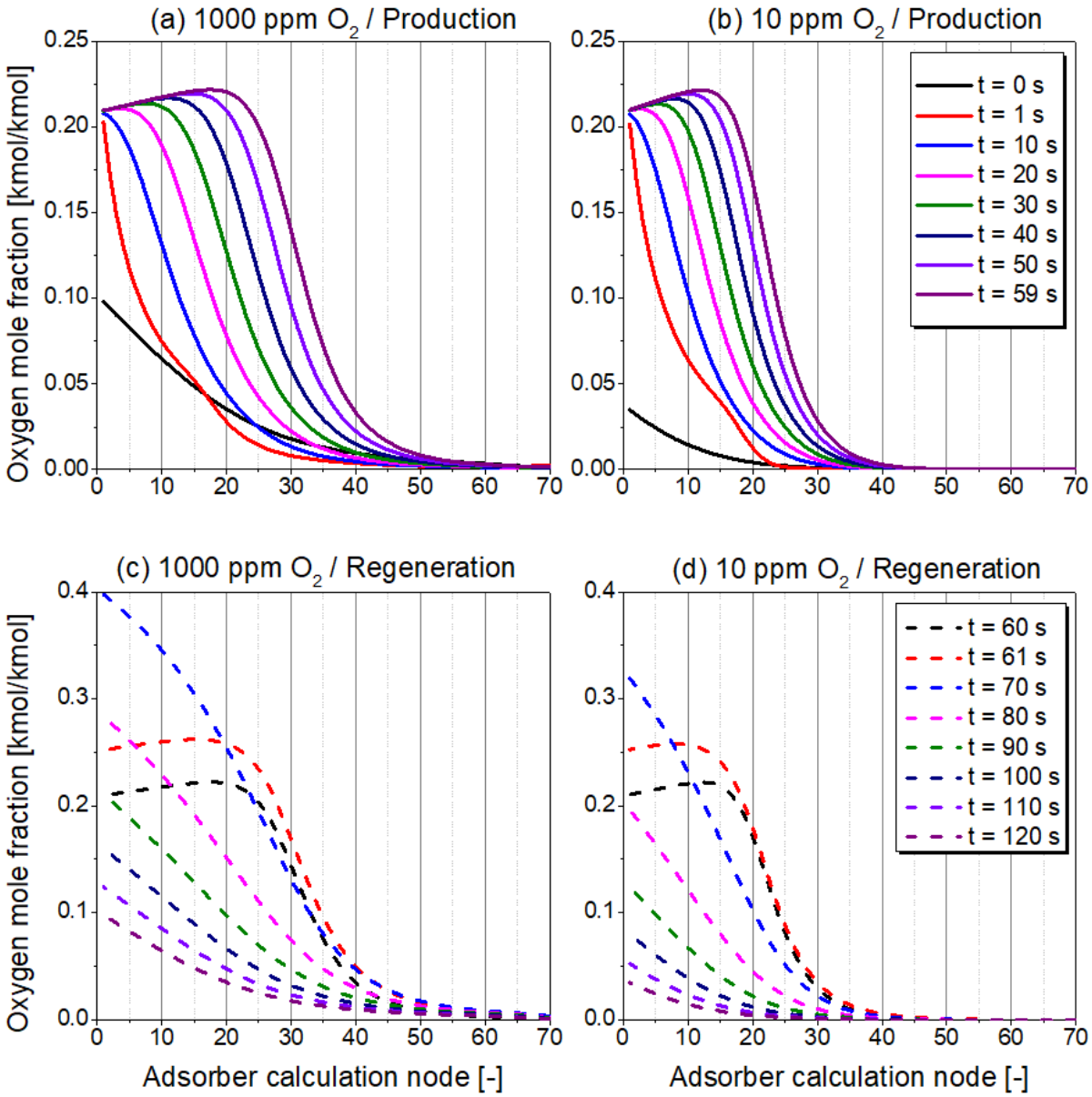

Fig. 6-5 Oxygen MTZ along the adsorber length at different time of the PSA reference cycle: (a, c) at product purity of 1000 ppm O_2; (b, d) at product purity of 10 ppm O_2; (a, b) during the production; (c, d) during the regeneration; here nodes 1 and 70 indicate the bottom and the top of the column, respectively

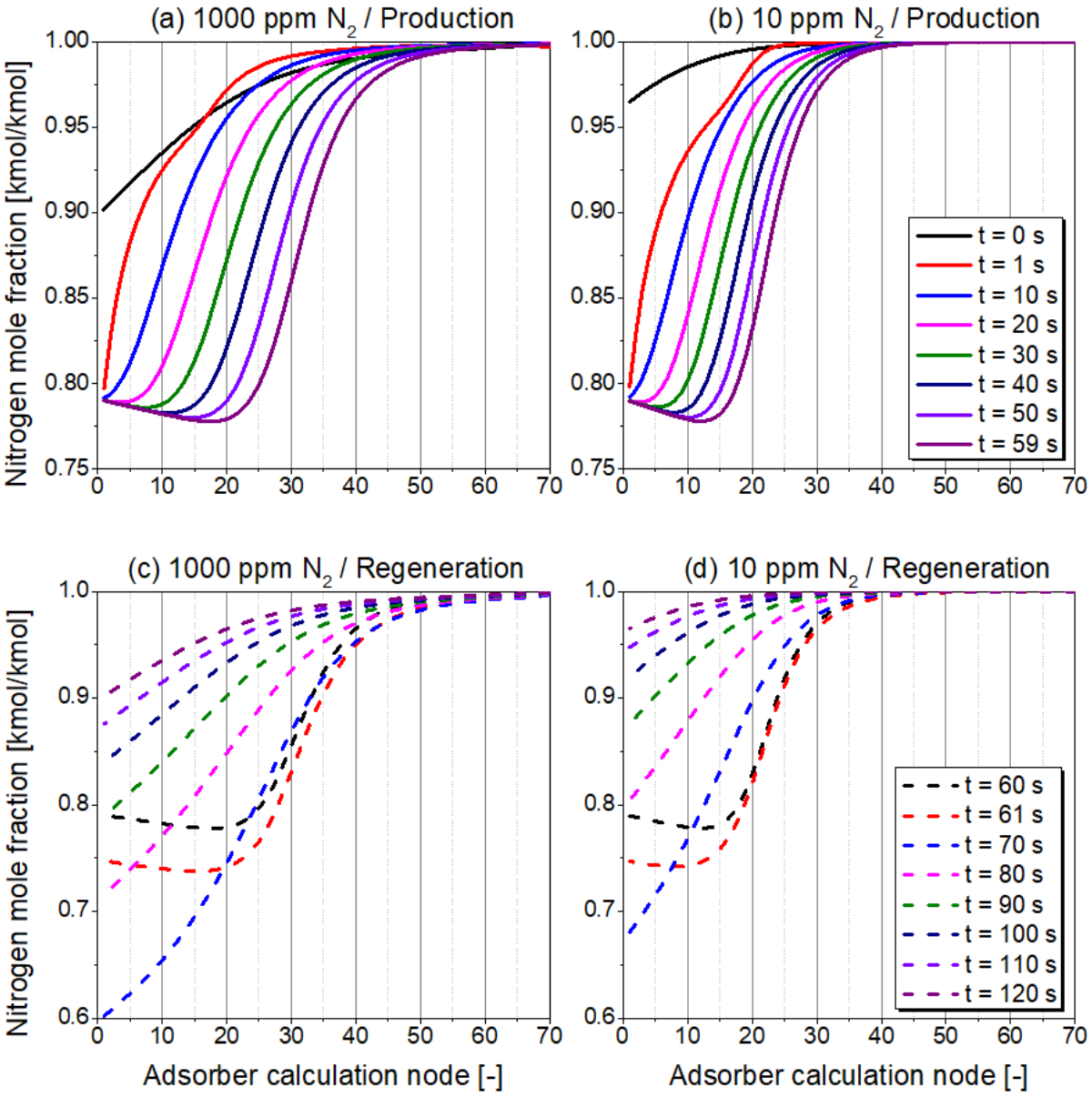

Fig. 6-6 Nitrogen MTZ along the adsorber length at different time of the PSA reference cycle: (a, c) at product purity of 1000 ppm O_2; (b, d) at product purity of 10 ppm O_2; (a, b) during the production; (c, d) during the regeneration; here nodes 1 and 70 indicate the bottom and the top of the column, respectively

7 Performance intensification strategies

In order to distinguish the most significant process conditions and cycle organisation strategies that should be considered towards PSA process intensification, performance indicators at product purity levels of 1000, 100, and 10 ppm O_2 were designated based on the outcome of the dynamic simulation, as presented in Fig. 7-1–5. Subsequently, the highest productivity and lowest air demand values were selected among the results in the studied parameter ranges, which correspond to those presented in Chapters 5.1–2. The findings are presented in Tab. 7-1 and Fig. 7-6–7.

Depending on the required product purity level, particular process conditions or cycle organisation strategies come to the fore while implementing PSA performance intensification strategies.

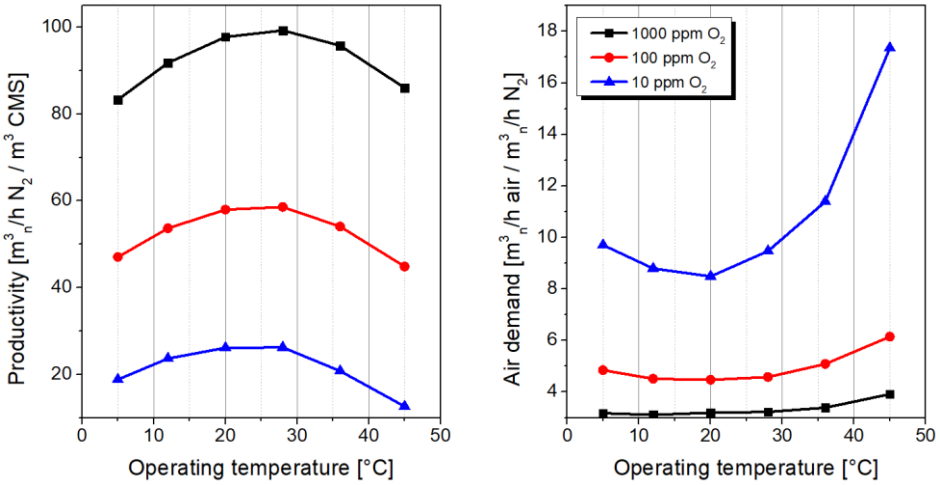

Fig. 7-1 Simulated productivity and air demand as a function of operating temperature

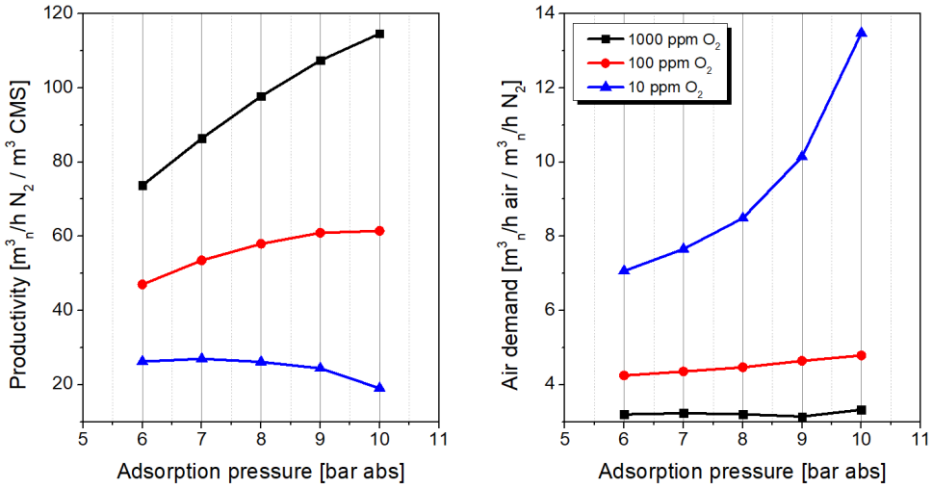

Fig. 7-2 Simulated productivity and air demand as a function of adsorption pressure

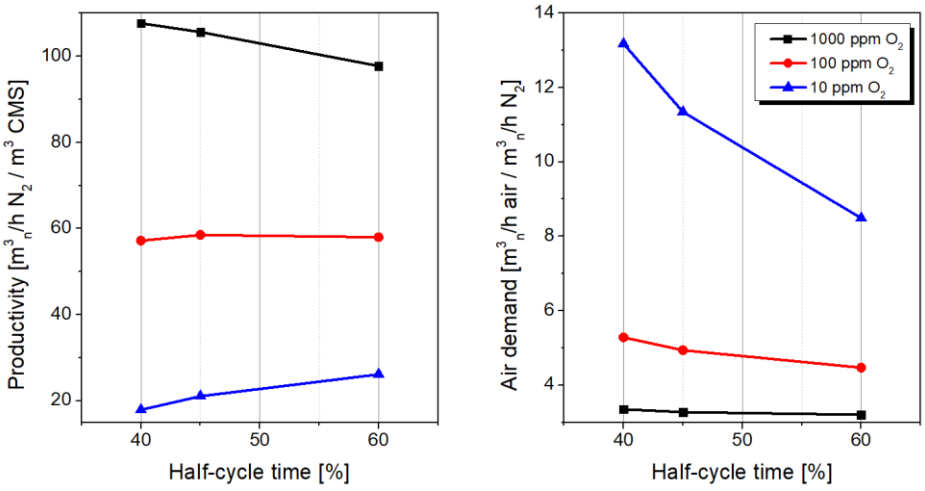

Fig. 7-3 Simulated productivity and air demand as a function of half-cycle time

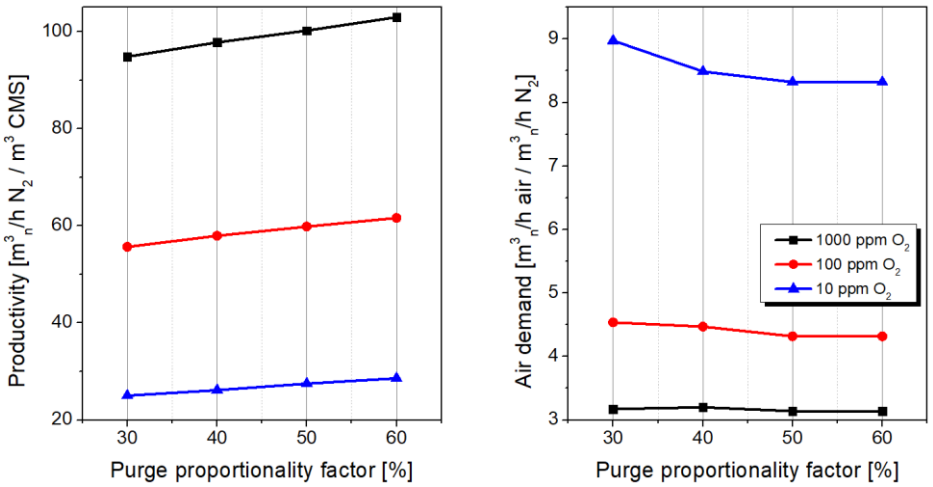

Fig. 7-4 Simulated productivity and air demand as a function of purge proportionality factor

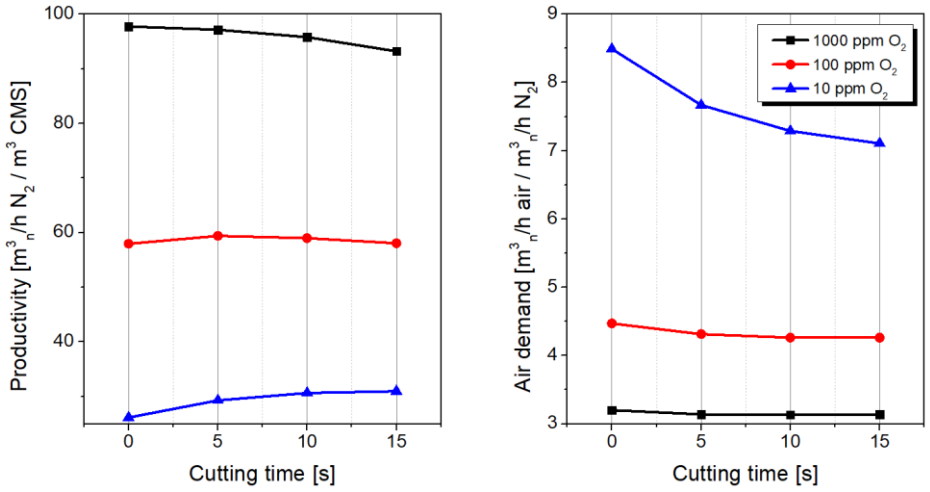

Fig. 7-5 Simulated productivity and air demand as a function of cutting time

According to Tab. 7-1 and Fig. 7-6, when an increased nitrogen productivity is the priority, the most advantage would bring: (1) adjusting the adsorption pressure to 10 bar abs at a product purity of 1000 ppm O_2; (2) adjusting the purge proportionality factor to 60 % at a purity of 100

ppm O_2; or (3) adjusting the cutting time to 15 s at a purity of 10 ppm O_2. However, in accordance with a current global focus on the energy conservation issue, a minimised air demand, rather than maximised productivity designates the preferable process outcome. Therefore, according to Tab. 7-1 and Fig. 7-7, it is of major advantage to (1) operate the PSA plant at moderate temperature of about 20 °C for the nitrogen generation at a purity of 1000 ppm O_2; (2) adjust the adsorption pressure to 6 bara at the product purity of 100 ppm O_2; or, in the same manner, (3) to adjust the adsorption pressure to 6 bara at a product purity of 10 ppm O_2. The detailed operating guidelines of the PSA unit with a focus on the intensification of process performance are presented in Tab. 7-2.

Tab. 7-1 Highest productivity and lowest air demand values at individual process intensification strategies

			Highest productivity [m^3_n/h N_2 / m^3 CMS]			**Lowest air demand [m^3_n/h air / m^3_n/h N_2]**		
	Parameter	Range	1000 ppm O_2	100 ppm O_2	10 ppm O_2	1000 ppm O_2	100 ppm O_2	10 ppm O_2
1	Operating temperature	5 – 45 [°C]	99.27 (at 28 °C)	58.56 (at 28 °C)	26.20 (at 28 °C)	3.11* (at 12 °C)	4.47 (at 20 °C)	8.49 (at 20 °C)
2	Adsorption pressure	6 – 10 [bar abs]	114.65* (at 10 bar)	61.45 (at 10 bar)	26.96 (at 7 bar)	3.14 (at 9 bar)	4.24* (at 6 bar)	7.06* (at 6 bar)
3	Half-cycle time	40 – 60 [s]	107.66 (at 40 s)	58.52 (at 45 s)	26.14 (at 60 s)	3.20 (at 60 s)	4.47 (at 60 s)	8.49 (at 60 s)
4	Purge proportionality factor	30 – 60 [%]	102.95 (at 60 %)	61.62* (at 60 %)	28.58 (at 60 %)	3.14 (at 60 %)	4.32 (at 60 %)	8.32 (at 60 %)
5	Cutting time	0 – 15 [s]	97.75 (at 0 s)	59.39 (at 5 s)	30.95* (at 15 s)	3.13** (at 10 s)	4.26 (at 15 s)	7.11 (at 15 s)

***** The most significant potential for productivity enlargement / air demand reduction
****** The second-most significant potential for productivity enlargement / air demand reduction

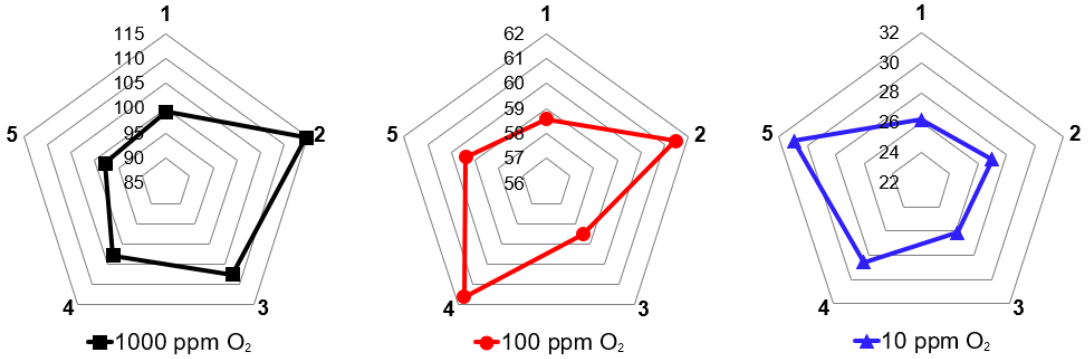

Fig. 7-6 Highest productivity [m^3_n/h N_2 / m^3 CMS] at individual process intensification strategies at different product purity levels: (1) operating temperature; (2) adsorption pressure; (3) half-cycle time; (4) purge flow rate; (5) cutting time

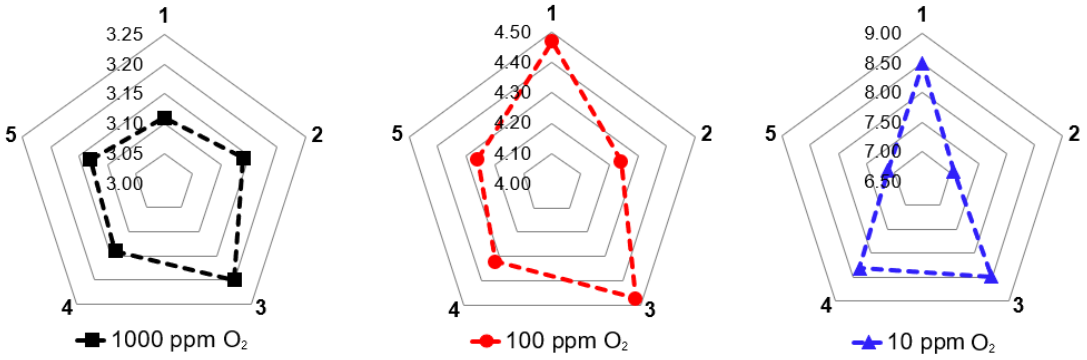

Fig. 7-7 Lowest air demand [m^3_n/h air / m^3_n/h N_2] at individual process intensification strategies at different product purity levels: (1) operating temperature; (2) adsorption pressure; (3) half-cycle time; (4) purge flow rate; (5) cutting time

Moreover, if the parameter which has the most significant potential for productivity enlargement or air demand reduction can not be modified, the parameter of the second-major influence on the process performance should be considered. For instance, the PSA operating temperature can not be adjusted in the standard industrial applications since units are mostly placed outdoors or inside the unheated industrial halls. Hence, according to Tab. 7-1, in order to reduce the air demand figures during the nitrogen generation at purity level of 1000 ppm O_2, the adjustment of the cutting time to 10 s shall be performed.

It is necessary to highlight that all performance intensification measures presented here were studied separately, while all other process conditions were following the reference state. Since the PSA dynamic behaviour is practically responsive to every variation of process conditions and cycle organisation strategy, a multi-parameter optimisation should be executed to demonstrate the overall optimum of PSA performance indicators. Nevertheless, such an approach can be executed with the validated mathematical model of the PSA plant, and therefore depends only on computation time and capacity.

Tab. 7-2 PSA operating guidelines with a focus on the process intensification; here T+B indicates Top/Top + Bottom/Bottom pressure equalisation strategy

Priority	**Increasing the productivity**			**Decreasing the air demand**		
Purity [ppm O_2]	1000	100	10	1000	100	10
Operating temperature [°C]	20	20	20	20	20	20
Adsorption pressure [bar abs]	10*	8	8	8	6*	6*
Half-cycle time [s]	60	60	60	60	60	60
Production time / Blow-down time [s]	59 / 59	59 / 59	59 / 44	59 / 59	59 / 59	59 / 59
Equalisation time [s]	1	1	1	1	1	1
Equalisation strategy	T+B	T+B	T+B	T+B	T+B	T+B
Purge time [s]	59	59	44	59	59	59
Purge proportionality factor [%]	40	60*	40	40	40	40
Purge flowrate [m^3n/h]	0.0485	0.0727	0.0650	0.0485	0.0485	0.0485
Backflow	Yes	Yes	Yes	Yes	Yes	Yes
Cutting time [s]	0	0	15*	0	0	0

***** a factor that was altered in relation to the reference process conditions

8 Summary and final conclusions

This thesis presents an experimentally-verified PSA mathematical model for high-purity applications with the aim to propose appropriate process optimisation schemes.

8.1 Overview of findings

A mathematical model for the dynamic simulation of high-purity twin-bed N_2-PSA was implemented in Aspen Adsorption™ and validated at multiple process conditions, cycle organisation strategies, and plant design parameters. Key-features of the model are a Sips-based IAST-approximation and a quadratic driving force approach. The influence of operating temperature, adsorption pressure, half-cycle time, purge flow rate, cutting time, flow resistances in the piping system, and volume of N_2-receiver tank on productivity and air demand was predicted qualitatively and mostly quantitatively correctly at two different product purity levels. Relative errors of simulated performance indicators were presented and their possible origin was discussed. It was clearly shown that a precise forecast of the PSA operation depends on the accurate representation of many factors, e.g. adsorption isotherms, mass transfer kinetics, pressure and temperature profiles along the adsorber, flow resistances, etc. When fitted to high-purity CMS materials, simulation errors at high-purity levels are expected to decline. A further improvement of the model is possible by introducing an additional gaseous key component combining the effects of moisture and carbon dioxide adsorption for a better simulation of thermal phenomena. The discussion of the adsorber column dynamics was conducted based on the validated mathematical model. The model is particularly capable to propose tailor-made process optimisation strategies. Recommendations for performance improvement, with a particular focus on the reduction of energy consumption, were given based on the simulation outcome at three product purity levels.

8.2 Critical discussion of the work

The mathematical model developed in this work can be applied to evaluate the performance of any twin-bed PSA unit intended for high-purity nitrogen generation; as long as the kinetic parameters, as listed in Tab. 3.5-1, are adjusted according to the utilised CMS material. However, the credibility of model predictions is highly dependent on correct representation of pressure profiles; thus, on proper estimation of flow resistances in the piping system. It should be clearly stated that the assembly of different armature within the PSA piping system, including different types of automatic valves, will certainly result in discrepancies between experimental and numerical data; which constitutes the biggest disadvantage of this type of model.

The crucial aspect regarding modelling of kinetically-controlled air separation is the correct representation of the mass transfer kinetics in highly microporous CMS adsorbent. The classical approach suggests an experimental investigation of breakthrough curves and its detailed analysis followed by the subsequent suggestion of the suitable model. By means of this strategy, an assessment of the origin of mass transfer resistances can be performed. However, in this work, the mass transfer kinetics were found by examination of different available models in order to fit the experimental PSA performance indicators to simulation results. The empirical evaluation of the breakthrough curve was not performed, mostly due to the fact that the

measurement method is inordinately unrepresentable in relation to standard operating conditions of the PSA system. The adsorbent bed would need to be fully regenerated and pressurised with helium; then, the synthetic air stream could be directed into the column. Although, in the PSA applications, the CMS surface is always occupied with oxygen and nitrogen molecules, since their adsorption takes place at atmospheric pressure; whereby the column pressurisation is accomplished with the compressed air stream itself. Apart from that, since the classical approach of breakthrough curve fitting is based on the assumption of the flow pattern corresponding to axially dispersed plug-flow; the occurrence of inevitable effects such as gas channeling within the column, as well as back-mixing in the tube transporting the effluent to the detector, makes this method somewhat unreliable [107]. Notwithstanding the presented explanations, it could still be beneficial to analyse the breakthrough curve in terms of its potential asymmetries, which could ultimately confirm the diffusional resistance occurring mainly in micropores mouths [108]. Without those results, the considerations presented in this work are purely theoretical. Furthermore, detailed experimental data regarding measurements of pure-component adsorption isotherms, exposing the amount adsorbed in the function of time at intermediate pressure steps, were not available. In this work, the only accessible insight into mass transfer kinetics concerns the adsorption of synthetic air mixture, as presented in Fig. 3.5-2. Based on those data, however, the evaluation of a suitable kinetic model was not feasible. Therefore, an enhanced focus should be placed on the experimental study of the mass transfer rate.

Apart from that, the estimation of mass dispersion along the adsorber column could also be improved by performing experimental research. In this work, the axial dispersion coefficient is calculated according to empirical equation presented in Eq. 3.1-4, which does not account for any gas channelling effect, either in the core of the packed bed or alongside the adsorber wall. However, the presence of those effects was concluded based on PSA performance results, as well as experimentally confirmed in the measurement of pressure drop caused by uncontrolled flow resistances in the piping system, as presented in Appendix 10.5. Therefore, the correction of axial dispersion coefficient should be considered, since both effects of mass dispersion and mass transfer kinetics are influencing the progress of mass transfer zone; thus the correct prediction of PSA dynamics.

8.3 Outlook

In this work, the performance of a twin-bed PSA pilot plant for the production of high-purity nitrogen was tested under many different process conditions, cycle organisation strategies, and design parameters; however, the research can be extended to investigate some unusual energy-reduction techniques or some distinct issues occurring during the industrial operation of those systems. Some of the activities considered are described below.

(1) Execution of multi-parameter analysis in order to forecast straightforwardly the PSA performance indicators based on results at miscellaneous operating situations and customer requirements. Therefore, it is advantageous to perform a classical multivariate regression analysis or to implement machine learning techniques to study the PSA system behaviour based on the probability analysis. In particular, artificial neural networks can be used to derive the output of the PSA system [109]. By means of this strategy, the optimum PSA performance could be established.

(2) Studies of PSA dynamic behaviour in transient conditions followed by the evaluation of the rate of accomplishing cyclic-steady state, which could be of particular interest for PSA applications that do not require a continuous flow of nitrogen. An example could be a nitrogen generator providing a modified atmosphere toward fire prevention in warehouses, data centers, or archives. In this case, the operation schedule of the PSA system is related to fluctuations of oxygen level in the controlled volume, e.g. depending on how often the exit door stays open.

(3) Investigation of the influence of moisture presence in feed stream on PSA performance indicators; especially in the long-term operation regime. The findings could be of interest for customers operating PSA nitrogen generators in warm climates, where installation of refrigerator dryers together with compressor becomes unprofitable.

(4) Comparison of PSA performance provided by different CMS materials. Especially the influence of pellet diameter could be of particular interest; however, the raw material, the pore size distribution, or the relative volume (ratio of the adsorbed gas volume to the adsorber volume) figures could influence the process efficiency.

(5) Consideration of the two-PSA-train concept towards the reduction of the N_2-receiver volume; therefore, diminishing the system footprint, as well as the capital costs. The idea is based on a parallel operation of two PSA units, where cycles are slightly shifted in time. As a result, the back-flow and the purge streams can be provided directly from the high-pressure column of one unit to the low-pressure column of the other unit.

(6) Resolution of the system scale-up problem, which concerns the design procedure of industrial-scale systems based on knowledge obtained by the operation of pilot-plants. The engineering challenge corresponds not only to elevated pressure drop along the packed bed, but also to different gas residence times within the column, as well as a significantly increased ratio of adsorber-to-pellet diameters in relation to smaller systems.

(7) Analysis of the chaos theory involved in experiments and simulations of PSA units. Since the nitrogen generation is characterised as a deterministic nonlinear system, a small change in initial conditions, e.g. manually adjusted feed pressure, can result in large differences in the final results of performance indicators. Those errors in measurements, but also due to rounding of numbers while numerical computations, can make a precise prediction of the dynamic behaviour of the PSA system impossible.

9 References

[1] A. Marcinek, J. Guderian, D. Bathen, Performance determination of high-purity N2-PSA-plants, Adsorption 26 (2020) 1215–1226.

[2] A. Marcinek, J. Guderian, D. Bathen, Process intensification of the high-purity nitrogen production in twin-bed Pressure Swing Adsorption plants: DOI: 10.1007/s10450-020-00291-8, Adsorption (2021).

[3] A. Marcinek, A. Möller, J. Guderian, D. Bathen, Dynamic simulation of high-purity twin-bed N2-PSA plants: DOI: 10.1007/s10450-021-00320-0, Adsorption (2021).

[4] S. Chiti, A Pilot Study on Hypoxic Air Performance in Fire Prevention, Fire Technol 51 (2015) 393–407.

[5] M. Dong, Y. Wang, J. Cai, T. Feng, Y. Pu, Effects of nitrogen on wettability and reliability of lead-free solder in reflow soldering, in: 2009 International Conference on Electronic Packaging Technology & High Density Packaging, IEEE, 8/10/2009 - 8/13/2009, pp. 147–151.

[6] C. Pauzon, E. Hryha, P. Forêt, L. Nyborg, Effect of argon and nitrogen atmospheres on the properties of stainless steel 316 L parts produced by laser-powder bed fusion, Materials & Design 179 (2019) 1–10.

[7] H. M. Haynes (Ed.), CRC Handbook of Chemistry and Physics (97th ed.), CRC Press, 2016-2017.

[8] N. N. Greenwood, A. Earnshaw, Chemistry of the Elements (Second Edition): Nitrogen, Elsevier Ltd., 1997.

[9] Grand View Research Inc., Industrial Gases Market Size, Share & Trends Analysis Report By Product (Nitrogen, Oxygen), By Application (Healthcare, Manufacturing), By Distribution (Onsite, Bulk), By Region, And Segment Forecasts, 2020 - 2027, Online access: www.grandviewresearch.com (22/2/2021).

[10] W.F. Castle, Air separation and liquefaction: recent developments and prospects for the beginning of the new millennium, International Journal of Refrigeration 25 (2002) 158–172.

[11] A. S. Emrani, M. Saber, F. Farhadi, A Decision Tree for Technology Selection of Nitrogen Production Plants, Journal of Chemical and Petroleum Engineering, University of Tehran 45 (2011) 1–11.

[12] T. Hu, H.P. H. Zhou, H. Jiang, Nitrogen Production by Efficiently Removing Oxygen From Air Using a Perovskite Hollow-Fiber Membrane With Porous Catalytic Layer, Front. Chem. 6 (2018) 329.

[13] D. D. Nikolić, E. S. Kikkinides, Modelling and optimization of hybrid PSA/membrane separation processes, Adsorption 21 (2015) 283–305.

[14] M. J. Campbell, R. Prasad, J. Smolarek, EP0595181 Membrane/PSA-deoxo process for nitrogen production, 1994.

[15] Eurosider, MICROGEN2 PSA Nitrogen Generators, Online access: www.eurosider.com (10/02/2020).

[16] B. Crittenden, W. J. Thomas, Adsorption Technology and Design, Elsevier Science & Technology Books, 1998.

[17] A.R. Smith, J. Klosek, A review of air separation technologies and their integration with energy conversion processes, Fuel Processing Technology 70 (2001) 115–134.

[18] M. Luberti, D. Friedrich, S. Brandani, A. Hyungwoong, Design of a H2 PSA for cogeneration of ultrapure hydrogen and power at an advanced integrated gasification combined cycle with pre-combustion capture, Adsorption 20 (2014) 511–524.

[19] M. S. Santos, C. A. Grande, A. E. Rodrigues, New cycle configuration to enhance performance of kinetic PSA processes, Chemical Engineering Science 66 (2011) 1590–1599.

[20] T. S. Bhatt, G. Storti, J. F. M. Denayer, R. Rota, Equilibrium Theory-Based Assessment of Dual-Reflux Pressure Swing Adsorption Cycles That Utilize Light Gas for Pressure Swing, Ind. Eng. Chem. Res. 58 (2019) 350–365.

[21] I. A. A. C. Esteves, J. P. B. Mota, Simulation of a new hybrid membrane/pressure swing adsorption process for gas separation, Desalination 148 (2002) 275–280.

[22] R. Rota, P. C. Wankat, Intensification of Pressure Swing Adsorption Processes, AIChE J. 36 (1990) 1299–1312.

[23] China Good Quality PSA Oxygen Generator Supplier ©, High Reliability PSA Nitrogen Generator, Pressure Swing Adsorption Nitrogen Generation, Online access: www.oxygennitrogengenerator.com (24/02/2021).

[24] James A. Ritter & The Team, Bench-Scale Development and Testing of Rapid PSA for CO2 Capture, 2015 NETL CO2 Capture Technology Meeting, Pittsburgh, PA, June 25, 2015.

[25] G. Salazar Duarte, B. Schürer, C. Voss, D. Bathen, Adsorptive Separation of CO 2 from Flue Gas by Temperature Swing Adsorption Processes, CBEN 4 (2017) 277–288.

[26] J. Schell, N. Casas, D. Marx, M. Mazzotti, Precombustion CO 2 Capture by Pressure Swing Adsorption (PSA): Comparison of Laboratory PSA Experiments and Simulations, Ind. Eng. Chem. Res. 52 (2013) 8311–8322.

[27] C. Voss, Applications of Pressure Swing Adsorption Technology, Adsorption 11 (2005) 527–529.

[28] A. Dąbrowski, Adsorption — from theory to practice, Advances in Colloid and Interface Science 93 (2001) 135–224.

[29] H.-J.Schröter, Carbon molecular sieves for gas separation processes, Gas Separation & Purification 7 (1993) 247–251.

[30] C. W. Skarstrom, US2944627A Method and apparatus for fractionating gaseous mixtures by adsorption, 1958.

[31] D. Finlayson, A. J. Sharp, UK 365092 Concentration of "vapours" by a pressure swing adsorption over a charcoal adsorbent, 1930.

[32] D. R. Ruthven, S. Farooq, K. S. Knaebel, Pressure Swing Adsorption, VCH Publishers, Inc., 1994.

[33] D. M. Ruthven, Principles of Adsorption and Adsorption Processes, John Wiley & Sons, Inc., 1984.

[34] D. D. Do, Adsorption Analysis: Equilibria and Kinetics, Imperial College Press, 1998.

[35] R.T. Yang, Gas Seperation by Adsorption Processes, 2013.

[36] J. Kärger, D. M. Ruthven, Diffusion in Zeolites and other Microporous Solids, J. Wiley & Sons INC, 1992.

[37] S. Sircar, J. R. Hufton, Why Does the Linear Driving Force Model for Adsorption Kinetics Work?, Adsorption 6 (2000) 137–147.

[38] Z. A. Abdel-Rahman, A. H. Mhdi, H. S. Auob, Parametric Study for Nitrogen Separation from Air by Pressure Swing Adsorption Using Carbon Molecular Sieve, Tikrit Journal of Engineering Sciences (TJES) 23 (2016) 1–9.

[39] J. S. Ehsan, M. Masoud, Pilot-Scale Experiments for Nitrogen Separation from Air by Pressure Swing Adsorption, South African Journal of Chemical Engineering 19 (2014) 42–56.

[40] J. S. Ahari, S. Pakseresht, Determination effects of process variables on Nitrogen production PSA system by mathematical modeling, Petroleum & Coal 50 (2008) 52–59.

[41] A. H. Mahdi, A. M. R. Ahmed, S. S. Salih, H. S. Ayuob, Simulation study of two units of pressure swing adsorption for producing oxygen and nitrogen simultaneously, in: AIP Conference Proceedings 2213, 020166 (2020), pp. 1–12.

[42] E. J. Shokroo, M. Shahcheraghi, M. Farniaei, Study of feed temperature effects on performance of a domestic industrial PSA plant, Appl Petrochem Res 4 (2014) 317–323.

[43] P. V. Chinh, N. T. Hieu, V. D. Tien, et al., Simulation and Experimental Study of a Single Fixed-Bed Model of Nitrogen Gas Generator Working by Pressure Swing Adsorption, Processes 7(10):654 (2019) 1-21.

[44] A.I. Shirley, N.O. Lemcoff, High-purity Nitrogen by pressure-swing adsorption, AIChE J. 43 (1997) 419–424.

[45] A.I. Shirley, N.O. Lemcoff, Air Separation by Carbon Molecular Sieves, Adsorption 8 (2002) 147–155.

[46] N.O. Lemcoff, Nitrogen separation from air by pressure swing adsorption, in: Adsorption and its Applications in Industry and Environmental Protection - Vol.I: Applications in Industry, Elsevier, 1999, pp. 347–370.

[47] M. B. Rao, R. G. Jenkins, W. A. Steele, Mathematical Modeing of Diffusive Potentials Within Carbon Molecular Sieves, 17th Conference on Carbon, American Carbon Society, Extended Abstracts: 114-115 (1985).

[48] R.R. Vemula, M.V. Kothare, S. Sircar, Anatomy of a rapid pressure swing adsorption process performance, AIChE J. 61 (2015) 2008–2015.

[49] H. M. Kvamsdal, T. Hertzberg, Optimization of pressure swing adsorption systems - The effect of mass transfer during the blowdown step, Chemical Engineering Science 50 (1995) 1203–1212.

[50] Our World in Data, Electricity Mix by Hannah Ritchie, Online access: ourworldindata.org (25/02/2021).

[51] D. Bathen, M. Breitbach, Adsorptionstechnik, 1st ed., Springer-Verlag Berlin Heidelberg, 2001.

[52] International Union of Pure and Applied Chemistry IUPAC, Chemisorption and physisorption, 2002, Online access: www.old.iupac.org (30.04.2021).

[53] C. Borgnakke, R. Sonntag, Fundamentals of Thermodynamics, 8th Edition, Wiley, 2013.

[54] S. Kayal, S. Baichuan, B.B. Sah, Adsorption characteristics of AQSOA zeolites and water for adsorption chillers, International Journal of Heat and Mass Transfer 92 (2016) 1120–1127.

[55] A. A. Sharipova et al., Triclosan adsorption from model system by mineral sorbent diatomite, Colloids and Surfaces A 532 (2017) 97–101.

[56] G.P. Jeppu, T.P. Clement, A modified Langmuir-Freundlich isotherm model for simulating pH-dependent adsorption effects, Journal of Contaminant Hydrology 129-130 (2012) 46–53.

[57] V. Steffen, E. Antonio da Silva, et al., Phenomenological adsorption isotherm for a binary system based on Poisson–Boltzmann equation, Surface and Interface Analysis 10 (2018) 50–57.

[58] N. Tzabar, H. J. M. ter Brake, Adsorption isotherms and Sips models of nitrogen, methane, ethane, and propane on commercial activated carbons and polyvinylidene chloride, Adsorption 22 (2016) 901–914.

[59] A. Nuhnen, C. Janiak, A practical guide to calculate the isosteric heat/enthalpy of adsorption via adsorption isotherms in metal-organic frameworks, MOFs, Dalton Transactions 49 (2020) 10295–10307.

[60] P. L. Llewellyn, G. Maurin, Gas adsorption microcalorimetry and modelling to characterise zeolites and related materials, Comptes Rendus Chimie 8 (2005) 283–302.

[61] K. S. Walton, D. S. Sholl, Predicting Multicomponent Adsorption: 50 Years of the Ideal Adsorbed Solution Theory, AIChE Journal 61 (2015) 2757–2762.

[62] A. A. Shapiro, E. H. Stenby, Potential Theory of Multicomponent Adsorption, Journal of Colloid and Interface Science 201 (1998) 146–157.

[63] O. Talu, I. Zwiebel, Multicomponent Adsorption Equilibria of Nonideal Mixtures, AIChE Journal 32 (1986) 1263–1276.

[64] S. Suwanayuen, R. P. Danner, Vacancy Solution Theory of Adsorption From Gas Mixtures, AIChE Journal 26 (1980) 76–83.

[65] A. L. Myers, J. M. Prausnitz, Thermodynamics of Mixed-Gas Adsorption, AIChE Journal 11 (1965) 121–127.

[66] L. Martínez-Balbuena et al., Applicability of the Gibbs Adsorption Isotherm to the analysis of experimental surface-tension data for ionic and nonionic surfactants, Advances in Colloid and Interface Science 247 (2017) 178–184.

[67] W. Kast, Adsorption aus der gasphase: ingenieurwissenschaftliche Grundlagen und technische verfahren, VCH, 1988.

[68] E. Gluekauf, Theory of chromatography, Part 10, Formula for diffusion into spheres and their application to chromatography, Transactions of the Faraday Society 51 (1955) 1540–1551.

[69] S. Brandani, Exact equivalence at cyclic steady state between isothermal diffusion and linear driving force models for linear adsorption systems, Adsorption 27 (2021) 171–180.

[70] S.-I- Nakao, M. Suzuki, Mass transfer coefficient in cyclic adsorption and desorption, J. Chem. Eng. Japan / JCEJ 16 (1983) 114–119.

[71] J. Villadsen, M. L. Michelsen, Solution of Differential Equation Models by Polynomial Approximation, Prentice-Hall, Inc., 1978.

[72] T. Vermeulen, Theory for Irreversible and Constant-Pattern Solid Diffusion, Industrial & Engineering Chemistry 45 (1953) 1664–1670.

[73] R. Valenciano, E. Aylón, M. T. Izquierdo, A Critical Short Review of Equilibrium and Kinetic Adsorption Models for VOCs Breakthrough Curves Modelling, Adsorption Science and Technology 33 (2015) 851–869.

[74] E. L. Cussler, DIFFUSION: Mass Transfer in Fluid Systems, Third Edition: Ch. 5.1.1, Eq. 5.1-1–5.1-3, Cambridge University Press, 2009.

[75] A. Kayode Coker, Ludwig's Applied Process Design for Chemical and Petrochemical Plants, Fourth Edition: Appendix C: Physical Properties of Liquids and Gases, Tab. C-4, C-6, Elsevier Inc., 2007.

[76] C. Tien, Adsorption calculations and modeling, Butterworth-Heinemann, 1994.

[77] N. Tzabar, H.J.M. ter Brake, Adsorption isotherms and Sips models of nitrogen, methane, ethane, and propane on commercial activated carbons and polyvinylidene chloride, Adsorption 22 (2016) 901–914.

[78] D. C. Koopman, J. V. Cole, H. H. Lee, Assumption of Local Equilibrium in Adsorption Processes, AIChE J. 38 (1992) 623–625.

[79] S. Sircar, R. Mohr, C. Ristic, M. B. Rao, Isosteric Heat of Adsorption: Theory and Experiment, The Journal of Physical Chemistry B 103 (1999) 6539–6546.

[80] S. V. Patel, J. M. Patel, Separation of High Purity Nitrogen from Air by Pressure Swing Adsorption on Carbon Molecular Sieves, International Journal of Engineering Research & Technology (IJERT) 3 (2014).

[81] M. S. A. Baksh, R. T. Yang, Unique adsorption properties and potential energy profiles of microporous pillared clays, AIChE J. 38 (1992) 1357–1368.

[82] Adsorption and its Applications in Industry and Environmental Protection - Vol.I: Applications in Industry, Elsevier, 1999.

[83] D. Shen, M. Bülow, N. O. Lemcoff, Mechanisms of Molecular Mobility of Oxygen and Nitrogen in Carbon Molecular Sieves, Adsorption 9 (2003) 295–302.

[84] H. K. Chagger, F. E. Ndaji, M. L. Sykes, K. M. Thomas, Kinetics of adsorption and diffusional characteristics of carbon molecular sieves, Carbon 33 (1995) 1405–1411.

[85] H. Qinglin, S. Farooq, I. A. Karimi, Prediction of binary gas diffusion in carbon molecular sieves at high pressure, AIChE J. 50 (2004) 351–367.

[86] Y. D. Chen, R. T. Yang, P. Uawithya, Diffusion of oxygen, nitrogen and their mixtures in carbon molecular sieve, AIChE J. 40 (1994) 577–585.

[87] J. Koresh, A. Soffer, Molecular Sieve Carbons: Part 3.-Adsorption Kinetics According to a Surface-barrier Model, J. Cham. Soc., Faraday Trans. 1 77 (1981) 3005–3018.

[88] Y.-S. Bae, C.-H. Lee, Sorption kinetics of eight gases on a carbon molecular sieve at elevated pressure, Carbon 43 (2005) 95–107.

[89] M. C. Campo, F. D. Magalhães, A. Mendes, Comparative study between a CMS membrane and a CMS adsorbent: Part I—Morphology, adsorption equilibrium and kinetics, Journal of Membrane Science 346 (2010) 15–25.

[90] J.-G. Jee, S.-J. Lee, C.-H. Lee, Comparison of the adsorption dynamics of air on zeolite 5A and carbon molecular sieve beds, Korean J. Chem. Eng. 21 (2004) 1183–1192.

[91] Y.-S. Bae, J.-H. Moon, H. Ahn, C.-H. Lee, Effects of adsorbate properties on adsorption mechanism in a carbon molecular sieve, Korean J. Chem. Eng. 21 (2004) 712–720.

[92] C. R. Reid, K. M. Thomas, Adsorption of Gases on a Carbon Molecular Sieve Used for Air Separation: Linear Adsorptives as Probes for Kinetic Selectivity, Langmuir 15 (1999) 3206–3218.

[93] Y.-S- Bae, Y.-K. Ryu, C.-H. Lee, Pressure-dependent models for adsorption kinetics on a CMS, Adsorption Science and Technology (2003) 167–171.

[94] A. L. Cabrera, J. E. Zehner, C. G. Coe, T. R. Gaffney, T. S. Farris, J. N. Armor, Preparation of carbon molecular sieves, I. Two-step hydrocarbon deposition with a single hydrocarbon, Carbon 31 (1993) 969–976.

[95] K. Chihara, M. Suzuki, Control of micropore diffusivities of molecular sieving carbon by deposition of hydrocarbons, Carbon 17 (1979) 339–343.

[96] Y. Kawabuchi, M. Kishino, S. Kawano, D. D. Whitehurst, I. Mochida, Carbon Deposition from Benzene and Cyclohexane onto Active Carbon Fiber To Control Its Pore Size, Langmuir 12 (1996) 4281–4285.

[97] Y. Yamane, H. Tanaka, M. T. Miyahara, In silico synthesis of carbon molecular sieves for high-performance air separation, Carbon 141 (2019) 626–634.

[98] Z. Hu, N. Maes, E. F. Vansant, Molecular probe technique for the assessment of the carbon molecular sieve structure, Journal of Porous Materials 2 (1995) 19–23.

[99] J. S. Adams, A. K.Itta, C. Zhang, G. B.Wenz, O. Sanyal, W. J.Koros, New insights into structural evolution in carbon molecular sieve membranes during pyrolysis, Carbon 141 (2019) 238–246.

[100] M. Rungta, G. B. Wenz, C. Zhang, L. Xu, W. Qiu, J. S. Adams, W. J. Koros, Carbon molecular sieve structure development and membrane performance relationships, Carbon 115 (2017) 237–248.

[101] K. M. Steel, W. J. Koros, Investigation of porosity of carbon materials and related effectson gas separation properties, Carbon 41 (2003) 253–266.

[102] Osaka Gas Chemicals Co., Ltd., Material Safety Data Sheet: SHIRASAGI MSC CT-350.

[103] CarboTech AC GmbH, Technical Information: Carbon Molecular Sieve SHIRASAGI MSC CT-350.

[104] C. A. Grande, Advances in Pressure Swing Adsorption for Gas Separation, ISRN Chemical Engineering 2012 (2012) 1–13.

[105] C. Y. Pan, D. Basmadjian, An analysis of adiabatic sorption of single solutes in fixed beds: pure thermal wave formation and its practical implications, Chemical Engineering Science 25 (1970) 1653–1664.

[106] A. Möller, J. Guderian, J. Möllmer, M. Lange, J. Hofmann, R. Gläser, Kinetische Untersuchungen der adsorptiven Luftzerlegung an Kohlenstoffmolekularsieben, Chemie Ingenieur Technik 85 (2013) 1680–1685.

[107] J. C. Knox, A. D. Ebner, M. D. LeVan, R. F. Coker, J. A. Ritter, Limitations of Breakthrough Curve Analysis in Fixed-Bed Adsorption, Industrial & engineering chemistry research 55 (2016) 4734–4748.

[108] L. H. de Oliveira, J. G. Meneguin, E. A. da Silva, M. A. de Barros, P.A. Arroyo, W. M. Grava, J. F. do Nascimento, Linear Driving Force Model in Carbon Dioxide Capture by Adsorption, AMM 830 (2016) 38–45.

[109] L. Palagi, A. Pesyridis, E. Sciubba, L. Tocci, Machine Learning for the prediction of the dynamic behavior of a small scale ORC system, Energy 166 (2019) 72–82.

10 Appendix

10.1 Interparticle diffusion coefficients

Gaseous interparticle diffusion coefficients of oxygen and nitrogen are calculated according Chapmen-Enskog theory [74] as shown in Eq. A.1-1

$$D_k = \frac{1.86\times10^{-3}T^{3/2}\left(\frac{1}{M_1}+\frac{1}{M_2}\right)^{1/2}}{P\sigma_{12}^2\Omega} \qquad \text{(Eq. A.1-1)}$$

in which D is diffusion coefficient [cm^2/s], T is temperature [K], P is pressure [atm], M_i is molecular weight [kg/kmol], σ_{12} is collision diameter [Å], and Ω is collision integral [-].

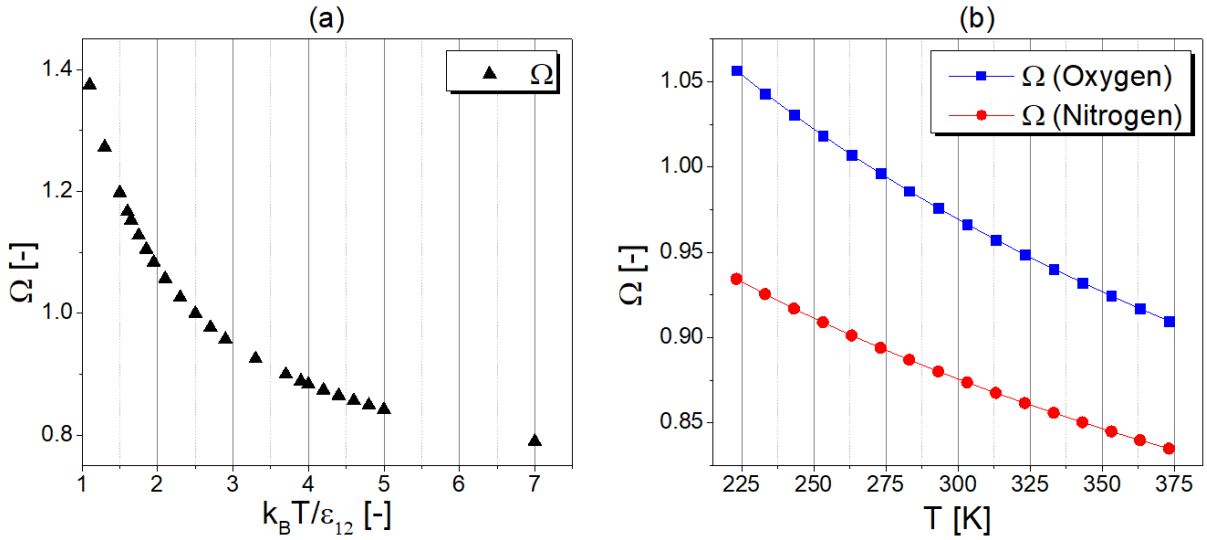

Fig. A.1-1 The collision integral Ω: (a) in the function of parameter k_BT/ε_{12}; (b) in the function of temperature T

The collision diameter σ_{12} is the arithmetic average of the two components. The collision integral Ω is a function of Lennard-Jones potential parameters ε_{12}/k_B [K] and temperature T [K], as presented in Fig. A.1-1a. The parameter k_BT/ε_{12} [-] is determined in the temperature range of -50 °C – 100 °C in order to include a wide range of PSA operating conditions. For that reason, the collision integral Ω is calculated in the specified range of k_BT/ε_{12} parameter from an approximation function as shown in Eq. A.1-2

$$\Omega = A\left(\frac{k_BT}{\varepsilon_{12}}\right)^B \qquad \text{(Eq. A.1-2)}$$

in which A and B are fitting parameters. Subsequently, Ω is determined as a function of temperature T [K], as presented in Fig. A.1-1b and described by an approximation function as shown in Eq. A.1-3

$$\Omega = C\left(T\right)^E \qquad \text{(Eq. A.1-3)}$$

in which C and E are fitting parameters. Therefore, diffusion coefficients of oxygen and nitrogen are implemented in the process simulation straightforward according to equations A.1-4 and A.1-5, respectively, in which D is diffusion coefficient [m^2/s].

$$D_{Oxygen} = \frac{4.81266 \times 10^{-8} T^{1.5}}{66.383537 PT^{-0.291}} \quad \text{(Eq. A.1-4)}$$

$$D_{Nitrogen} = \frac{4.81266 \times 10^{-8} T^{1.5}}{39.77204 PT^{-0.219}} \quad \text{(Eq. A.1-5)}$$

Parameters for the calculation of diffusion coefficients are presented in Tab. A.1-1.

Tab. A.1-1 Parameters for the calculation of diffusion coefficients [74]

	Oxygen	**Nitrogen**
M [kg/kmol]	31.998	28.0134
σ [Å]	3.467	3.798
ε_{12}/k_B [K]	106.7	71.4
T [°C]	-50 – 100	-50 – 100
k_BT/ε_{12} [-]	1.95 – 3.70	2.9 – 7.0
A	1.3097	1.1993
B	-0.291	-0.219
C	5.0976	3.0541
E	-0.291	-0.219

10.2 Gas thermal conductivity

Gas thermal conductivity is calculated according to empirical equation [75] as shown in Eq. A.2-1

$$k_g = \sum k_{gk} y_k \quad \text{(Eq. A.2-1)}$$

in which k_g is thermal conductivity of gaseous mixture [W/m/K], k_{gk} is thermal conductivity of pure component k [W/m/K], and y_k is mole fraction of component k [kmol/kmol].

The thermal conductivity of pure oxygen and nitrogen is calculated according to the empirical equation A.2-2 presented in Tab. A.2-1 along with regression coefficients and temperature range of application.

Tab. A.2-1 Thermal conductivity of pure gases [75]

	$k_{gk} = A + BT + CT^2 \left[\frac{W}{m \cdot K}\right]$ (Eq. A.2-2)			Temperature [K]
	A	B	C	
Oxygen	0.00121	8.6157×10^{-5}	-1.3346×10^{-8}	80 – 1500
Nitrogen	0.00309	7.5930×10^{-5}	-1.1014×10^{-8}	78 – 1500

The parameter k_{gk} is subsequently determined in the temperature range of -50 °C – 100 °C in order to increase the precision of estimation. For that reason, k_{gk} is calculated from an approximation function as shown in Eq. A.2-3

$$k_{gk} = DT + E \quad \text{(Eq. A.2-3)}$$

in which D and E are fitting parameters, and T is temperature [K]. Therefore, gas thermal conductivity is implemented in the process simulation straightforward according to equation A.2-3 in which k_g is thermal conductivity of gaseous mixture [MW/m/K].

$$k_g = \left(7.793\times10^{-11}T + 2.456\times10^{-9}\right)y_{Oxygen} + \left(6.914\times10^{-11}T + 4.118\times10^{-9}\right)y_{Nitrogen} \quad \text{(Eq. A.2-3)}$$

10.3 Gas-solid heat transfer coefficient

The heat transfer coefficient between gas and solid phases h is calculated as a function of Reynolds and Prandtl numbers according to the algorithm presented in Eq. A.3-1–A.3-4 in which h is gas-solid heat transfer coefficient [MW/m^2/K].

$$Re = \frac{2r_p M \rho_g v_g}{\mu}; \quad Pr = \frac{\mu C_{pg}}{k_g M} \quad \text{(Eq. A.3-1; A.3-2)}$$

$$\text{If } Re < 190 \text{ then } j = 1.66Re^{-0.51} \text{ else } j = 0.983Re^{-0.41}; \quad h = jC_{pg}v_g\rho_g Pr^{-2/3} \quad \text{(Eq. A.3-3; A.3-4)}$$

10.4 Adsorbed phase heat capacity

Adsorbed phase heat capacity is calculated according to empirical equation [75] as shown in Eq. A.4-1

$$C_{pak} = f\left(T\right) \quad \text{(Eq. A.4-1)}$$

in which C_{pak} is adsorbed phase heat capacity of component k [J/mol/K], and T is temperature [K]. Because the gas temperature in the studied system is always higher than the critical temperature of oxygen and nitrogen, the adsorbed phase heat capacity is calculated in terms of ideal gases [76].

The adsorbed phase heat capacity of oxygen and nitrogen is calculated according to the empirical equation A.4-2 presented in Tab. A.4-1 along with regression coefficients and temperature range of application.

Tab. A.4-1 Heat capacity of pure gases [75]

	$C_{pa} = A + BT + CT^2 + DT^3 + ET^4 \left[\frac{J}{mol\cdot K}\right]$ (Eq. A.4-2)					Temperature [K]
	A	B×10^3	C×10^5	D×10^9	E×10^{13}	
Oxygen	29.526	-8.8999	3.8083	-32.629	88.607	50 – 1500
Nitrogen	29.342	-3.5395	1.0076	-4.3116	2.5935	50 – 1500

The parameter C_{pak} is determined in the temperature range of -50 °C – 100 °C in order to increase the precision of estimation. For that reason, C_{pak} is calculated from an approximation function as shown in Eq. A.4-3

$$C_{pak} = FT^2 + GT + H \quad \text{(Eq. A.4-3)}$$

in which *F*, *G*, and *H* are fitting parameters, and *T* is temperature [K]. Therefore, adsorbed phase heat capacities of oxygen and nitrogen are implemented in the process simulation straightforwardly according to equations A.4-4 and A.4-5, respectively, in which C_{pa} is adsorbed phase heat capacity [MJ/kmol/K].

$$C_{paOxygen} = 1\times10^{-8}T^2 - 2\times10^{-6}T + 0.0289 \quad \text{(Eq. A.4-4)}$$

$$C_{paNitrogen} = 6\times10^{-9}T^2 - 2\times10^{-6}T + 0.0292 \quad \text{(Eq. A.4-5)}$$

10.5 Pressure drop due to uncontrolled flow resistances in the piping system

The pressure drop caused by uncontrolled flow resistances in the PSA piping system was studied experimentally in the PSA pilot-plant. In order to do so, the outlet of the adsorber column was directed to the atmosphere, the pressure of an inlet gas stream was manipulated with a manual pressure controller (PC), and the gas pressure within the column (PIR 1 – PIR 5) as well as feed stream flow rate (FM) were recorded. The scheme of experimental set-up together with the results are presented in Fig. A.5-1.

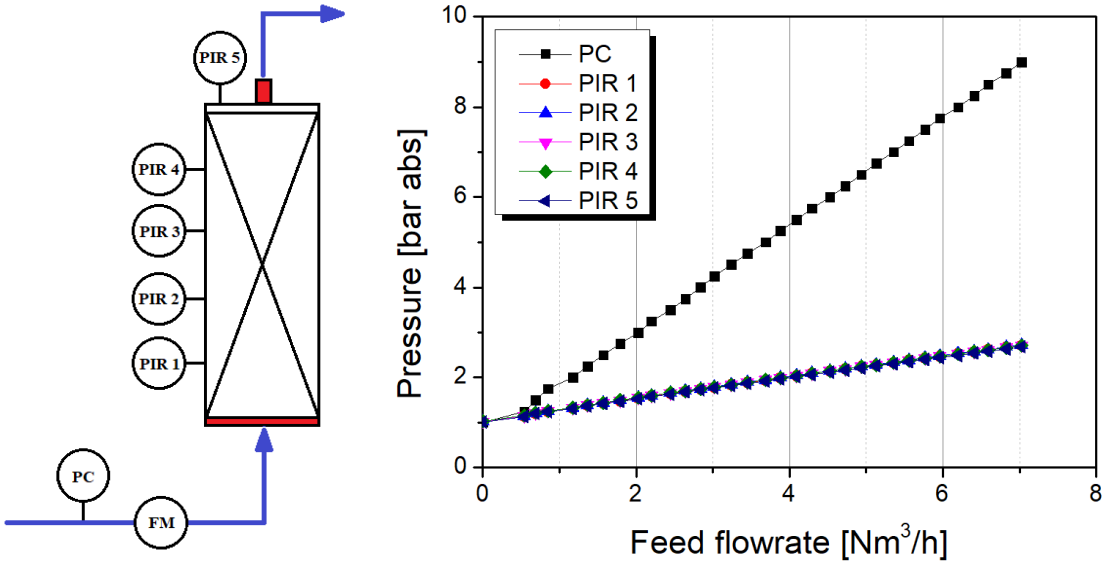

Fig. A.5-1 Experimental set-up for the determination of uncontrolled flow resistances in the PSA piping system (marked with a red colour); and the empirical results

The experiment confirmed the occurrence of the gas channelling effect in the adsorber near-wall volume since pressure values recorded by indicators PIR 1 – PIR 5 showed no significant difference. Therefore, the pressure drop on the packed bed supporting plate placed at the bottom of the column was calculated as the difference between the inlet pressure (PR) and the arithmetic average pressure value of remaining indicators (PIR 1 – PIR 5). Accordingly, the pressure drop on the microfilter placed at the top of the column was calculated as the difference between arithmetic average pressure value of indicators PIR 1 – PIR 5 and atmospheric pressure level (1 bar abs).
The calculated pressure drop resulting from uncontrolled flow resistances in the PSA piping system is presented in Fig. 2.2-2.

10.6 Flow coefficients of controlled flow resistances in the piping system

Flow coefficients *Cv* of particular valve models V representing controlled flow resistances in the PSA piping system were found individually by the fitting of simulated pressure curves to corresponding experimental pressure curves measured at the top of two adsorbers columns. In order to do so, controlled flow resistances in a specific pipeline were investigated one at a time; therefore, control valves in all other pipelines were fully opened and all other valve models V in the process simulator representing controlled flow resistances were adjusted to simulate the action of the ball valve, accordingly. The results of individually adjusted controlled flow resistances in the PSA piping system are presented in Fig. A.6-1.

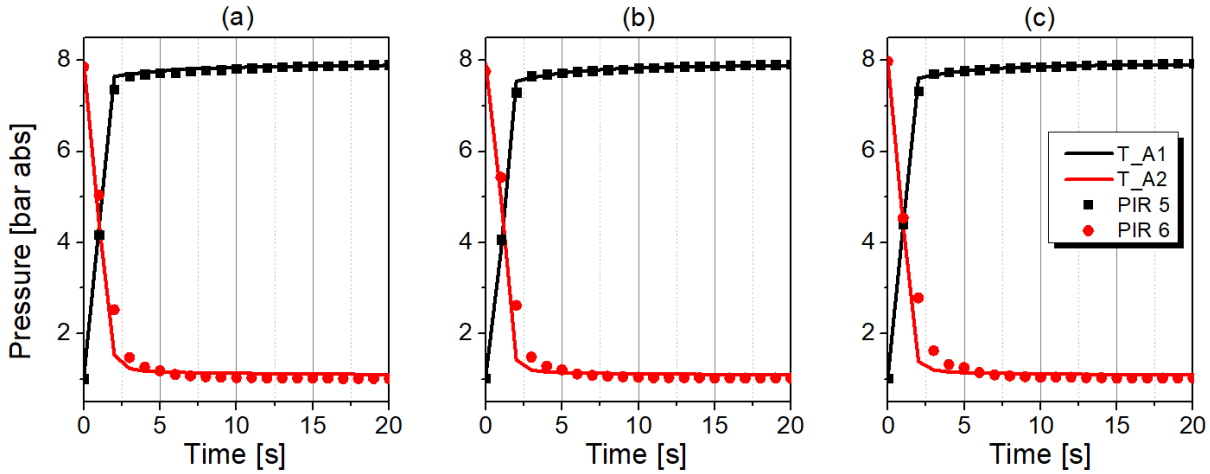

Fig. A.6-1 Experimental and simulated adsorbers pressure profiles at individually adjusted *Cv* values simulating controlled flow resistances in the PSA piping system: (a) feed pipeline *Cv* = 5.0×10^{-1} for V2 and V3; (b) equalisation pipelines *Cv* = 2.5×10^{-5} for V10 and V11; (c) tail gas pipeline – V6 and V7 simulating action of ball valve (minimised flow resistances)

Fig. A.6-1 Flow coefficients *Cv* simulating controlled flow resistances in the PSA piping system

	Stem opening of valve [%]	**Cv [kmol/s/bar]**
Feed pipeline	6	5.0×10^{-4}
	15	1.0×10^{-3}
	25	5.0×10^{-3}
	35	1.5×10^{-2}
	53*	5.0×10^{-1}
Equalisation pipeline	5	1.1×10^{-5}
	25*	2.5×10^{-5}
	50	3.0×10^{-5}
	75	7.4×10^{-5}
Tail gas pipeline	15	1.5×10^{-5}
	25	3.0×10^{-5}
	53	9.0×10^{-5}

* Favourable stem position

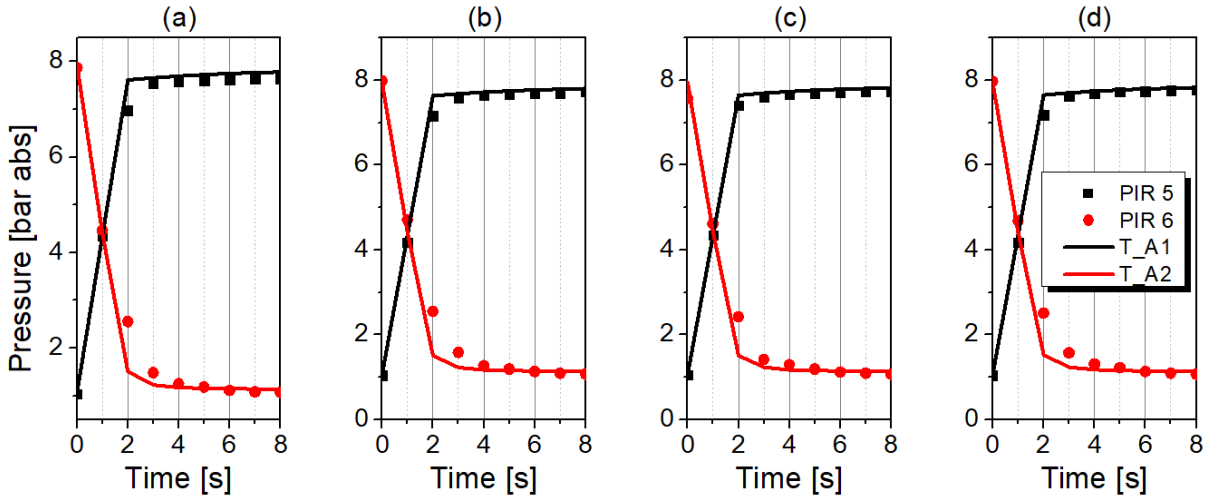

Fig. A.6-2 Experimental and simulated adsorbers pressure profiles at adjusted *Cv* values of V2 and V3 simulating flow resistances in the feed pipeline: (a) $Cv = 5.0 \times 10^{-4}$; (b) $Cv = 1.0 \times 10^{-3}$; (c) $Cv = 5.0 \times 10^{-3}$; (d) $Cv = 1.5 \times 10^{-2}$

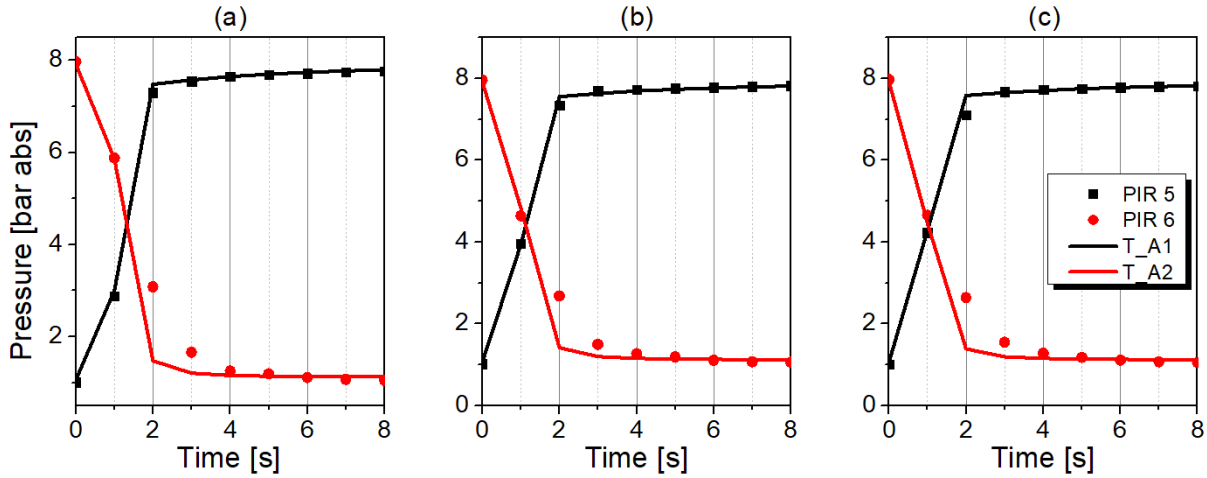

Fig. A.6-3 Experimental and simulated adsorbers pressure profiles at adjusted *Cv* values of V10 and V11 simulating flow resistances in the equalisation pipelines: (a) $Cv = 1.1 \times 10^{-5}$; (b) $Cv = 5.0 \times 10^{-5}$; (c) $Cv = 7.4 \times 10^{-5}$

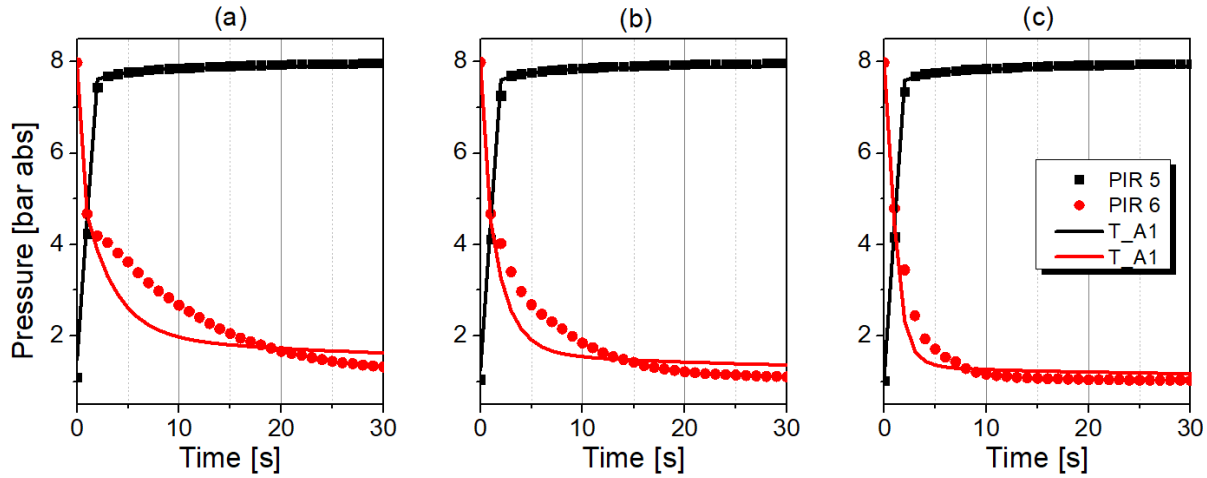

Fig. A.6-4 Experimental and simulated adsorbers pressure profiles at adjusted *Cv* values of V6 and V7 simulating flow resistances in the tail gas pipeline: (a) $Cv = 1.5 \times 10^{-5}$; (b) $Cv = 3.0 \times 10^{-5}$; (c) $Cv = 9.0 \times 10^{-5}$

By means of the same strategy, the quantification of individual flow coefficients *Cv* at different stem positions of particular control valves assembled in the PSA pilot-plant was performed. The results are presented in Fig. A.6-2–A.6-4 and Tab. A.6-1. Since the correct representation of pressure curves during the PSA cycle is crucial for the proper estimation of adsorption isotherms, as well as mass transfer kinetics, more complex investigation of *Cv* data should be considered, especially regarding the tail-gas pipeline.

10.7 Pressure drop along the packed-bed

Pressure drop along the packed bed was studied empirically in the external experimental set-up, the scheme of which is presented in Fig. A.6-1. The column's geometry and operating conditions are given in Tab. A.6-1. The column was packed with adsorbent pellets with the snow-storm filling procedure, corresponding to the method of adsorbers packing in the PSA pilot-plant. The height of the packed bed was adjusted to represent the adsorbent volume in the PSA pilot-plant.

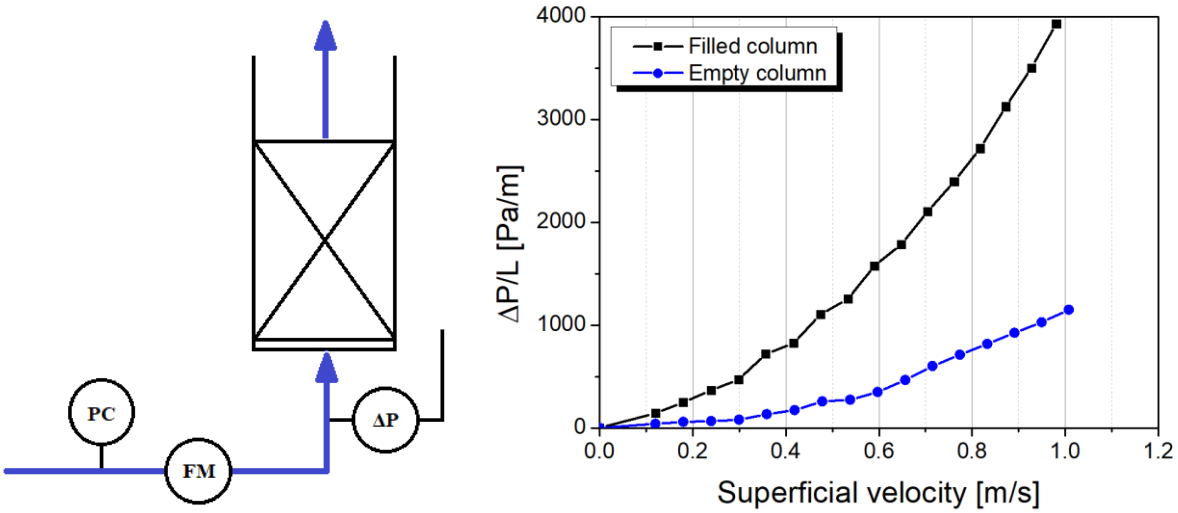

Fig. A.7-1 External experimental set-up for determination of pressure drop along the packed bed; and the empirical results

The pressure of the inlet gas stream was manipulated with a manual pressure controller (PC), and the pressure difference between column inlet and ambient (ΔP) as well as feed stream flow rate (FM) were recorded. Two series of measurements were made: (1) with an empty column to determine the pressure drop on the packed bed supporting plate, and (2) with a filled column. The results are presented in Fig. A.7-1. Therefore, the pressure drop on the packed bed, as presented in Fig 2.2-4, was calculated as the difference of pressure drops determined during measurements with a filled and an empty column.

Tab. A.7-1 Column geometry and experimental conditions

Medium	Dry air
Temperature [°C]	23
Bed length [m]	0.4
Bed diameter [m]	0.08
Bed volume [m^3]	0.00201
Cross-section area [m^2]	0.005024
Packing density [g/L]	667.88

10.8 Statistical analysis of adsorbent pellets geometry

The sample of 100 adsorbent particles was statistically analysed in order to determine the average diameter of the pellet as well as the interparticle porosity of the packed bed according to Eq. A.8-1. Explicit data are presented in Tab. A.8-1. The results are shown in Tab. A.8-2. Mass of the dry sample was determined by subtracting the water content which was determined experimentally by drying the sample at 120 °C until constant weight.

$$\varepsilon_i = 1 - \frac{\rho_s}{\rho_{average}} \qquad \text{(Eq. A.8-1)}$$

Tab. A.8-1 Geometry analysis of the CMS pellets

No.	h [mm]	d [mm]	V [mm³]	No.	h [mm]	d [mm]	V [mm³]	No.	h [mm]	d [mm]	V [mm³]
1	2.85	1.65	6.091	**35**	1.95	1.65	4.168	**68**	3.30	1.65	7.053
2	4.35	1.70	9.869	**36**	2.00	1.70	4.537	**69**	2.25	1.65	4.809
3	2.75	1.65	5.877	**37**	2.50	1.65	5.343	**70**	2.20	1.65	4.702
4	4.15	1.65	8.869	**38**	3.45	1.65	7.373	**71**	2.70	1.65	5.770
5	2.70	1.65	5.770	**39**	4.20	1.65	8.976	**72**	3.00	1.70	6.806
6	3.75	1.60	7.536	**40**	2.75	1.65	5.877	**73**	3.00	1.75	7.212
7	3.25	1.70	7.373	**41**	1.80	1.65	3.847	**74**	3.10	1.65	6.625
8	4.30	1.65	9.190	**42**	3.90	1.60	7.837	**75**	1.75	1.70	3.970
9	3.00	1.65	6.412	**43**	2.90	1.65	6.198	**76**	2.50	1.65	5.343
10	3.05	1.65	6.518	**44**	1.95	1.65	4.168	**77**	1.80	1.65	3.847
11	1.90	1.65	4.061	**45**	4.30	1.65	9.190	**78**	2.10	1.65	4.488
12	2.75	1.65	5.877	**46**	3.10	1.65	6.625	**79**	2.35	1.70	5.331
13	3.30	1.65	7.053	**47**	3.25	1.65	6.946	**80**	2.15	1.65	4.595
14	2.90	1.65	6.198	**48**	2.75	1.65	5.877	**81**	2.50	1.65	5.343
15	2.00	1.65	4.274	**49**	3.80	1.65	8.121	**82**	3.80	1.65	8.121
16	3.50	1.65	7.480	**50**	2.90	1.65	6.198	**83**	1.50	1.70	3.403
17	3.20	1.65	6.839	**51**	3.15	1.70	7.146	**84**	3.60	1.65	7.694
18	4.35	1.65	9.297	**52**	2.70	1.65	5.770	**85**	1.60	1.60	3.215
19	2.55	1.65	5.450	**53**	4.10	1.65	8.762	**86**	1.70	1.70	3.857
20	2.75	1.75	6.611	**54**	3.00	1.65	6.412	**87**	2.20	1.65	4.702
21	1.65	1.65	3.526	**55**	3.45	1.70	7.827	**88**	2.90	1.65	6.198
22	1.85	1.65	3.954	**56**	2.20	1.65	4.702	**89**	2.50	1.70	5.672
23	1.80	1.65	3.847	**57**	2.70	1.65	5.770	**90**	2.00	1.65	4.274
24	4.65	1.70	10.549	**58**	2.10	1.65	4.488	**91**	1.55	1.65	3.313
25	4.45	1.65	9.510	**59**	2.45	1.65	5.236	**92**	2.40	1.70	5.445
26	2.95	1.65	6.305	**60**	1.90	1.65	4.061	**93**	2.10	1.65	4.488
27	2.60	1.70	5.899	**61**	1.90	1.65	4.061	**94**	2.05	1.65	4.381
28	4.15	1.70	9.415	**62**	2.60	1.65	5.557	**95**	2.10	1.70	4.764
29	4.60	1.70	10.436	**63**	3.00	1.65	6.412	**96**	1.05	1.65	2.244
30	1.80	1.75	4.327	**64**	2.45	1.65	5.236	**97**	2.10	1.65	4.488
31	3.15	1.65	6.732	**65**	3.20	1.70	7.260	**98**	1.70	1.65	3.633
32	1.90	1.65	4.061	**66**	2.90	1.60	5.828	**99**	1.25	1.65	2.672
33	2.10	1.60	4.220	**67**	4.10	1.65	8.762	**100**	1.40	1.65	2.992
34	3.25	1.65	6.946								

Tab. A.8-2 Results of geometry analysis of the CMS pellets

Average height of single pellet $h_{average}$ [mm]	2.7385
Average diameter of single pellet $d_{average}$ [mm]	1.6595
Average radius of single pellet $r_{average}$ [mm]	0.8298
Average volume of single pellet $V_{average}$ [mm^3]	5.9202
Water content [wt.-%]	1.91
Average mass of single pellet $m_{average}$ [g]	0.0070635
Average density of single pellet $\rho_{average}$ [kg/m^3]	1193.12
Average packing density ρ_s [kg/m^3]	711
Packed bed interparticle porosity ε_i [m^3 void/m^3 bed]	0.404

10.9 Implementation of the kinetic model into the process simulator

The prediction of pure component adsorption isotherms is described by temperature-dependent Sips model as presented in Eq. 2.3-1–2.3-4. However, in the process simulator the temperature-dependent Sips model is implemented by default according to the function presented in Eq. A.9-1.

$$w_k^* = \frac{IP_1 IP_2 p_k^{IP_3} exp\left(IP_4 / T_s\right)}{1 + IP_5 p_k^{IP_3} exp\left(IP_6 / T_s\right)} \qquad \text{(Eq. A.9-1)}$$

in which IP_x is the isotherm parameter of an unknown unit. Therefore, isotherm parameters IP_x in the process simulator were adjusted to be in accordance with the Sips fitting parameters, as presented in Tab. A.9-1. Moreover, IP_1 was modified to correspond to saturation loading w_{s0}^* as determined by the Sips isotherm model. By means of this strategy, the description of adsorption isotherm is the process simulator is identical to the temperature-dependent Sips model.

Tab. A.9-1 Isotherm parameters of oxygen and nitrogen implemented in the process simulator

	IP_1	IP_2	IP_3	IP_4	IP_5	IP_6
O_2	3.384×10^{-3}	2.163×10^{-4}	9.154×10^{-1}	1.850×10^{3}	5.214×10^{-4}	1.600×10^{3}
N_2	2.707×10^{-3}	3.528×10^{-4}	8.606×10^{-1}	1.811×10^{3}	7.886×10^{-4}	1.584×10^{3}

As presented in Eq. A.9-2, the calculation of mass transfer coefficients requires the inverted isotherm slope dp_k/dw_k. For that reason, the derivative of the adsorption isotherm equation was found as shown in Eq. A.9-3. By means of this strategy, equations for the calculation of mass transfer coefficients are implemented straightforwardly in the process simulator.

$$MTC_k = \frac{1}{r_p^2} A_k \exp\left(\frac{-E_{ak}}{RT_s}\right) \frac{w_k}{p_k} \frac{dp_k}{dw_k} \qquad \text{(Eq. A.9-2)}$$

$$\frac{dp_k}{dw_k} = \frac{\left(1 + IP_5 p_k^{IP_3} exp\left(IP_6 / T_s\right)\right)^2}{IP_1 IP_2 IP_3 p_k^{IP_3 - 1} exp\left(IP_4 / T_s\right)} \qquad \text{(Eq. A.9-3)}$$